# WOJSKOWA AKADEMIA TECHNICZNA
# im. Jarosława Dąbrowskiego

# DOCTORAL DISERTATION

## Ultraviolet radiation in the atmosphere and its applications for military purposes

**mgr inż. Ngoc Hiep Doan**

Promotor:**dr hab. inż. Krzysztof KOPCZYŃSKI, prof. WAT**

Promotor **pomocniczy**: **dr. inż. Marek ZYGMUNT**

**Warszawa, 2026**

**Abstract**

This doctoral thesis focuses on the investigation of ultraviolet (UV) radiation propagation in the atmosphere and its potential applications in missile warning and target detection systems. In recent years, UV radiation has gained increasing interest due to its unique advantages in both civilian and military domains. Civilian applications include flame detection, fire warning, monitoring of partial discharges in high-voltage power systems, and UV index measurements for human health protection [1-4]. In military domain, UV radiation is employed in missile launch warning systems and as a protective channel in multispectral infrared (IR) seekers [5-7].

The most promising feature of UV detection is the so-called solar-blind UV band, where solar radiation is strongly absorbed by atmospheric ozone ($O_3$) and oxygen ($O_2$) [8]. This spectral region allows artificial UV sources, such as missile plumes, to be detected with high signal-to-noise ratios and low false-alarm rates [9]. However, UV detection faces limitations, including restricted detection ranges caused by strong atmospheric absorption and scattering, as well as the presence of solar background radiation at higher altitudes.

To address these challenges, the research presented in this thesis is based on three main directions. First, the attenuation of UV radiation in the atmosphere is studied through theoretical analysis and modelling. Second, photon-counting detectors are employed to measure natural UV background levels. Third, based on UV background measurements and calculations of signal levels the feasibility of UV-based detection was evaluated in two practical scenarios. The expected ranges of detection of missile plume emissions in the solar-blind UV band, and airborne target detection using negative-contrast imaging in the near-UV were calculated for various atmospheric visibilities.

The main achievement of this thesis is the demonstration of the feasibility and limitations of UV-based detection for defense applications. The results confirm that, despite short propagation ranges, UV detection provides a favorable signal-to-background ratio in the solar-blind band, enabling robust missile warning with reduced false-alarm probability. Additionally, the study shows that near-UV imaging can enhance negative-contrast detection of airborne targets. Therefore, it can be concluded that the proposed research directions contribute to a better understanding of UV radiation propagation and provide a scientific foundation for the development of advanced UV sensing systems in defense applications.

**Streszczenie**

Niniejsza rozprawa doktorska koncentruje się na badaniu propagacji promieniowania ultrafioletowego (UV) w atmosferze oraz potencjalnych zastosowaniach tego promieniowania w systemach detekcji startów rakiet i pocisków oraz detekcji celów powietrznych. W ostatnich latach promieniowanie UV wzbudza rosnące zainteresowanie ze względu na swoje unikalne zalety zarówno w zastosowaniach cywilnych, jak i wojskowych. Zastosowania cywilne obejmują detekcję płomienia, systemy wczesnego ostrzegania pożarowego, monitorowanie wyładowań niezupełnych w systemach elektroenergetycznych wysokiego napięcia oraz pomiary poziomu natężenia UV w celu ochrony zdrowia ludzi [1 - 4]. W obszarze wojskowym promieniowanie UV wykorzystywane jest w systemach ostrzegania o starcie pocisków oraz jako dodatkowy kanał w wielospektralnych głowicach naprowadzających w podczerwieni (IR) [5 - 7].

Najbardziej obiecującą cechą detekcji UV jest tzw. pasmo solar-blind UV, w którym promieniowanie słoneczne jest silnie pochłaniane przez ozon atmosferyczny ($O_3$) oraz tlen ($O_2$) [8]. Ten zakres widmowy umożliwia wykrywanie sztucznych źródeł promieniowania UV, takich jak smugi gazów wylotowych pocisków, przy wysokim stosunku sygnału do szumu oraz niskim prawdopodobieństwie fałszywych alarmów [9]. Jednocześnie detekcja UV napotyka na istotne ograniczenia, w tym ograniczony zasięg detekcji spowodowany silnym pochłanianiem i rozpraszaniem w atmosferze, a także obecnością tła słonecznego na większych wysokościach.

W celu przezwyciężenia tych wyzwań wyniki badań przedstawione w niniejszej rozprawie dotyczą trzech głównych obszarów. Po pierwsze, analizowane jest tłumienie promieniowania UV w atmosferze na drodze analizy teoretycznej i modelowania. Po drugie, naturalne tło UV jest mierzone przy pomocy czułych detektorów zliczających fotony. Po trzecie, na podstawie pomiarów promieniowania tła ultrafioletowego i oczekiwanej wielkości sygnałów oceniono możliwość wykrywania zagrożeń. Obliczono zasięgi wykrycia emisji gazów wylotowych pocisków w pasmie solar-blind UV oraz zasięgi wykrycia celów powietrznych z wykorzystaniem obrazowania o kontraście negatywnym w bliskim nadfiolecie.

Głównym osiągnięciem niniejszej rozprawy jest wykazanie możliwości oraz ograniczeń detekcji opartej na promieniowaniu UV w zastosowaniach obronnych. Uzyskane wyniki potwierdzają, że pomimo krótkich zasięgów propagacji, detekcja UV zapewnia korzystny stosunek sygnału do tła w paśmie solar-blind, umożliwiając

wiarygodne ostrzeganie o starcie pocisków przy zmniejszonym prawdopodobieństwie fałszywych alarmów. Ponadto wykazano, że obrazowanie w bliskim nadfiolecie może zwiększyć skuteczność detekcji celów powietrznych przy wykorzystaniu negatywnego kontrastu. Można zatem stwierdzić, że zaproponowane kierunki badań przyczyniają się do lepszego zrozumienia propagacji promieniowania UV oraz stanowią podstawę do rozwoju zaawansowanych systemów detekcji UV w zastosowaniach obronnych.

**Acknowledgments**

I would like to express my sincere gratitude to Professor Krzysztof Kopczyński for his guidance and for providing excellent conditions for me to conduct my research and carry out experiments at the Institute of Optoelectronics. I have also gained valuable knowledge and received many helpful comments from him during discussions of my research.

I would like to sincerely thank Dr. Marek Zygmunt for his scientific guidance, helpful feedback, and for providing access to experimental equipment for my research. I am also grateful to Dr. Zbigniew Zawadzki for his dedicated support and valuable contributions to this research. My sincere thanks also go to my colleagues from the Zespół Laserowej Teledetekcji for their strong support in the design, assembly and installation of the UV radiation measurement system.

Finally, I am very grateful to my family, my wife, and my children for their constant encouragement and support throughout my PhD studies in Poland.

**Table of contents**

**List of Abbreviations:**

| | |
|---|---|
| AFRL | Air Force Research Laboratory |
| AOD | Aerosol Optical Depth |
| ASTM | American Society for Testing and Materials |
| c | Velocity of light |
| CFD | Computational Fluid Dynamics |
| CMOS | Complementary Metal-Oxide-Semiconductor |
| CMWS | Common Missile Warning System |
| DIRCM | Directional Infrared Countermeasures |
| DU | Dobson Unit |
| EUV | Extreme Ultraviolet |
| FOV | Field Of View |
| FPA | Focal Plane Array |
| FUV | Far Ultraviolet |
| FWHM | Full Width at Half Maximum |
| GAW | Global Atmosphere Watch |
| h | Planck's constant |
| HITRAN | HIgh-resolution TRANsmission molecular absorption database |
| HTPB | Hydroxyl-Terminated PolyButadiene |
| IFOV | Instantaneous Field Of view |
| IR | Infrared |
| K | Kenvil |
| LWIR | Long-Wave Infrared |
| MANPADS | Man-Portable Air Defense Systems |
| MLS | Mid-Latitude Summer |
| MLW | Mid-Latitude Winter |
| MODTRAN | MODerate resolution TRANsmittance |
| MT | Magnesium-Teflon |
| MTV | Magnesium-Teflon-Viton |
| MUV | Middle Ultraviolet |
| MWIR | Mid-Wave Infrared |
| MWS | Missile Warning System |

| | |
|---|---|
| NA | Numerical Aperture |
| NEP | Noise Equivalent Power |
| NUV | Near Ultraviolet |
| NWIR | Near-Wave Infrared |
| PMT | PhotoMultiplier Tube |
| ppmv | parts per million by volume |
| $P_d$ | Probability of detection |
| $P_{fa}$ | Probability of False Alarm |
| QE | Quantum Efficiency |
| RT | Radiative Transfer |
| RTE | Radiative Transfer Equation |
| ROIC | ReadOut Integrated Circuit |
| SNR | Signal-to-Noise Ratio |
| SWIR | Short-Wave Infrared |
| SZA | Solar Zenith Angle |
| UAV | Unmanned Aerial Vehicle |
| UV | Ultraviolet |
| UV-A | Ultraviolet-A |
| UV-B | Ultraviolet-B |
| UV-C | Ultraviolet-C |
| VIS | Visible |
| VUV | Vacuum Ultraviolet |
| WMO | World Meteorological Organization |
| WOUDC | World Ozone and Ultraviolet Radiation Data Centre |
| λ | Wavelength |

## 1. Introduction

In recent years, electro-optical applications have witnessed significant development not only in the visible, infrared, and terahertz spectral regions, but also in the ultraviolet (UV) spectrum. UV radiation has found wide-range applications across multiple domains. Notable examples include:

- Civilian applications, such as flame detection and fire warning systems, UV cameras for monitoring and detecting partial discharges on high-voltage power lines and substations helping to prevent failures and support maintenance. Monitoring systems for UV index and erythemal dose are also crucial for evaluating the effects of UV radiation on human health, including the risk of sunburn, skin aging, cataracts, and skin cancer.
- Military applications, including missile launch warning systems and UV protection channels integrated into infrared seekers to improve target discrimination from countermeasures.

Electro-optical systems operating in the UV band benefit from high sensitivity due to low background noise levels. The primary natural UV radiation source is the Sun; however, atmospheric constituents - especially ozone ($O_3$) and oxygen ($O_2$) - strongly absorb UV radiation. As a result, a spectral region known as the solar-blind UV band is formed, in which solar UV radiation cannot reach lower layers of the atmosphere. This creates ideal conditions for detecting artificial UV sources with high signal-to-noise ratios.

A typical example is missile warning systems operating in the solar-blind UV region. A missile plume emits radiation across the spectrum from UV to MWIR; however, the small fraction of emission within the solar-blind UV band is highly useful, as there is virtually no solar background at low altitudes. Most sources within this band are artificial, there is no natural background, and although the signal may be weak, the absence of background noise provides strong scene contrast and a high signal-to-clutter ratio, significantly reducing false alarms.

Despite this advantage, UV-based missile launch detection systems also have limitations:

- Detection range is relatively short due to atmospheric absorption and scattering of UV radiation.

- At high altitudes, the ozone layer no longer fully blocks solar UV, leading to increased solar background even in the UV-blind region.

Notable operational UV-based missile warning systems include the AN/AAR-54(V) and AN/AAR-57 (CMWS). The AAR-54 is a passive UV sensor capable of tracking multiple sources simultaneously, rapidly classifying threats, and interfacing with countermeasure systems. It can be integrated across various airborne platforms. The AAR-57, developed by BAE Systems in 2005, expands upon AAR-54's capabilities by incorporating Hostile Fire Indication, missile warning, and data logging functions, enabling detection of small arms and Rocket-Propelled Grenades (RPGs), and supporting post-mission analysis [10-11].

Some third-generation infrared-guided MANPADS (Man-Portable Air Defense Systems) utilize multi-spectral seekers to identify targets under conditions where single-band detection is insufficient. These seekers may combine UV/IR or SWIR/MWIR channels, allowing improved discrimination between real targets and countermeasures. Multispectral homing systems incorporating UV channels typically feature cooled InSb detectors (with peak sensitivity around 4 μm) and UV-sensitive detectors based on Si, CdS, or GaAs. Airborne targets tend to exhibit weak signals in the UV band and strong emissions in the MWIR band - making it easier to differentiate them from modern flares [12].

Several modern missile seekers have integrated UV detection channels to enhance tracking and resistance to countermeasures:

- The Stinger POST missile uses a two-color (IR/UV) seeker, with an InSb detector for hot gas plumes and a CdS detector to track UV radiation emitted from the aircraft surface, allowing engagement from multiple angles [13].
- The Piorun+ features a tri-band seeker (2IR + 1UV) using argon-cooled detectors, optimized for detecting low-signature targets such as shielded helicopters and UAVs [14].
- A Russian triple-band optical seeker combining mid-IR, near-IR, and UV channels was developed in the mid-1990s to overcome limitations of earlier systems and expand MANPADS operational capabilities [15].

Missile launch warning systems operating in the solar-blind UV region and UV protection channels in MANPADS seekers are representative applications of scattered UV radiation in military contexts. However, due to the classified nature of military technology, related research is rarely published in open literature.

Considering this, the present dissertation focuses on the following research directions:

- Investigation of UV radiation attenuation in the atmosphere.
- Application of photon-counting detectors for measuring background UV radiation.
- Execution of field measurements and detection analysis, including:
    - Determination of detection range for UV radiation emitted by missile plumes in the solar-blind region.
    - Evaluation of airborne target detection using negative contrast imaging in the near-UV range.

The research contents and corresponding results will be presented in detail in the following chapters of this dissertation.

## 2. Aim and structure of the thesis

### 2.1. Aim of the thesis

The aim of this thesis is to investigate the characteristics and propagation of ultraviolet (UV) radiation in the atmosphere and its potential of applications in missile warning and airborne target detection.

As at low altitudes the level of UV radiation in solar-blind region is low, to measure UV background radiation in this region a sufficiently sensitive detector is necessary, so the measurement device with photon-counting UV sensors is proposed, built and applied. UV background radiation in 250-295 nm band for various atmospheric conditions and daytime is measured. Next the study evaluates the detectability of missile exhaust plumes in the above solar-blind UV region. The detection of airborne targets using negative contrast imaging in the near-UV range (300–400 nm) is also examined and the ranges are determined.

### 2.2. Structure of the thesis

The content of doctoral dissertation was divided into 11 sections:

**Section** 1. Introduction

**Section** 2. Aim and Structure of the thesis

**Section** 3. Radiation and UV signature

**Section** 4. UV radiation in the Earth's atmosphere and its attenuation

**Section** 5. Factors Affecting Surface UV Radiation and Methods for UV Radiation Measurement

**Section** 6. Photon counting detector used in measurement of UV (250-295nm) background

**Section** 7. Background UV radiation.

**Section** 8. UV negative contrast of aircraft in 300-400 spectrum

**Section** 9. Range analysis of detection of UV radiation emitted by rocket plumes

**Section** 10. Conclusions

**Section** 11**.** References

### 3. Radiation and UV signature

### 3.1. The Ultraviolet definitions and classification

Ultraviolet radiation is a form of electromagnetic wave, with a wavelength longer than X-rays and shorter than the wavelength of the visible region. The wavelength of UV radiation ranges from 10 nm to 400 nm. Thus, the spectrum of UV waves lies between X-rays and visible light. The relationship between UV radiation in the electromagnetic spectrum is shown in Figure 3.1.

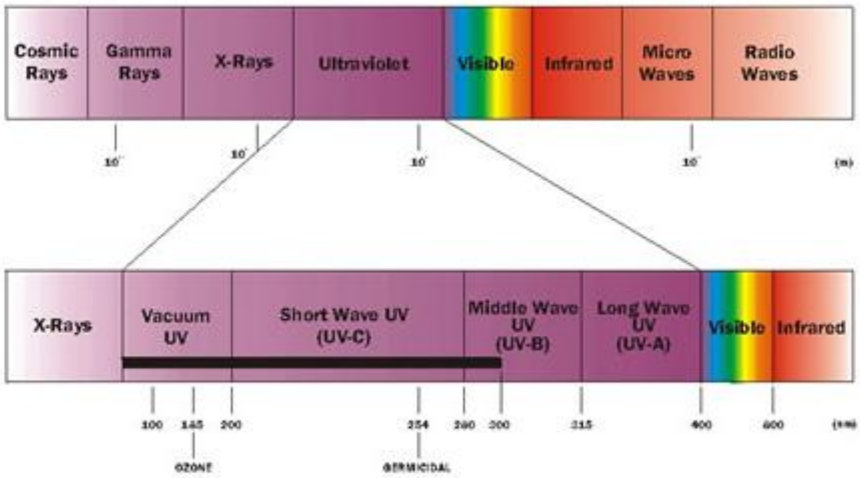


*Fig. 1. Ultraviolet in the electromagnetic spectrum [16]*

**- UV classification**

Electromagnetic wave radiation is subdivided into several subspectral ranges, there are two commonly used classifications based on material properties. The physics and effects of UV radiation in biology and medicine.

Generally, Ultraviolet radiation in scientific fields is classified [17] into:

+ Near Ultraviolet-NUV: This region has wavelength values in the range of 300-400 nm. Extends from the shortwave wavelength of the visible region to the limit of the short wavelength at which solar radiation can reach the earth's surface

+ Middle Ultraviolet -MUV: The MUV radiation has a wavelength range of approximately 300 to 200 nm. Most of the solar radiation in this spectrum is absorbed in the atmosphere by ozone molecules. The 300 nm approximation is the short wavelength limit at which solar radiation cannot reach the earth's surface.

+ Far Ultraviolet-FUV: This is the region with a wavelength between 200nm and 122 nm. In this region, solar radiation is strongly absorbed by the oxygen molecule.

+ Vacuum Ultraviolet-VUV This region includes wavelengths between about 200 nm and 10 nm. The vacuum in the name refers to the act that ground-level instruments are usually placed under a vacuum to obtain sufficient light transmission in this region.

+ Extreme Ultraviolet-EUV The extreme ultraviolet, is defined here as 121nm to 10nm. The EUV solar radiation is responsible for photoionization at ionospheric altitudes.

In biology and medicine, the most widespread is classification, which partitions the UV spectral band into three regions with different wavelengths: UVA: 315– 400 nm, UVB:280–315 nm, and UVC:100–280 nm.

UV-A radiation has a biological effect that is very weak and has almost no negative consequences on living things or human skin, etc. Most of the solar radiation in the UV-A spectrum reaches the surface. This means that the UV-A radiation is not absorbed by molecules present in the atmospheric composition.

Most UV-B radiation is absorbed by the ozone layer of the atmosphere and only 6% reaches the Earth's surface, but this radiation has biological effects on the human body such as causing skin burns, negative effects on the retina of the eye as well as to the immune system, etc.

The UV-C radiation is completely absorbed by oxygen and ozone molecules in the atmosphere, No solar UV-C radiation reaches the Earth's surface.

The ISO-21348 standard on space environment (natural and artificial) - process for determining solar irradiances gives the classification for the UV radiation shown in table 1.

Table 1.Classification of ultraviolet radiation according to the data of [18]

| **Designation** | **Abbreviation** | **Wavelength, nm** |
|---|---|---|
| Near Ultraviolet | NUV | 300nm $< \lambda <$ 400nm |
| Middle Ultraviolet | MUV | 200nm $< \lambda <$ 300nm |
| Far Ultraviolet | FUV | 122nm $< \lambda <$ 200nm |
| Vacuum Ultraviolet | VUV | 10nm $< \lambda <$ 200nm |
| Extreme Ultraviolet | EUV | 10nm $< \lambda <$121nm |
| Ultraviolet A | UV-A | 315 nm $< \lambda <$ 400nm |
| Ultraviolet B | UV-B | 280 nm $< \lambda <$ 315nm |
| Ultraviolet C | UV-C | 100 nm $< \lambda <$ 280nm |

### 3.2. Fundamental Laws of Radiation

**Plank's law**

A blackbody is an idealized physical object that absorbs all incidental electromagnetic radiation without any reflection or scattering. Planck's law of radiation describes the spectral distribution of the radiation emitted by the blackbody at a specific temperature T [19] :

$$M_\lambda(T) = \frac{2\pi h\, c^2}{\lambda^5\left(e^{\frac{hc}{\lambda kT}} - 1\right)} = \frac{c_1}{\lambda^5\left(e^{\frac{c_2}{\lambda T}} - 1\right)} \quad (1)$$

Where: $M_\lambda(T)$ is the spectral radiant exitance with the unit $(w \cdot m^{-2} \cdot \mu m^{-1})$

h is Planck's constant

c is the velocity of light

T is the absolute temperature in degree Kenvil.

λ is the wavelength in $\mu m$

$c_1 = 2\pi\, hc^2 = 3.7418 \times 10^8 (w \cdot m^{-2} \cdot \mu m^4)$ is the first radiation constant.

$c_2 = \frac{h.c}{k} = 1.4388 \times 10^4$ (μm · K) is the second radiation constant.

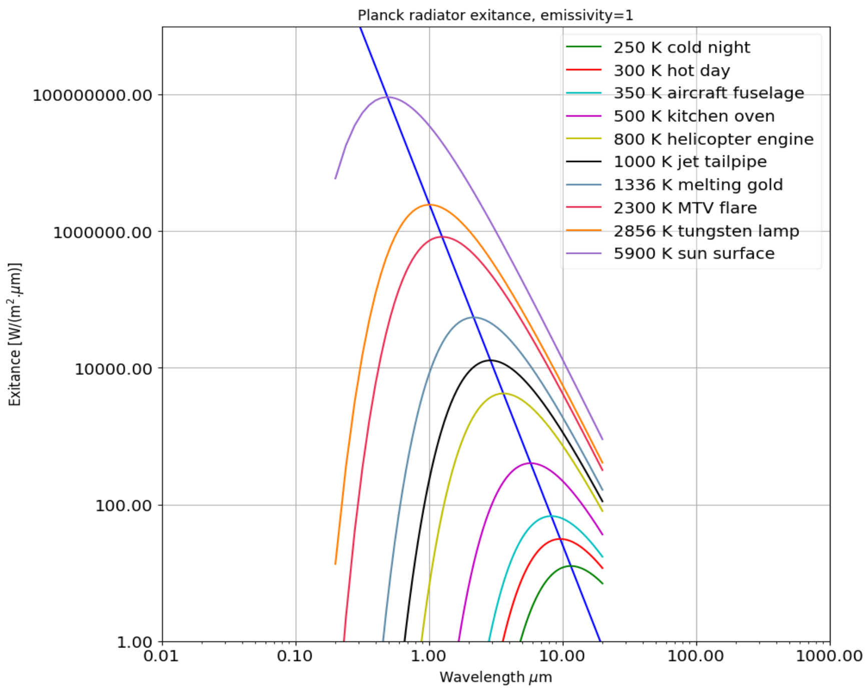


*Fig. 2. Blackbody radiation curves with absolute temperature as indicated*

**Wien's Displacement Law**

The curve in Figure 2 represents the spectral characteristics of a blackbody at various temperatures. It shows that for each specific temperature the Planck curve has only one peak value. The equation expresses the relationship between the temperature of the blackbody and the wavelength at which its emitted radiation reaches a maximum. The straight line connecting the peaks of the Planck curves at different temperatures is illustrated in Figure 2. The peak value corresponding to each curve is calculated using the following expression:

$$\lambda_m = 2897/T \tag{2}$$

Where: - $\lambda_m$ is the wavelength (in micrometers μm) at which the pick emission intensity occurs.

- T is the temperature of the blackbody (in degrees Kelvin, K).

- 2897 is Wien's constant (in $K \cdot \mu m$).

Wien's displacement law states that the hotter an object is, the shorter the wavelength at which it emits radiation at maximum intensity.

**The Stefan–Boltzmann Law**

The total radiation emitted by a blackbody is calculated using the Stefan–Boltzmann law.

$$M(T) = \int_0^\infty M_\lambda(T)d\lambda = \int_0^\infty \frac{2\pi h\, c^2}{\lambda^5\left(e^{\frac{hc}{\lambda kT}} - 1\right)} d\lambda = \frac{2k^4\pi^5\pi}{15c^2h^3} T^4 = \sigma\, T^4 \tag{3}$$

Where,$\sigma$ = 5.6697 x $10^{-12}$ ($Wcm^{-2}K^{-4}$) is Stefan-Boltzmann's constant.

M(T) is the blackbody exitance radiation in [$w/m^2$], and temperature T in [K].

**Properties of Radiation:** Radiation properties include the following coefficients: emissivity, absorptivity, reflectivity, and transmissive.

Emissivity: Emissivity is defined as the ratio between the monochromatic radiative intensity emitted by the object and that emitted by a corresponding blackbody.

$$\varepsilon_\lambda = \frac{I_\lambda(\text{emitted})}{B_\lambda(T)} \tag{4}$$

A blackbody has an emissivity equal to 1, while a graybody has a constant emissivity between 0 and 1. In contrast, a selective radiator is defined as having an emissivity that varies with wavelength.

When radiant energy is incident on a material, three processes occur: reflection, absorption, and transmission. According to the law of energy conservation, these three quantities are as follows:

$$\alpha_\lambda + r_\lambda + \tau_\lambda = 1 \tag{5}$$

where:

- $\alpha_\lambda$ is absorptance: $\alpha_\lambda = \frac{I_\lambda(\text{absorbed})}{I_\lambda(\text{incident})}$ (6)

- $r_\lambda$ is reflectance $r_\lambda = \frac{I_\lambda(\text{reflected})}{I_\lambda(\text{incident})}$ (7)

- $\tau_\lambda$ is transmittance: $\tau_\lambda = \frac{I_\lambda(\text{Transmitted})}{I_\lambda(\text{incident})}$ (8)

### 3.3. Ultraviolet signature

Ultraviolet radiation in the background originates from various sources, including both natural and artificial ones. In atmospheric background, the primary natural source of UV radiation is solar radiation. In addition, there are several types of artificial sources that may be present, such as high-pressure street lighting, runway beacons, arc sources from welding machines, hot flashes from artillery projectiles, corona discharge on high-voltage power transmission lines, power plants, substations, flares released from aircraft to protect platforms against infrared-guided missiles, missile explosions, and more. These disturbances are complex and difficult to control, causing significant interference with UV signal and target detection applications. Within the scope of this dissertation, several UV signals will be introduced from the following sources: solar, aircraft, missile plumes, and flares.

#### 3.3.1. Solar UV radiation

The primary source of UV radiation in the atmosphere is the Sun [19]. The intensity of the UV reaching the Earth's surface depends on concentration of the atmospheric ozone, the Sun's position over the Earth's surface, height over the sea level, atmospheric compositions, cloud covering, degree of UV-radiation reflection from surface (of water, soil), etc [20], [21].

Solar constant: The amount of total solar power reaching the top of the atmosphere (TOA)-the upper boundary of the atmosphere (~100 km), where radiation has not yet been attenuated by the atmosphere - is called the solar constant, with a rounded mean value of $1366\ W \cdot m^{-2}$ [22].

The spectrum of solar radiation is considered closely approximate to that of a blackbody at a temperature of 5800 K [7]. Figure 3 shows the solar radiation spectrum at the top of the atmosphere based on data from the ASTM E-490 standard, other curve represents the radiation spectrum of a blackbody at 5800 K, calculated using Planck's equation.

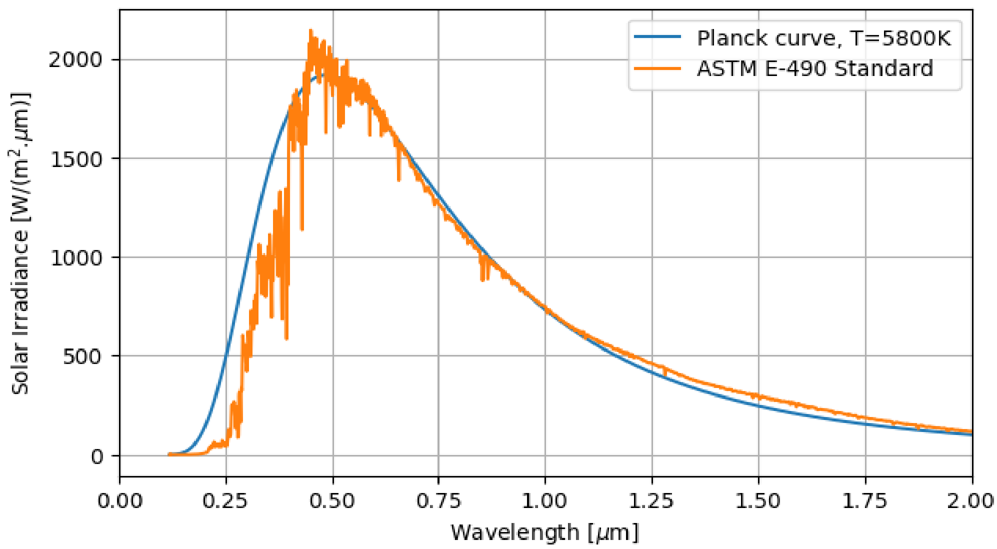


*Fig. 3. Solar Irradiation with data from ASTM E-490 and Planck flux with a temperature of 5800 K*

Based on the data presented in Figure 3, it can be observed that solar radiation in the ultraviolet region (wavelengths < 0.4 μm) accounts for approximately 10% of the total solar radiation, about 40% falls within the visible region, and around 50% is in the infrared region.

A comparison between the two curves, 'ASTM E490 Standard' and 'Planck curve, T = 5800 K', shows that in the ultraviolet region, the solar radiation does not fully match the blackbody radiation at a temperature of 5800 K. Figure 4 provides a detailed illustration of the solar spectrum in the range from 0.1 μm to 0.4 μm, along with Planck curves at temperatures of 4700 K, 5000 K, and 6000 K.

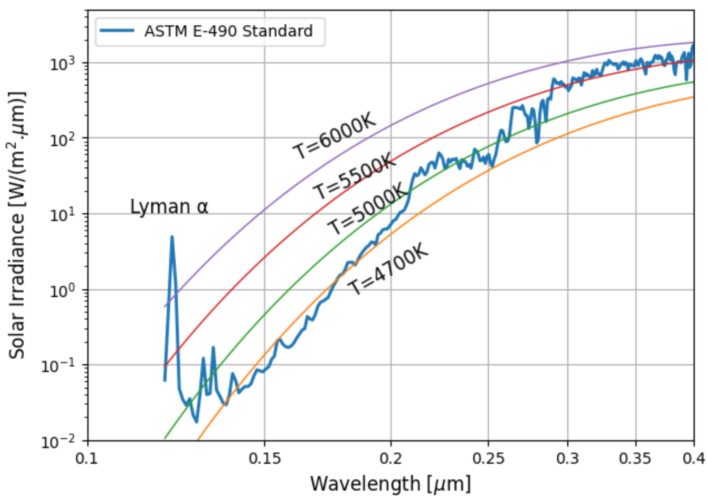


*Fig. 4. Solar radiation at the top of the atmosphere in the ultraviolet region and the Planck curves for temperatures of 4700 K, 5000 K, 5500 K, and 6000 K (logarithmic scale).*

While ultraviolet radiation makes up about 10% of the total solar radiation at the top of the atmosphere, only a small portion of it reaches the Earth's surface approximately 94% in the UV-A range and just 6% in the UV-B range. Wavelengths below 300 nm are entirely absorbed by the atmosphere, with the cutoff point primarily governed by the concentration of ozone in the stratosphere [20], [23]. The radiation intensity curve of sunlight in Earth's atmosphere and sea level is shown in figure 5.

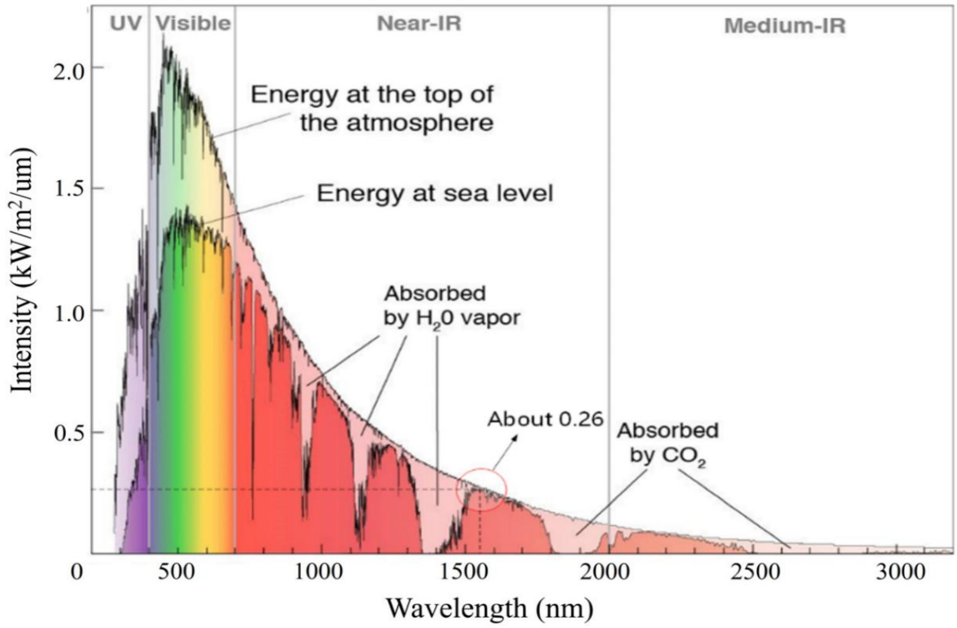


*Fig. 5. Spectral irradiance of the Sun at sea level [24]*

### 3.3.2. UV missile plume signatures

A significant portion of the radiative flux emitted from the flame and rocket engine originates in the infrared (IR) spectrum, primarily due to the hot gases generated in the combustion chamber and the exhaust gases expelled through the nozzle. These gases interact with ambient air, resulting in post-combustion reactions.

The main components of solid rocket propellant include solid aluminum fuel, ammonium perchlorate, and organic binders such as HTPB (hydroxyl-terminated polybutadiene) [25]. To enhance thrust, various additives such as boron and zirconia particles are also included [26].

Rocket exhaust plume contains a variety of chemical species, including CO, $CO_2$, $C_2$, CH, CN, $H_2O$, OH, NO, etc. [10]. The combustion of fuel particles produces high-temperature metal oxide particles (with temperatures in the range of 2000–3000 K) as well as soot. These particles are major sources of thermal radiation in the exhaust plume [27].

Ultraviolet signature of a rocket engine consists of several main components:

- Continuous thermal emission caused by the high temperature of metal oxide particles and soot.
- Strong UV emissions around 306 nm, produced by recombination reactions of atomic oxygen and hydrogen

This emission is particularly prominent in the 306–309 nm wavelength range [10–11,13].

- CO + O chemiluminescence, which emits continuous UV radiation in the 250–290 nm range. The intensity of this chemiluminescent emission depends on the concentrations of CO and O, and its temperature dependence has been determined experimentally [26,28].

The relationship between chemiluminescent intensity, temperature, and wavelength is illustrated in Figure 6.

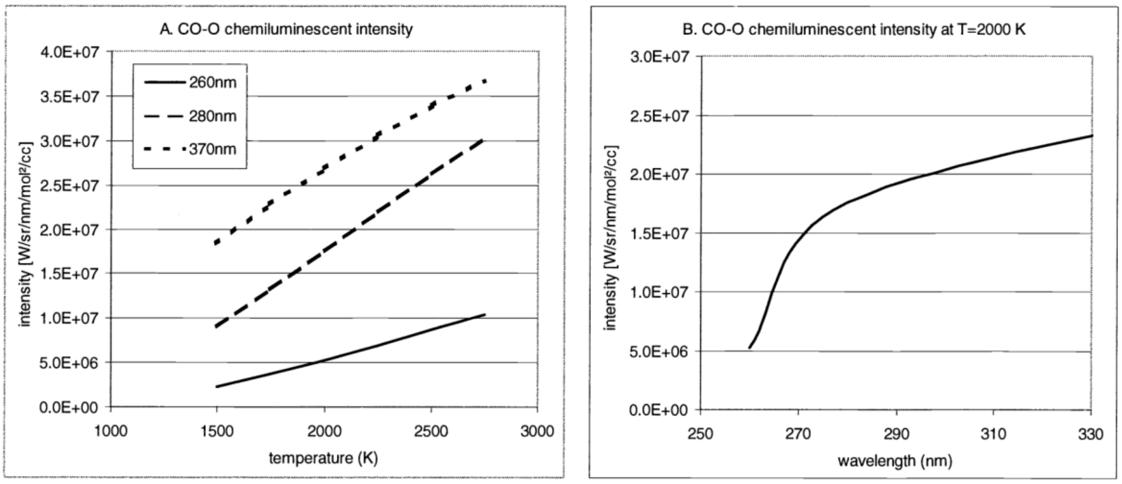


*Fig. 6. Intensity of the CO-O chemiluminescence as a function of temperature (a) and wavelength (b) [13]*

Rocket motor plumes emit significant levels of radiation in the 270-290 UV range. This UV signal consists of a continuum from the thermal emission of solid particles and photochemical CO/O, and the band of molecular emission from some kind of hydroxyl predominance

### 3.3.4. Airplane signature

All components of an aircraft emit or reflect selective radiation across different spectral regions. The primary emitted radiation originates from thermal emissions of the aircraft's engine and exhaust plume. These sources are characterized by their intensity, spectral distribution, and the propagation of radiation through the atmosphere to the sensor

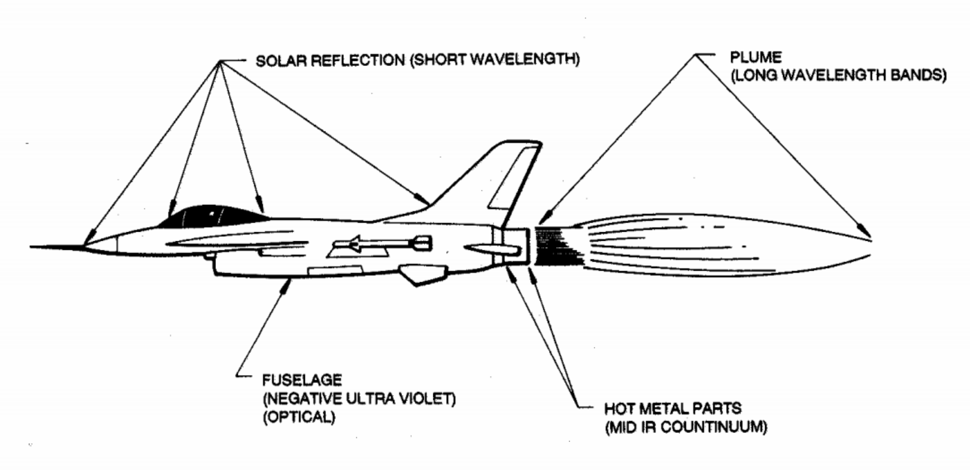


*Fig. 7. Sources of radiation on aircraft [29]*

Aircraft primarily emit infrared (IR) signatures, with the main sources being continuous thermal emission from hot engine components and the exhaust plume. The temperatures of these components vary by location and engine operating mode, including:

- Combustion chamber: 1500–2000 K
- Nozzle: 1200–1800 K
- Afterburner mode: up to 2400–2600 K
- Exhaust plume downstream of the nozzle: 800–1200 K [30–32].

In addition, the aircraft fuselage can become heated due to atmospheric friction, scattering, and reflection of solar and terrestrial infrared radiation.

The UV signatures of aircraft include the following major sources:

- High-temperature emission components: According to Planck's Law, elevated temperatures shift the emission peak toward shorter wavelengths, leading to the presence of radiation in the UV region.
- Chemiluminescence from the exhaust gases, with emissions observed in the 200–400 nm range [33]. Strong UV emissions have been recorded in the 200–325 nm range from JP-4 fuel combustion in an F404 engine operating in afterburner mode, as shown in Figure 6 [29].
- Additionally, the aircraft body blocks solar UV radiation, making the aircraft appear darker than the sky background in the UV spectrum - a phenomenon known as negative contrast or silhouetting. This effect is counterintuitive when

compared to observations in the IR or visible spectrum, where the object typically appears brighter than the background due to its thermal emission.

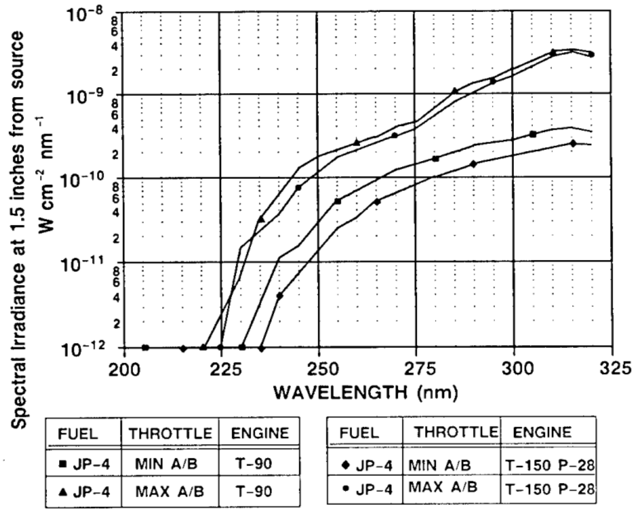


*Fig. 8. UV spectral data from F404 engine [29]*

### 3.3.5. Flares

The emergence of infrared-guided missiles has led to the development of countermeasure systems aimed at deceiving or neutralizing such threats. Among the most widely used countermeasures deployed across various airborne platforms are decoys, including infrared flares and electronic jamming systems that interfere with the missile seeker.

Infrared flares are a type of passive countermeasure deployed from aircraft to divert heat-seeking (IR-guided) missiles by creating false thermal targets. The main objective of flares is to mimic or exceed the infrared signature of the aircraft, thereby attracting the missile seeker away from the actual platform. These flares emit radiation not only in the infrared spectrum, but also in the ultraviolet range.

**Conventional Flares**:

Magnesium-Teflon (MT) and Magnesium-Teflon-Viton (MTV) flares are commonly used to protect various airborne platforms (such as aircraft and helicopters) against infrared-guided surface-to-air missiles. These countermeasures work by:

- Creating a false target within the missile's field of view by generating an intense thermal source. The combustion temperature of the flare composition can reach up to 2200 K, and when magnesium is oxidized, it may exceed 3100 K [34]. This results in strong IR radiation with peak emission in the 1–3 μm range [35].

- During the combustion of MTV pyrotechnic compositions, UV emission has been observed in the 340–370 nm range, attributed to gaseous MgF [36].

Figure 9 compares the emission spectrum of a flare decoy with the hot components of an aircraft [37]. The high combustion temperature of flares ensures an intensity sufficient to mislead nearly all infrared-guided missiles that lack advanced counter-countermeasure capabilities (i.e., that operate with single-color seekers).

The missile seeker is deceived by the intense IR energy present in its field of view, causing it to lock onto the decoy instead of the actual aircraft, allowing the platform to evade the missile attack effectively.

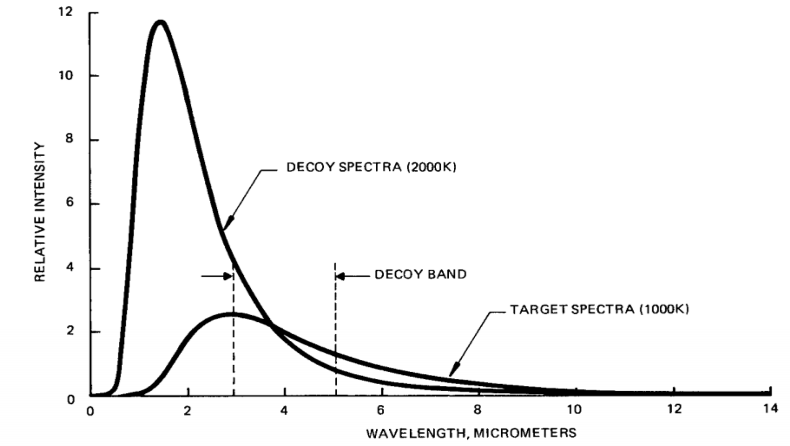


*Fig. 9. Typical decoy/target spectra [37]*

Thus, conventional flares emit UV radiation in the 340–370 nm range and thermal infrared radiation corresponding to a combustion temperature of approximately 2200 K.

**Advanced Flares:**

Modern flares are designed not only to reproduce the spectral emission characteristics of real aircraft targets, but also to defeat discrimination algorithms used in modern infrared-guided missile seekers. These algorithms may include rise-time analysis, dual-band spectral discrimination (IR/UV), and area temperature matching. As such, flares have become an essential active defense measure in protecting aircraft from modern infrared missile threats [38].

Some key types of advanced flares include:

- Spectrally Adapted Payloads (SAPs): SAPs are flares engineered so that their infrared emission spectrum closely resembles that of the intended target, such as the jet engine exhaust of an aircraft. This design aims to deceive modern IR seekers with spectral discrimination capabilities.

- Spectrally Balanced Flares [39],[40]: The chemical composition of these flares is optimized so that, during combustion, they generate a specific intensity ratio between two spectral bands:

- α-band (2–3 μm)
- β-band(3–5 μm)

This ratio, denoted as $\theta = I_a / I_\beta$, typically falls between 0.5 and 0.8, which closely matches the spectral characteristics of actual aircraft engine plumes.

Additionally, SAPs are designed to operate at lower temperatures, which helps suppress ultraviolet emissions, thereby reducing the risk of detection by dual-color seekers capable of IR/UV discrimination.

- Liquid Pyrophoric Flares [38],[41]: These flares represent one of the most advanced infrared countermeasure technologies, developed to defeat sophisticated seekers such as Imaging Infrared (IIR) and multi-band seekers. They offer several key advantages:

- Use of pyrophoric fuels, typically Triethylaluminum or Trimethylaluminum, which ignite spontaneously upon contact with air—eliminating the need for an oxidizer.
- Strong emission in the 3–5 μm band, matching the typical spectral signature of jet engines, improving target mimicry.
- Wide spatial dispersion of radiation—unlike traditional flares that appear as concentrated points, these flares form a broad radiating cloud, mimicking a larger target area.
- Short burn duration with high intensity, ensuring rapid response and effective disruption of infrared sensors, even under emergency combat conditions.

Other types of flares include:

- Aerodynamically Stabilized Flares: designed to maintain flight stability, improving flare placement and effectiveness.
- Cocktail Flare Systems: combining multiple flare types to broaden spectral coverage and maximize jamming effectiveness against diverse threats such as IIR-guided missiles, spectrally discriminating seekers, and multi-band detection systems.

These systems enhance flare performance in modern combat environments by optimizing flight behavior, emission spectrum, and countermeasure adaptability [38].

# 4. UV radiation in the Earth's atmosphere and its attenuation

The Earth's atmosphere consists of many components and is relatively complex. Temperature, pressure, and the concentration of substances in the atmosphere vary with altitude. The attenuation of radiation during its propagation through the atmosphere is influenced by both absorption and scattering by molecules as well as particles, etc.

To gain a better understanding of the mechanisms of radiation attenuation in the atmosphere, this chapter presents the following key topics:

- The structure and composition of the atmosphere
- Absorption and scattering by gas molecules
- Absorption and scattering by particles (Mie scattering)
- The radiative transfer equation and models for calculating solar radiation at the Earth's surface

## 4.1. Structure of the Atmosphere

The Earth's atmosphere is divided into several layers based on its thermal structure, including:

- The troposphere
- The stratosphere
- The mesosphere
- The thermosphere

These layers are defined according to changes in temperature with altitude [42].

In each layer, the atmospheric composition, molecular concentrations, particle density distribution, temperature, and pressure all vary with height.

The thermal structure of the atmosphere is represented by six standard models, each corresponding to different geographic regions on Earth's surface. These models are described in detail in U.S. Standard Atmosphere, 1976 [42] and U.S. Standard Atmosphere Supplements, 1966 [43], and include:

- Tropical (15°N Annual Average)
- Mid-Latitude Summer (45°N, July)
- Mid-Latitude Winter (45°N, January)
- Sub-Arctic Summer (60°N, July)
- Sub-Arctic Winter (60°N, January)
- U.S. Standard Atmosphere (1976)

The temperature and pressure profiles [42–43] as a function of altitude for the six models are illustrated in Figure 10.

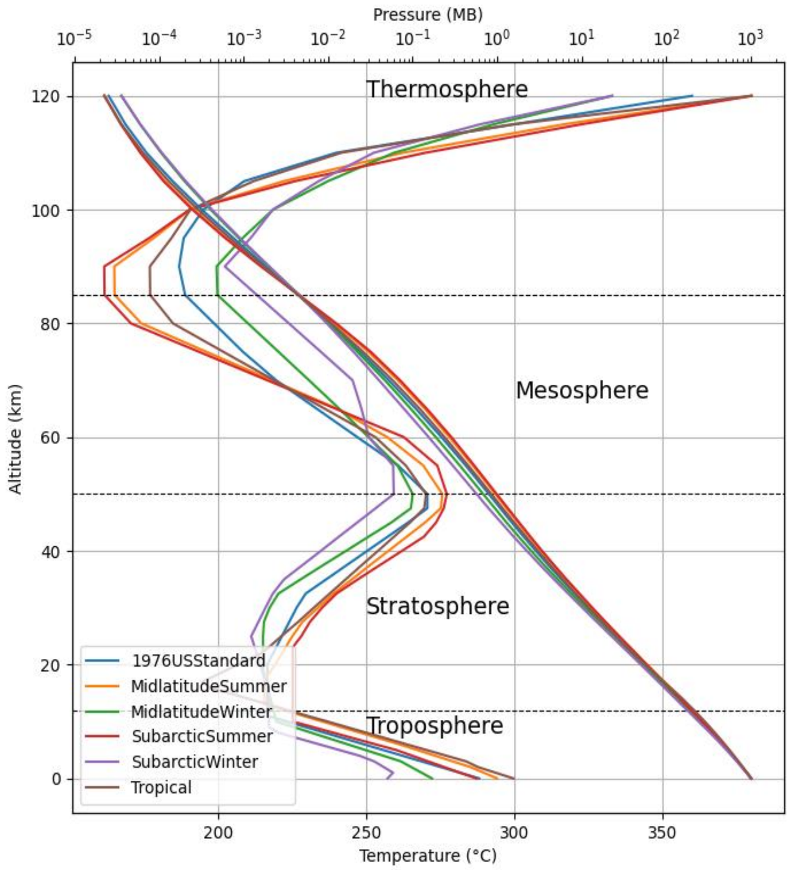


*Fig. 10. Variation of temperature and pressure with atmospheric altitude*

## 4.2. Composition of the atmosphere.

The atmosphere is composed of:

- Gases
- Aerosols
- Water and ice cloud droplets

Atmospheric gases are highly selective in their ability to absorb radiation. Each radioactively active atmospheric gas has a specific absorption spectrum – its own signature. Thus, the abundance of gases in the atmosphere controls the overall spectral absorption.

#### 4.2.1. Gases

The Earth's atmosphere consists of various gases, primarily nitrogen (78.08%) and oxygen (20.95%), along with trace gases and noble gases [44]. Table 2 presents the atmospheric constituents along with their molar masses and volume mixing ratios [45].

Table 2. Concentrations of Uniformly Mixed Gases in the Atmosphere

| **Constituent** | **Molecular weight** | **Fractional concentration by volume** |
|---:|---:|---:|
| Nitrogen ($N_2$) | 28.013 | 78.08% |
| Oxygen ($O_2$) | 32.00 | 20.95% |
| Argon (Ar) | 39.95 | 0.93% |
| Water vapor ($H_2O$) | 18.02 | 0-5% |
| Carbon dioxide ($CO_2$) | 44.01 | 380 ppm |
| Neon (Ne) | 20.18 | 18 ppm |
| Helium (He) | 4.00 | 5 ppm |
| Methane (CH4) | 16.04 | 1.75 ppm |
| Krypton (Kr) | 83.80 | 1 ppm |
| Hydrogen ($H_2$) | 23.02 | 0.5 ppm |
| Nitrous oxide ($N_2O$) | 56.03 | 0.3 ppm |
| Ozone ($O_3$) | 48.00 | 0-0.1 ppm |

##### 4.2.1.1 Absorption by Gas Molecules

When radiation interacts with matter, several phenomena may occur - absorption, scattering, or emission. Absorption results in no secondary radiation being emitted, but rather a reduction in the energy of the incident radiation. This is because the photons are absorbed by atoms or molecules, raising them to a higher energy state. Each photon carries an energy level:

$$E=hc/\lambda \quad (9)$$

Absorption by gas molecules is a complex process, as molecules possess multiple internal energy levels. Depending on the energy of the radiation and the molecular structure of the gas, the absorption spectra may take several forms:

- Continuous absorption spectra (Absorption continua)

- Discrete absorption lines with finite width (Absorption lines)
- Clusters of absorption lines, known as bands (Broadening of absorption lines)

In the ultraviolet region, atmospheric radiation absorption primarily occurs as continuous absorption. In contrast, absorption in the visible and infrared regions typically appears as lines and bands.

For ultraviolet radiation (0.1–0.4 μm), extreme ultraviolet radiation from the Sun carries enough energy to ionize atoms by ejecting electrons - this process is known as photoionization. Such high-energy UV radiation is completely absorbed in the ionosphere, at altitudes above 90 km.

Molecular oxygen absorbs radiation at wavelengths up to 240 nm, leading to its dissociation into two oxygen atoms - a process called photodissociation. The free oxygen atoms generated are essential in forming ozone, which itself can be dissociated by solar radiation up to 310 nm [31].

This photoionization and photodissociation mechanisms are examples of continuous absorption, and the main continuous absorption bands in the atmosphere are listed in the following

Table 3. UV absorption bands in the atmosphere

| **Wavelength range** | **Gas** | **Absorption band** | **Location of absorption** | **Classification of absorption strength** |
|---|---|---|---|---|
| 100-200 | $O_2$ | Schuman-Runge | Thermosphere/ Mesosphere | Very strong |
| 200-242 | $O_2$ | Herzberg | Statosphere | weak |
| 200-400 | $O_3$ | Hartley-Huggins | Statosphere | strong |

The absorption of gas molecules is characterized by the absorption coefficient $ka$, which indicates the ability of a gas to absorb radiation at a specific wavelength. This coefficient is typically calculated using the following expression:

$$k_a = n(z)\sigma_a \quad (cm^{-1}) \tag{10}$$

Where:

-n(z) is the number of density (in [molecules/cm $^3$]) for a specific absorber.

- $\sigma_a$ is the absorption cross section [cm$^2$/molecule]

- z is the altitude of the atmosphere.

The absorption cross-section coefficients of the Schuman-Runge and Herzberg bands of molecular oxygen, the Hartley-Huggins bands of ozone, and other molecular gases such as $N_2O$, $SO_2$, BrO, and OClO are obtained from the HITRAN database [46].

The molecular number density at the Earth's surface under standard conditions is given by: $N_i = \frac{PN_A}{RT} \times C_i \times 10^{-6}$ [molecules/ $cm^3$]

With the standard values:

- $[C_i]$ – Volume mixing ratio of gas i, in [ppmv]
- P=101.325 [Pa]: Standard atmospheric pressure
- T=273.15 [K]: Standard temperature
- $N_A = 6.02210^{23} \times [mol^{-1}]$ : Avogadro's number
- R=8.314 [J/(mol·K)]: Ideal gas constant

a normal absorption optical depth (optical thickness) for a monochromatic wavelength and for a given absorber as follows:

$$\tau(z) = \int_z^\infty k_a dz = \int_z^\infty n(z)\sigma_a dz \quad (11)$$

The vertical optical thickness integrated over the entire atmosphere is:

$$\tau = \int_0^\infty n(z)\sigma_a dz \quad (12)$$

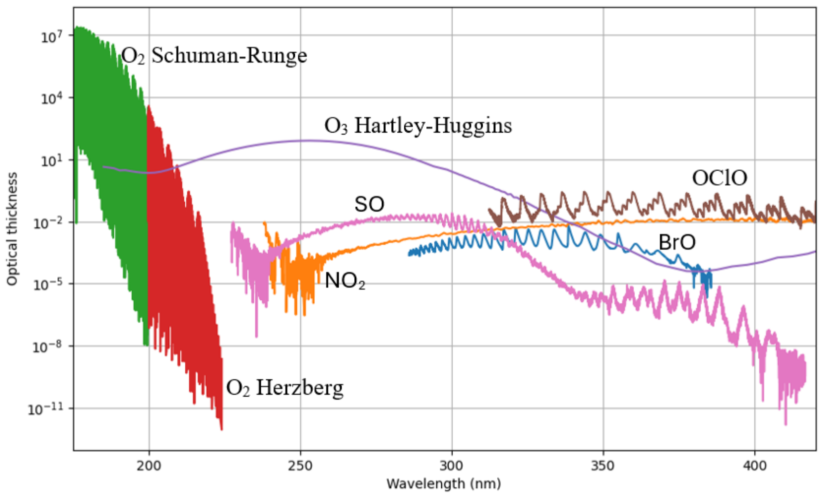


*Fig. 11. Vertical optical thicknesses of main gaseous absorbers in UV*

The calculated results shown in the graph indicate that, in the UV-C wavelength range (100-280 nm), UV radiation is primarily absorbed by oxygen and ozone layer. Other gases play only a minor role.

### 4.2.1.2. Molecular Rayleigh scattering.

The scattering effect depends on the ratio between the size of the scattering particle and the wavelength of light. This is expressed through the size parameter: $x = \frac{2\pi r}{\lambda}$, where *r* is the radius of the spherical scattering particle and *λ* is the wavelength of light. Scattering can be categorized into three regimes:

- $x \ll 1$: Rayleigh scattering (particles much smaller than the wavelength)
- $x \approx 1$: Mie scattering (particles comparable in size to the wavelength)
- $x \gg 1$: Geometric scattering (particles much larger than the wavelength)

The applicability of different scattering models based on particle size and wavelength is illustrated in Figure 12.

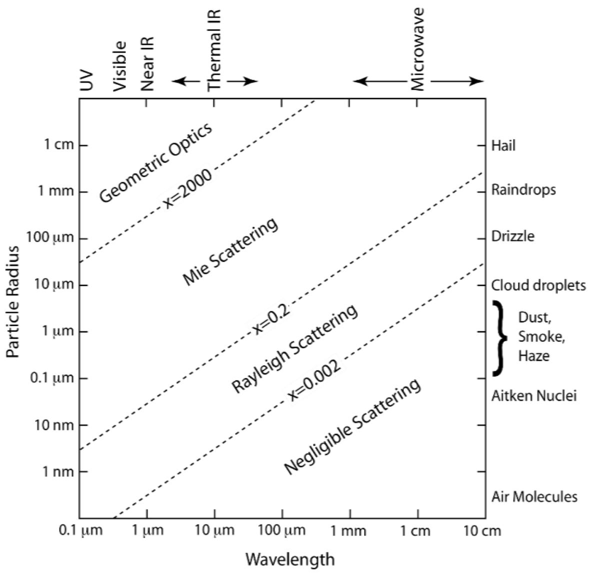


*Fig. 12. Scattering theory model applied according to particle size*

In the atmosphere, particles responsible for scattering range in size from gas molecules (~$10^{-4}$ µm), to aerosols (~1 µm), water droplets (~10 µm), ice crystals (~100 µm), and large raindrops and hailstones (~1 cm) [47].

Based on the model illustrated in Figure 10, it is shown that in the ultraviolet and visible radiation regions (short wavelengths), gas molecules play a dominant role in scattering light, and the applicable scattering model is Rayleigh scattering. Aerosols, clouds, and droplets are subject to Mie scattering.

Rayleigh scattering is an elastic scattering process of electromagnetic radiation that occurs when light interacts with gas molecules whose size is much smaller than the wavelength of the light. The scattering intensity is inversely proportional to the fourth power of the wavelength ($\lambda^{-4}$), meaning that shorter wavelengths (such as blue and violet light) are scattered more strongly than longer wavelengths. Rayleigh scattering consists of three main components: scattering due to molecules, the local field effect, and depolarization caused by the non-spherical shape of the molecules or particles, which is described using the King correction factor. For a gas with known refractive index and King factor, the Rayleigh scattering cross-section as a function of wavelength can be determined by the following expression [48–49]:

$$\sigma(\lambda) = \frac{24\pi^3 (n_s^2 - 1)^2}{\lambda^4 N_s^2 (n_s^2 + 2)^2} \left(\frac{6 + 3\delta}{6 - 7\delta}\right) \tag{13}$$

Where:

- $\sigma$ is the scattering cross section per molecule [$cm^2$/molecules]
- $N_s$ is molecular density [molecules/$cm^3$]
- $n_s$ is refractive index of the gas
- $\lambda$ is wavelength [µm]
- $K(\lambda) = \frac{6+3\delta}{6-7\delta}$ King factor (depolarization term)

For monatomic gases, the King correction factor is K = 1, meaning there is no depolarization. However, for diatomic and polyatomic gases, this factor deviates from 1 due to molecular anisotropy. Table 4 presents the formulas for calculating the refractive index and the King correction factor for several atmospheric gases.

Table 4. Refractive index and King correction factor for selected atmospheric gases

| Gas | Refractive index | King correction factorrs | Ref. |
|---|---|---|---|
| | $(n - 1) \times 10^8$ | $K(\lambda)$ | |
| Air | $8060.51 + \frac{2480990}{132.274 - \lambda^{-2}} + \frac{17455.7}{39.32957 - \lambda^{-2}}$ | 1.048 | [50], [51] |
| $N_2$ | $5677.465 + \frac{3188187,4}{144 - \lambda^{-2}}$ | $1.034 + \frac{3.17 \times 10^{-4}}{\lambda^2}$ | [48], [52] |
| $O_2$ | $20564.8 + \frac{248289.9}{40.9 - \lambda^{-2}}$ | $1.096 + \frac{1.385 \times 10^{-3}}{\lambda^2} + \frac{1.448 \times 10^{-4}}{\lambda^4}$ | |
| $CO_2$ | $22822.1 + 117.8 \times \lambda^{-2} + \frac{2406030}{130 - \lambda^{-2}} + \frac{15997}{38.9 - \lambda^{-2}}$ | 1.15 | [52] [53] |

From equation (6), the Rayleigh scattering cross-section coefficients of several atmospheric gases can be calculated. The results are presented in Figure 13.

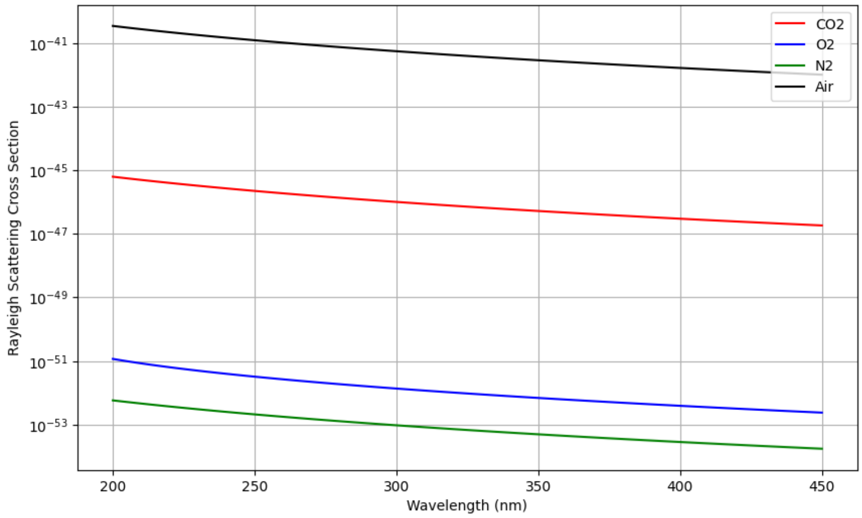


*Fig. 13. Rayleigh scattering cross-section of $CO_2$, $O_2$, $N_2$, and dry air*

The Rayleigh scattering phase function:

$$P(\Theta) = \frac{3}{4}(1 + \cos^{2\Theta}) \qquad (14)$$

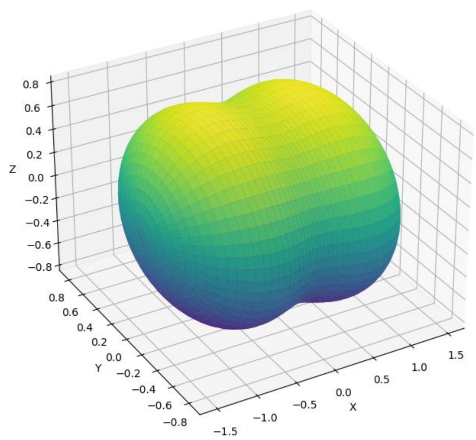


*Fig. 14. Phase function plot in polar coordinates*

Rayleigh scattering is symmetrically distributed in both forward and backward directions

Using this scattering cross-section, one can calculate the optical depth of the entire atmosphere due to molecular scattering as:

$$\tau(\lambda) = \sigma_s(\lambda) \int_0^{top} N(z)\, dz \qquad (15)$$

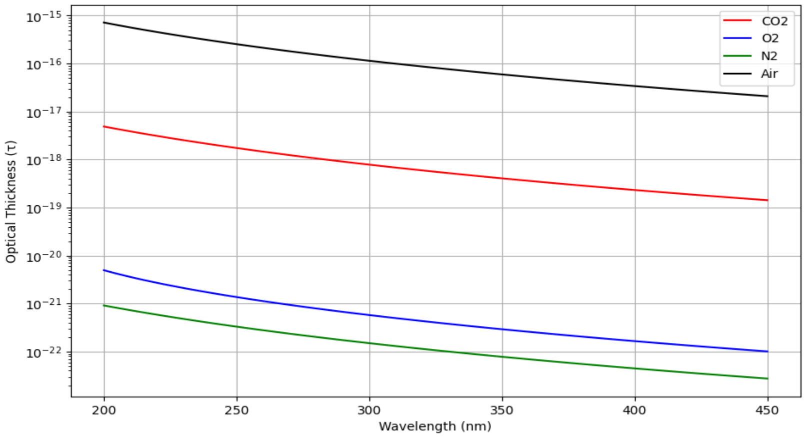


*Fig. 15. Vertical optical thickness of atmospheric gases due to Rayleigh Scattering*

**4.2.2. Aerosols**

4.2.2.1. Mie Scattering: Absorption and Scattering by Aerosols, Clouds, and Droplets

Mie scattering is based on the exact solution of Maxwell's equations for light scattering by a homogeneous spherical particle. Unlike Rayleigh scattering, which occurs when particles are much smaller than the wavelength of light, Mie scattering arises when the particle size r is comparable to or larger than the wavelength λ.

Mie theory assumes that the scattering particles are spherical and homogeneous, meaning that the refractive index has a single value at a given wavelength [54]. The Mie coefficients $a_n$ and $b_n$ describe the scattering of light waves by a spherical particle. They are defined as follows:

$$a_n = \frac{m\psi_n(mx)\psi_n'(x) - \psi_n(x)\psi_n'(mx)}{m\psi_n(mx)\xi_n'(x) - \xi_n(x)\psi_n'(mx)}$$
$$b_n = \frac{\psi_n(mx)\psi_n'(x) - m\psi_n(x)\psi_n'(mx)}{\psi_n(mx)\xi_n'(x) - m\xi_n(x)\psi_n'(mx)} \quad (16)$$

Where:

- $x = \frac{2\pi r}{\lambda}$ is the size parameter.
- m=n+ik is the complex refractive index of the particle (consisting of the real part n and the imaginary part k, which describes absorption)
- $\psi_n(x)$ is the spherical Bessel function of the first kind.
- $\xi_n(x) = \psi_n(x) + i\chi_n(x)$ It is the spherical Hankel function (a combination of Bessel functions of the first and second kind).
- $\psi_n'(x), \chi_n'(x)$ are the first derivatives of the above functions.

In Mie theory, scattered light is described through the scattering, absorption, and extinction cross-section coefficients (units: [m²]).

Extinction cross-section:

$$\sigma_{ext} = \frac{2\pi}{k^2}\sum_{n=1}^{\infty}(2n+1)\Re(a_n + b_n) \tag{17}$$

Where:

- k: The wavenumber in the surrounding medium, defined as $k = \frac{2\pi}{\lambda}$, where λ is the wavelength of light.

- $\Re(a_n + b_n)$The real part of the sum of Mie coefficients $a_n$ *and* $b_n$

Scattering cross-section – Describes the extent to which light is scattered by a particle:

$$\sigma_{sca} = \frac{2\pi}{k^2}\sum_{n=1}^{\infty}(2n+1)(|a_n|^2 + |b_n|^2) \tag{18}$$

Where: $a_n, b_n$ are Mie scattering coefficients, representing the electric and magnetic contributions to the scattering process (see Equation (8)).

Absorption cross-section – Describes the amount of light absorbed by the particle:

$$\sigma_{abs} = \sigma_{ext} - \sigma_{sca} \tag{19}$$

To facilitate comparison, efficiency factors are defined as:

Scattering efficiency: $Q_{sca} = \frac{\sigma_{sca}}{\pi r^2}$

Absorption efficiency: $Q_{abs} = \frac{\sigma_{abs}}{\pi r^2}$

Extinction efficiency: $Q_{ext} = \frac{\sigma_{ext}}{\pi r^2}$

These factors are normalized by the geometric cross-sectional area of the particle, enabling comparison between particles of different sizes.

Mie Phase Function:

The Mie phase function, denoted as P(θ), describes the angular distribution of scattered light as a function of the scattering angle θ. In other words, it gives the probability that light will be scattered in a specific direction after interacting with a particle.

The asymmetry parameter g is used to quantify the average scattering direction and is defined by the following equation:

$$g = \frac{\int_{-1}^{1} \cos\theta \, P(\theta) \, d(\cos\theta)}{\int_{-1}^{1} P(\theta) \, d(\cos\theta)} \tag{20}$$

In which:

– θ is the scattering angle, and P(θ) is the phase function.

– g>0: Light is predominantly scattered in the forward direction.

– g<0: Light is predominantly backscattered.

The figure below shows an example of calculated Mie parameters: extinction efficiency Qext, scattering efficiency Qsca , absorption efficiency Qabs, and the asymmetry parameter g, for water droplets with a complex refractive index of n=1.33+0.4i, and particle sizes ranging from 0.01 μm to 100 μm in the UV spectral range (0.2–0.4 μm).

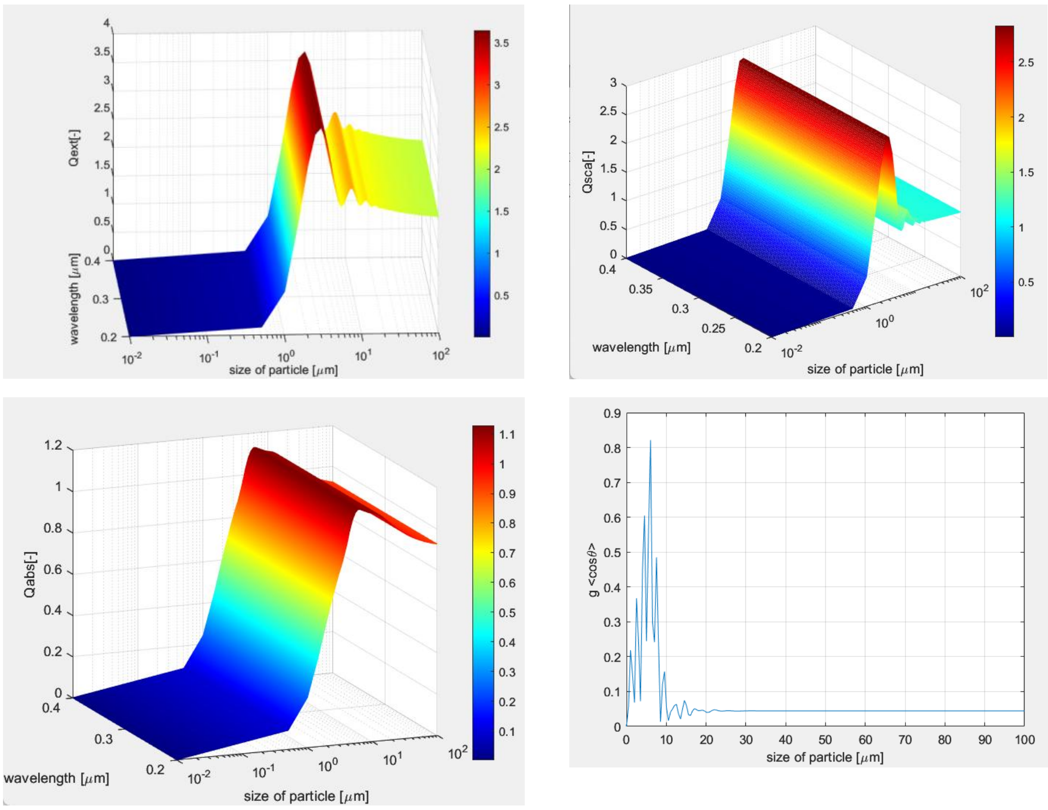


*Fig. 16. Extinction efficiency (Qext), scattering efficiency (Qsca), absorption efficiency (Qabs), and asymmetry parameter (g) of water vapor*

#### 4.2.2.2. Aerosols and Computational Modeling

Aerosols are produced in Earth's atmosphere from various sources. They are natural or anthropogenic chemical compounds- both inorganic and organic. Aerosol particles are introduced into the atmosphere either directly from surface sources or through chemical reactions among atmospheric gases triggered by solar radiation (i.e., photochemical processes). Surface-level sources include human activities (industrial zones, vehicles, etc.) and natural phenomena (wildfires, volcanic eruptions, etc.). Sea salt aerosols are formed at the ocean surface.

To analyze or simulate how aerosols affect the propagation of radiation in the atmosphere - such as changes in direction, intensity, etc. - aerosols must be modeled. An aerosol model represents its nature, size distribution, and spatial profile in the atmosphere. Vertical characteristics of aerosols are modeled by dividing the atmosphere into four altitude regions, each associated with a specific aerosol type [55]:

- Boundary layer (0–2 km): Includes water-soluble particles, dust-like particles, soot, and sea salt.
- Upper troposphere (2–10 km): Aerosols consist of fine particles formed from gas components and a second group of coarse particles.
- Lower stratosphere (10–30 km): Mainly composed of sulfate compounds generated through photochemical reactions, along with volcanic dust and $SO_2$ emissions.
- Upper atmosphere (30–100 km): Predominantly consists of meteoric dust.

Among these, aerosols in the boundary layer are the most variable and are classified into the following basic models [55–57]: Urban, Rural, Remote Continental, and Maritime. The parameters of these boundary layer aerosol models are summarized in Table 5.

Table 5. Basic Aerosol Models in the Boundary Layer [56]

| **Aerosol Model** | **Aerosol Component** | **Percentage by Aerosol** |
|---|---|---|
| Urban | Water-Soluble | 61 |
| | Soot | 22 |
| | Dust-like | 17 |
| Rural | Urban | 80 |
| | Soot | 20 |
| Continental | Dust-like | 70 |
| | Water-Soluble | 29 |
| | Soot | 1 |
| Maritime | Oceanic | 95 |
| | Water-Soluble | 5 |

The aerosol size distribution in the Boundary layer is represented as the sum of three lognormal distributions:

$$\frac{dN(r)}{d\big(log(r)\big)} = \sum_{i=1}^{3} \frac{N_i}{\sqrt{2\pi} log\sigma_i} exp\left\{\frac{-(log(r/R_i)^2}{2(log\sigma_i)^2}\right\} \tag{21}$$

Where:

- N(r) is the cumulative particle number distribution (in $cm^{-3}$).

- r is the particle radius (in $\mu$m)

- $R_i$ is the mean particle radius (in $\mu$m)

- $N_i$ is the integral of the *i*th normal function.

- $log\ \sigma_i$ is a measure of particle polydispersity.

The size distribution parameters of the above aerosol models are presented in tab.6.

Table 6. Size distribution parameters of aerosols [57]

| Aerosol | i | $N_i(cm^{-3})$ | $R_i(\mu m)$ | $log\sigma_i$ |
|---|---|---|---|---|
| **Rural** | 1 | 6.65E3 | 0.00739 | 0.225 |
| | 2 | 1.47E2 | 0.0269 | 0.557 |
| | 3 | 1.99E3 | 0.0419 | 0.266 |
| **Urban** | 1 | 9.93E4 | 0.00651 | 0.245 |
| | 2 | 1.11E3 | 0.00714 | 0.666 |
| | 3 | 3.64E4 | 0.0248 | 0.337 |
| **Remote continental** | 1 | 3.20E3 | 0.01 | 0.161 |
| | 2 | 2.90E3 | 0.058 | 0.217 |
| | 3 | 3.00E-1 | 0.9 | 0.380 |
| **Maritime** | 1 | 1.33E2 | 0.0039 | 0.657 |
| | 2 | 6.66E1 | 0.133 | 0.210 |
| | 3 | 3.06 | 0.29 | 0.396 |

In figure 17. the particle size distribution of various aerosols is presented

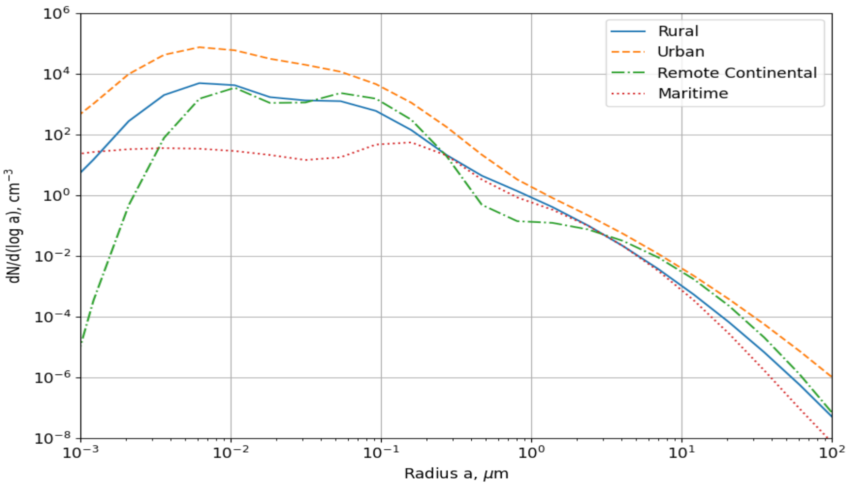


*Fig. 17. Particle size distributions in atmospheric aerosols for different aerosol models*

Refractive Index of Aerosols: According to the aerosol models presented above, the effective refractive index of aerosols is calculated based on the refractive indices and volume fractions of the constituent materials. The effective refractive index is approximately estimated using Bruggeman's effective medium theory. [58]

$$\sum_{i=1}^{N} f_i \frac{n_i^2 - n_{eff}^2}{n_i^2 + 2n_{eff}^2} = 0 \tag{22}$$

In which:

- $n_i$ is the refractive index of the *i-th component*,
- $n_{eff}$ is the effective refractive index of the mixture,
- $f_i$ is the volume fraction of the i-th component, such that:

$$\sum_{i=1}^{N} f_i = 1 \tag{23}$$

The refractive indices of several aerosol components are presented in Table 7 [56].

Table 7. Refractive indices of selected aerosol components

| Wavelength (microns) | Dust-Like | | Water Soluble | | Oceanic | | Soot | |
|---|---|---|---|---|---|---|---|---|
| 0.2 | 1.53 | -7.00E-02 | 1.53 | -7.00E-02 | 1.429 | -2.87E-05 | 1.509 | -0.35 |
| 0.25 | 1.53 | -3.00E-02 | 1.53 | -3.00E-02 | 1.404 | -1.45E-06 | 1.52 | -0.45 |
| 0.3 | 1.53 | -8.00E-03 | 1.53 | -8.00E-03 | 1.395 | -5.33E-07 | 1.74 | 0.47 |
| 0.337 | 1.53 | -8.00E-03 | 1.53 | -5.00E-03 | 1.39 | -1.20E-07 | 1.75 | 0.47 |
| 0.4 | 1.53 | -8.00E-03 | 1.53 | -5.00E-03 | 1.385 | -9.90E-09 | 1.75 | 0.46 |
| 0.486 | 1.53 | -8.00E-03 | 1.53 | -5.00E-03 | 1.383 | -7.90E-09 | 1.75 | 0.46 |
| 0.515 | 1.53 | -8.00E-03 | 1.53 | -5.00E-03 | 1.381 | -3.91E-09 | 1.75 | 0.45 |
| 0.55 | 1.53 | -8.00E-03 | 1.53 | -6.00E-03 | 1.379 | -1.25E-09 | 1.75 | 0.45 |
| 0.633 | 1.53 | -8.00E-03 | 1.53 | -6.00E-03 | 1.377 | -5.62E-09 | 1.75 | 0.43 |
| 0.694 | 1.53 | -8.00E-03 | 1.53 | -7.00E-03 | 1.375 | -1.62E-08 | 1.75 | 0.43 |
| 0.86 | 1.52 | -8.00E-03 | 1.52 | -1.20E-02 | 1.367 | -6.41E-05 | 1.75 | 0.43 |
| 1.06 | 1.49 | -8.00E-03 | 1.49 | -1.70E-02 | 1.355 | -1.41E-4 | 1.75 | 0.45 |

To calculate the extinction coefficient of aerosols (a mixture of various substances), we need to follow these steps:

Input parameters:

- Particle size distribution N(r)
- Effective refractive index of the mixture $n_{eff}(\lambda)$

Compute the cross-section coefficients using Mie theory

– Scattering cross section, $\sigma_s(r, \lambda)$

– Absorption cross section, $\sigma_a(r, \lambda)$

– Extinction cross section, $\sigma_e(r, \lambda)$

– Phase function, $P(\Theta)$

(as a function of a particle size and wavelength)

Calculate the extinction coefficient by integrating over the entire particle size distribution

– Scattering coefficient, $k_s(\lambda)$

– Absorption coefficient, $k_a(\lambda)$

– Extinction coefficient, $k_e(\lambda)$

– Phase function, $P11(\Theta)$ (as a function of the wavelength).

**Integration over the size distribution N(r)**

For a given type of particle characterized by the size distribution N(r), the extinction, scattering and absorption coefficients are determined as:

$$k_{e,s,a}(\lambda) = \int_0^\infty \sigma_{e,s,a}(r, \lambda) N(r) dr \tag{24}$$

where: $\sigma_{e,s,a}(r, \lambda)$ is the extinction, scattering, and absorption cross-section of aerosol particles.

The single scattering albedo is also defined:

$$\omega(\lambda) = \frac{k_s}{k_a + k_s} = \frac{k_s}{k_e} \tag{25}$$

**Total optical depth:**

The optical depth of the entire atmosphere column:

$$\tau_\lambda = \int_0^{z_{top}} k_{e,\lambda}(z) dz \tag{26}$$

Under clear-sky atmospheric conditions, $\tau$ is due to attenuation by aerosols, Rayleigh scattering, and absorption by gas molecules

$$\tau_\lambda = \tau^M_{a,\lambda} + \tau^M_{s,\lambda} + \tau^A_{a,\lambda} + \tau^A_{s,\lambda} \tag{27}$$

Where: - $\tau^M_{a,\lambda}, \tau^M_{s,\lambda}$ are optical depth due to absorption by gases and molecular scattering (Rayleigh scattering), respectively.

- $\tau_{a,\lambda}^{A}, \tau_{s,\lambda}^{MA}$ are optical depth due to absorption and scattering by aerosol particles, respectively.

### 4.3. Radiative Transfer Equation in the Atmosphere

The Radiative Transfer Equation is a mathematical model that describes the change in light intensity as it passes through a medium characterized by its absorption, scattering, and emission properties.

Assumptions of the plane-parallel atmosphere model:

- The atmosphere from the surface to the top of the atmosphere is divided into multiple horizontally stratified layers (parallel planes).
- The composition within each atmospheric layer, boundaries by two successive planes, is assumed to be homogeneous. The optical thickness is measured from the top of the atmosphere along the z-axis.
- The solar zenith angle, azimuth angle, and scattering angle in a specific direction are represented as shown in Figure 18.

The desired radiation at wavelength λ along an arbitrary path with a given azimuth angle and cosine of the solar zenith angle is determined by solving the radiative transfer equation [56]:

$$\mu \frac{d}{d\tau} I_{\lambda}(\tau, \mu, \phi) = I_{\lambda}(\tau, \mu, \phi) - J(\tau, \mu, \phi) \tag{28}$$

Here $\tau$ is the vertical optical depth, $\mu$ is then the cosine of the path zenith angle, and $\Phi$ is the azimuth angle relative to the sun's azimuth.

The general source function, $J(\tau, \mu, \phi)$ , which includes the scattering of solar radiation and thermal emission, is given by:

$$J(\tau, \mu, \phi) = J_0(\tau, \mu, \phi) + J_{MS}(\tau, \mu, \phi) \tag{29}$$

Where:

$$J_0(\tau, \mu, \phi) = \frac{\omega_0(\tau)}{4\pi} I0.\, e^{\frac{-\tau}{\mu_0}} P(\Omega; -\Omega_0) + [1 - \omega_0(\tau)] B[\Theta(\tau)]$$

$$J_{MS}(\tau, \mu, \phi) = \frac{\omega_0(\tau)}{4\pi} \int_{\Omega} P(\Omega; \Omega') I(\tau, \Omega') d\Omega' \tag{30}$$

Here, $\omega_0(\tau)$is the single scattering albedo, P is the appropriate angular scattering or phase function, and B is the Planck function at temperature $\Theta(\tau)$. The extraterrestrial solar irradiance is given by F and the path and solar directions are given by a respectively.

Solving the Radiative Transfer Equation (RTE) means determining the value of the radiation intensity I(λ,μ,ϕ,τ) in a 2D coordinate system, given the optical properties of the atmosphere and two boundary conditions: the incident radiation intensity at the top of the atmosphere and the surface reflection at the bottom. [59]

At the top of the atmosphere: τ=0:

$$I(0,\mu,\phi) = I(\tau_*,\mu,\phi)e^{-\tau_*/\mu} + \int_0^{\tau_*} J(\tau,\mu,\phi)e^{-\tau/\mu}\frac{d\tau}{\mu} \tag{31}$$

And at the bottom of the atmosphere τ=τ∗ (see Figure 18).

the radiative transfer equation becomes:

$$I(\tau_*,-\mu,\phi) = I(0,-\mu,\phi)e^{-\tau_*/\mu} + \int_0^{\tau_*} J(\tau,-\mu,\phi)e^{-(\tau_*-\tau)/\mu}\frac{d\tau}{\mu} \tag{32}$$

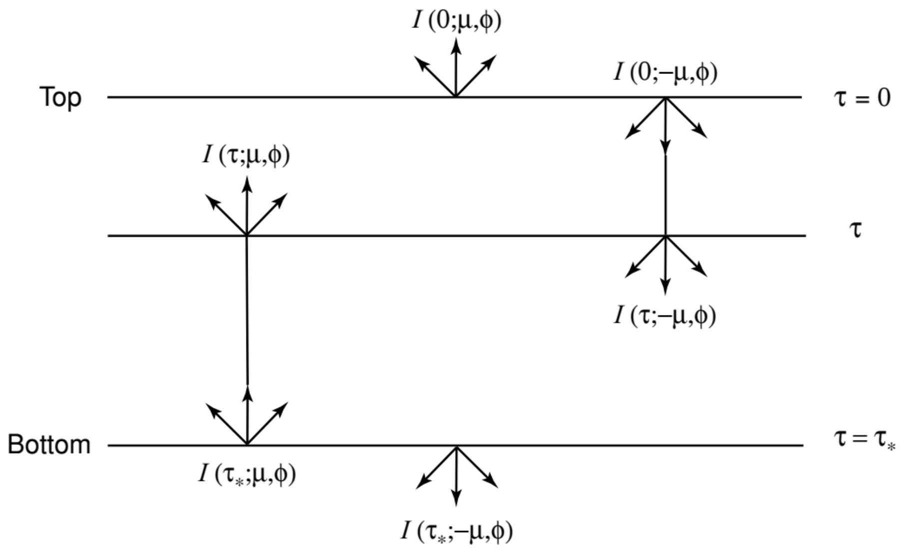


*Fig. 18. Upward and downward intensities at a given level $\tau$ and at top ($\tau = 0$) and bottom ($\tau = \tau^*$) levels in a finite*

The radiative transfer equation is expressed in the form of an integral-differential equation. To solve this equation, the following parameters must be known in advance:

- The structural composition of the atmosphere
- Attenuation due to absorption and scattering by gas molecules, aerosols, clouds, etc.
- Boundary conditions: radiation intensity at the top of the atmosphere and the surface reflectance of the Earth.

### 4.4. Atmospheric Transmittance Calculation Software

Many software tools have been developed to solve the integro-differential equation describing radiative transfer in the atmosphere, using various numerical algorithms. Among these, the MODerate resolution TRANsmittance (MODTRAN) code is one of the most widely used tools in the research and applied science communities.

MODTRAN is a moderate-resolution atmospheric radiative transfer model, widely applied for simulating radiation transmission through the Earth's atmosphere. It was developed by Spectral Sciences, Inc. and the U.S. Air Force Research Laboratory (AFRL), originally to support remote sensing missions and atmospheric research [60]. Key features include:

- Broad spectral range: MODTRAN simulates radiative transfer from the ultraviolet (UV) to the far-infrared (FIR), covering wavelengths from 0.2 μm to 10,000 μm.
- Detailed atmospheric modeling: Provides standard atmospheric profiles (e.g., polar, tropical, desert), as well as the ability to input user-defined atmospheric profiles.
- Scattering simulation: Supports various scattering models, including Rayleigh, Mie, and multiple scattering using the DISORT algorithm.
- Surface condition simulation: Includes surface reflectance models such as BRDF (Bidirectional Reflectance Distribution Function).

## 5. Factors affecting surface UV radiation and methods for UV radiation measurement

Although ultraviolet radiation constitutes only a very small portion of the total solar radiation, its short wavelength and high energy make it capable of causing harmful effects on ecosystems, material degradation, and human health. For humans, exposure to UV radiation from the Sun is associated with skin cancer, premature skin aging, cataracts, and other eye disorders. It can also impair the immune response and reduce the effectiveness of vaccines. Certain plant species respond to increased UV radiation by reducing growth or photosynthetic activity. Phytoplankton, the base of the marine food chain, can also be adversely affected [3],[4].

As it travels through the atmosphere, solar UV radiation undergoes complex processes of absorption and scattering before reaching the Earth's surface. Ozone strongly absorbs UV radiation, and the presence of ozone and oxygen in the stratosphere results in the absorption of nearly all solar radiation below 290 nm. Consequently, nearly all UV-C radiation (200–280 nm) does not reach the troposphere or the Earth's surface. Solar UV-B radiation (280–315 nm) is significantly absorbed by atmospheric ozone, while only a small portion (less than 3%) of UV-A radiation (315–400 nm) is absorbed [61], [62]. The inverse relationship between ozone and surface UV levels is often partially masked by variability in cloud cover, tropospheric pollution, or aerosol content in the atmosphere. This complicates the assessment of UV trends and underscores the need for direct measurements, especially since modeling surface UV radiation under cloudy conditions remains limited in accuracy.

To better understand and quantify surface UV radiation and its spatial and temporal variability, this chapter presents several methods for determining surface UV radiation, provides examples of published measurement results, and discusses the main factors influencing UV radiation.

### 5.1. Factors Affecting Surface UV Radiation

Surface UV radiation is defined as the downward irradiance incident on a horizontal surface. This incoming radiation consists of two components: the direct component that comes straight from the Sun and the diffuse component that is scattered by the atmosphere. Ultraviolet radiation from the Sun reaching the Earth's surface is influenced by various factors, including absorption, scattering, and reflection processes occurring in the atmosphere and at the Earth's surface. Below are the most important factors that affect the level of solar UV radiation reaching the ground.

**Solar Zenith Angle (SZA):** The solar zenith angle is the angle between the vertical direction at a specific point on Earth and the direction to the Sun. The SZA depends on latitude, day of the year, and time of day. Changes in the solar zenith angle affect the solar elevation and the length of the atmospheric path that radiation travels. The dependence of UV radiation on SZA explains the typical diurnal pattern of UV radiation under cloud-free conditions-it usually peaks around solar noon and decreases in the morning and afternoon. When the SZA is small (i.e., the Sun is high in the sky), the radiation passes through a shorter atmospheric path, experiencing less absorption, which results in higher surface UV intensity. Conversely, at large SZA (Sun is lower), the radiation must travel through a thicker layer of atmosphere, increasing absorption and reducing UV intensity at the surface. In high-latitude regions, the SZA is generally larger throughout the year, leading to lower UV radiation levels compared to equatorial regions [63], [64]. Figure 19 presents the relationship between time of day and UV radiation measured at the Kaunas monitoring station (Lithuania), located at 54.88°N, 23.83°E, 77 m., on February 28, 2025 [65].

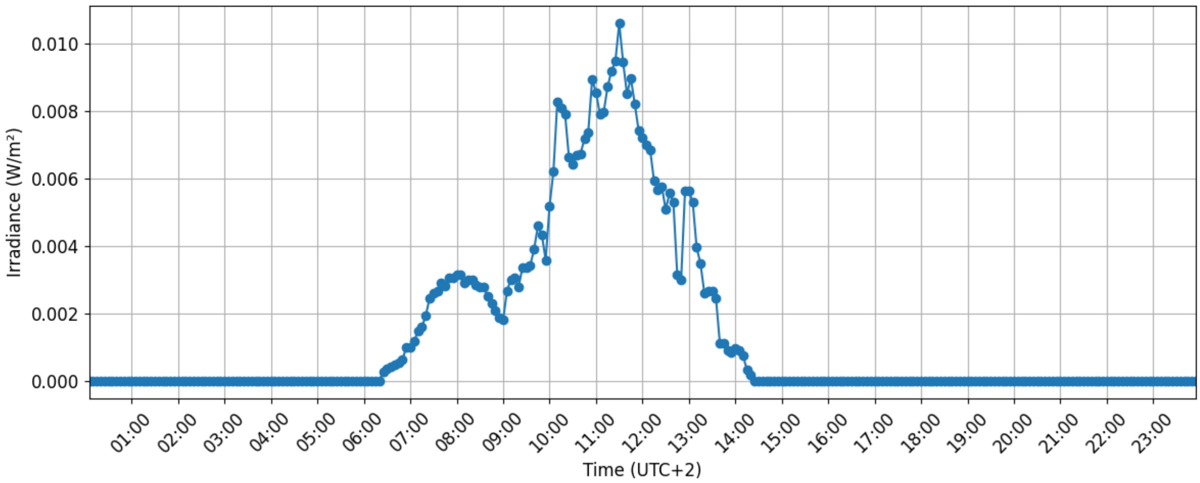


*Fig. 19. Diurnal Variation of UV-B Radiation*

The UV-B radiation data measured at the Kaunas monitoring station on February 28, 2025, show the diurnal variation of UV radiation. The intensity reaches its maximum at noon, corresponding to the smallest solar zenith angle, and decreases in the morning and afternoon as the solar zenith angle increases.

**Distance Between the Earth and the Sun**: The intensity of solar radiation decreases with the inverse square of the distance between the Earth and the Sun. This variation is geometric in nature and therefore independent of wavelength, meaning that radiation at all wavelengths is equally affected. Because the Earth's orbit around the Sun is elliptical, with the Sun at one of the foci, small variations in distance throughout the year are clearly observed. The Earth is closest to the Sun in early January (perihelion) and farthest in early July (aphelion). The relative difference between the minimum and maximum intensity is about 7%. This variation in radiation has implications for the geographical distribution of UV radiation, with the maximum occurring during the winter in the Northern Hemisphere and correspondingly during the summer in the Southern Hemisphere, and vice versa [64]. Thus, based purely on geometric considerations, the intensity of radiation during summer in the Southern Hemisphere is higher than in the Northern Hemisphere. Figure 20 illustrates the Earth's orbit around the Sun over the course of a year [65].

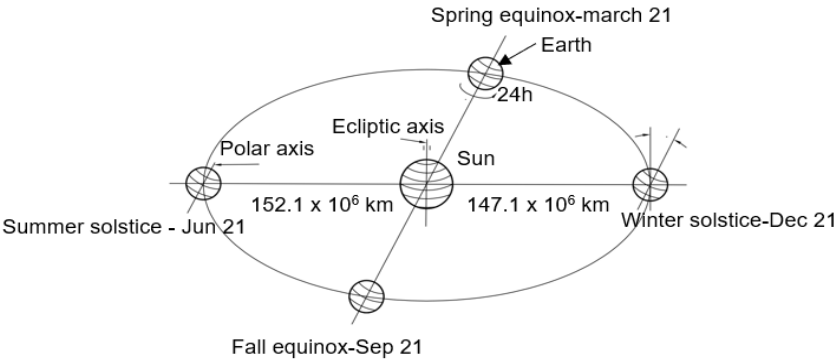


*Fig. 20. Annual motion of the earth about the sun [66]*

However, this factor can easily lead to confusion when comparing UV radiation at a single location. In addition to the Earth–Sun distance, other factors-such as the solar zenith angle and the season also significantly influence surface UV radiation. To illustrate this more clearly, an example is shown in Figure 21. It presents UV radiation measurements taken at 12:00 local time at the Uccle station (Belgium) on the perihelion date, January 2, 2024 (when the Earth is closest to the Sun), and the aphelion date, July 5, 2024 (when the Earth is farthest from the Sun).

The results show that the UV radiation measured on the aphelion date was higher than that on the perihelion date. (Measurement data were retrieved from the WOUDC database at the Uccle monitoring station of the Royal Meteorological Institute of Belgium) [67].

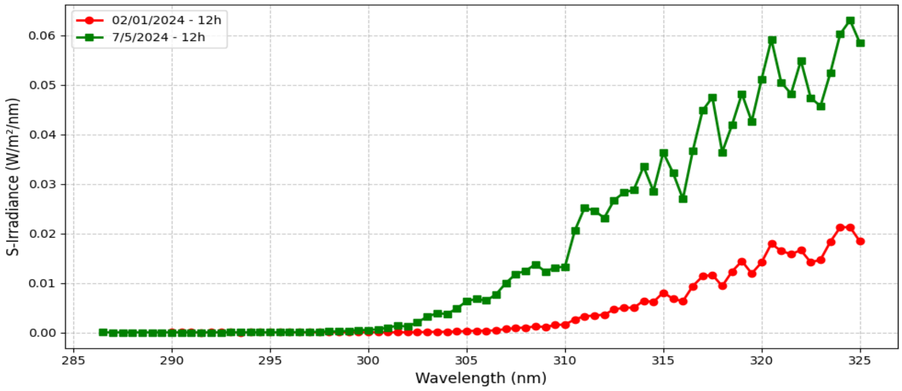


*Fig. 21. UV Irradiance Measured at Noon on Perihelion and Aphelion Dates at Uccle (Belgium)*

**Ozone Layer:** ozone in the atmosphere stratospheric absorbs nearly all UV-C radiation and a significant portion of UV-B radiation. However, the thickness of the ozone layer varies inversely with the amount of UV radiation received at the surface. Ozone concentration fluctuates over both space and time. The figure shows the global distribution of ozone as monitored by the Ozone-Measuring Instrument on the NOAA-21 Satellite.

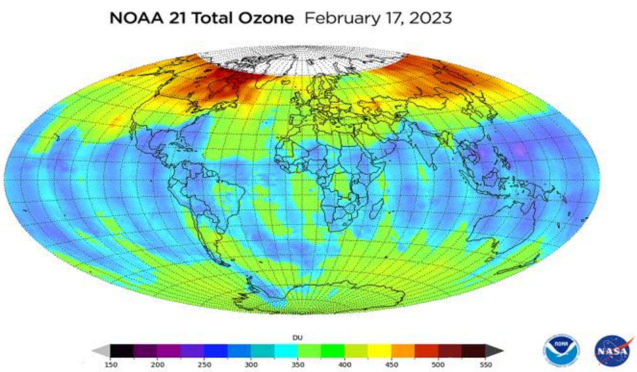


*Fig. 22. Total ozone measured by the Ozone Mapping and Profiler Suite – Nadir Mapper (OMPS NM) on February 17, 2023 [69]*

It can be observed that [61], [68]:

- Ozone is thicker in the polar regions and lower at the equator.
- It varies seasonally, with lower ozone levels in spring and higher levels in autumn.
- The "ozone hole" phenomenon over Antarctica in spring significantly increases UV-B radiation in that region.

The higher the ozone concentration, the more UV radiation is attenuated before reaching the Earth's surface. The PcModWin software allows users to modify ozone concentration in its simulations. A comparison of solar UV irradiance for different ozone concentrations is shown in Figure 23 (with ozone values of 250 DU (Dobson Unit), 350 DU, and 450 DU used for the simulations)

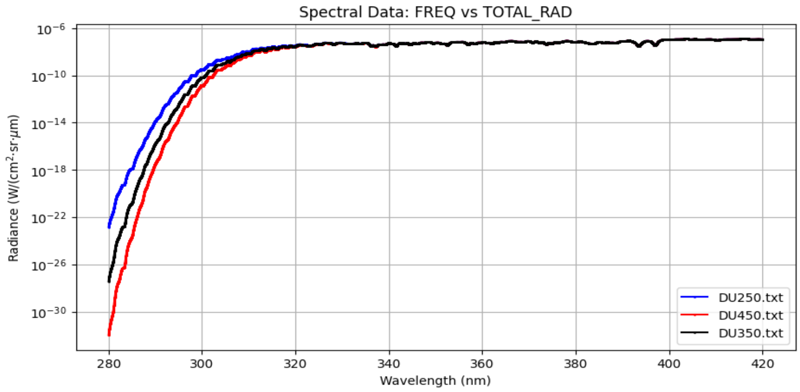


*Fig. 23. Effect of Ozone Concentration on Surface UV Radiation*

The calculation results show that surface UV radiation increases as ozone concentration decreases. The attenuation of UV radiation due to ozone layers occurs primarily in the UV-B region.

**Effect of Clouds on Surface UV Radiation**: Clouds are among the most significant factors affecting surface UV radiation. However, their impact is not limited to reducing UV radiation - under certain conditions, clouds can actually enhance UV intensity due to the cloud enhancement effect. Clouds influence UV radiation through three primary mechanisms [61], [69–71]:

- Absorption: Part of the UV radiation is absorbed by water droplets and ice crystals within the clouds.
- Scattering: Clouds scatter UV radiation in multiple directions, causing some of it to be lost before reaching the surface.
- Reflection: Cloud surfaces can reflect part of the UV radiation back into the atmosphere, reducing the amount reaching the surface.

Yet, in some specific conditions, clouds can increase surface UV radiation due to enhanced reflection between cloud layers or between clouds and the ground.

Several experimental studies have quantified UV attenuation based on cloud cover. Key findings include:

- Under completely overcast skies with thick clouds, UV radiation can be reduced by up to 70% compared to clear skies.
- Thin clouds or clouds with many gaps may only slightly reduce UV, typically by 10-30%.

Although clouds usually diminish UV radiation, in certain situations they can enhance surface UV intensity due to factors such as:

- Partial cloud cover that does not fully block direct sunlight.
- Cloud edges reflecting and scattering UV radiation, increasing local UV intensity under the cloud edges.
- This phenomenon is especially noticeable on days with scattered or convective clouds.

A study in the Netherlands showed that under scattered cloud conditions, UV intensity can increase by up to 30% in some cases (typically ranging from 10–30%) compared to clear-sky conditions [70].

Another study in Australia also reported that on partly cloudy days with gaps in the clouds, UV radiation could be over 20% higher than on cloud-free days [71].

Figure 24 shows UV radiation measured in Brazil on a day with scattered cumulus clouds (January 15, 2011).

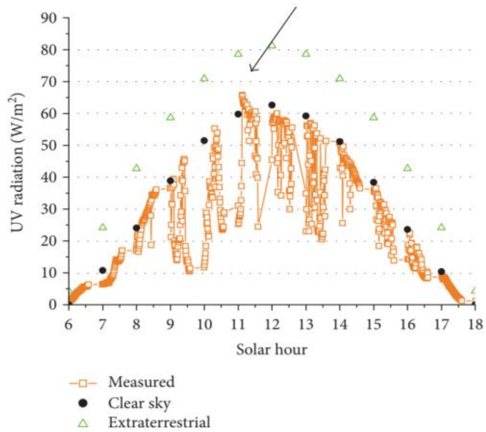


*Fig. 24. Enhancement of UV radiation by clound efect (on January 15,2011 in Brazil) [72]*

Not all types of clouds affect UV radiation in the same way. A simulation of how different cloud types of influence surface UV radiation were performed using the PcModWin software, as illustrated in Figure 25.

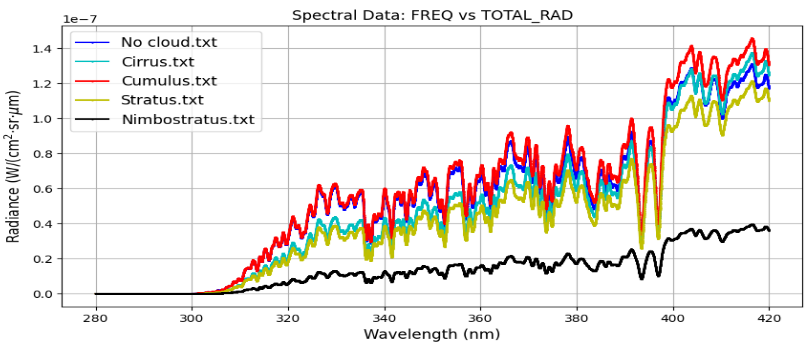


*Fig. 25. Effect of Clouds on UV Radiation*

Below are common cloud types and their typical influence on surface UV radiation [61], [68–71]:

Table 8. Influence of clouds on UV radiation

| Cloud Type | Impact on UV Radiation |
|---|---|
| Cirrus (thin, high clouds) | Slight reduction in UV (around 5–10%) due to their thinness and high altitude. |
| Cumulus (fluffy, scattered clouds) | Can amplify UV radiation due to reflection from cloud edges. |
| Stratus (thick, low-level clouds) | Significant reduction in UV, possibly up to 60–80%. |
| Nimbostratus (dense rain clouds) | Strong UV absorption, potentially reducing UV by up to 90%. |

**Reflection from the Earth's Surface (Albedo):** Albedo is the proportion of solar radiation that is reflected back into the atmosphere by the Earth's surface. There are many types of surfaces with varying albedo characteristics. Typical examples include:

- Sand (dry sand, white sand, brown sand, dune sand, black sand)
- Water (calm ocean, seawater, offshore seawater, coastal seawater)
- Snow and Ice (fresh dry snow, mountain snow, melting snow, solid ice, granular snow, fine fresh snow)
- Vegetation (Pinyon pine, fir, Norway spruce, Ponderosa pine, coniferous trees, deciduous trees, birch leaves, oak leaves, grazing grassland)
- Rocks (basalt, granite)
- Fields/Grasslands (dry grass, green ryegrass, lush green grass, perennial ryegrass, alpine meadow, fresh green meadow, long dry grass, lawn grass, crops like wheat fields and tall green corn)
- Artificial construction materials (concrete slabs, old runway concrete, aged asphalt, terracotta tiles, red construction bricks, plywood sheets, white vinyl panels, transparent fiberglass greenhouse roofs, corrugated galvanized metal sheets)

Spectral reflectance data across the full spectral range from approximately 300 nm to 800 nm is available only for the specific material types listed above [73].

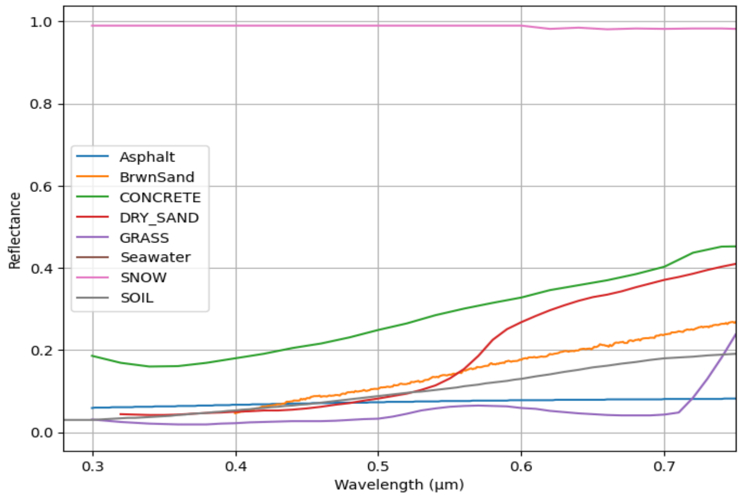


*Fig. 26. Spectral reflectance of some materials*

From the graph above, it can be observed that:

- Most natural materials have low reflectance coefficients in the UV region (< 0.1), but the reflectance increases gradually in the visible (VIS) and near-infrared (NIR) regions.
- Artificial materials tend to have higher average reflectance compared to natural materials.
- Concrete slabs exhibit the highest reflectance among common construction materials.
- Snow is an exception, with very high reflectance across the entire spectrum from UV to NIR.
- Snow and ice can have very high albedo values (up to ~95%), which significantly increases the UV intensity due to backscattering into the atmosphere.
- Sand and desert surfaces have moderate albedo (20–30%), which can also enhance UV radiation.
- Water bodies and forests have low albedo (less than 10%), which reduces reflected UV radiation.

This explains why UV intensity in snow-covered areas can be up to 50% higher than in snow-free regions [61], [64], [73].

### 5.2. Methods for Measuring UV Radiation

Methods for determining UV radiation include:

- Ground-based instruments: Devices installed at monitoring stations directly measure the UV radiation reaching the Earth's surface.

- Satellites: Spectrometers mounted on satellites measure UV radiation reflected from the Earth's surface. These observations, combined with radiative transfer (RT) models, are used to estimate surface UV radiation on a global scale.
- Radiative Transfer Models: These models calculate surface UV radiation based on atmospheric models, geographical parameters, and optical properties (scattering, absorption) of atmospheric components used as input data.

In addition to the above, statistical models are used. These models are built from long-term monitoring data and analyze the dependence of surface UV irradiance on geographic and atmospheric factors in the past to predict current and future conditions.

This chapter primarily focuses on ground-based UV radiation measurement devices and satellite-based UV observations.

### 5.2.1. Ground-based instruments

Currently, there are three main types of ground-based instruments commonly used by surface UV radiation monitoring stations around the world, including [4],[61], [63], [72–74]:

- SpectroRadiometer
- Multifilter narrowband radiometers
- Broadband filter radiometers

#### 5.2.1.1. SpectroRadiometer

Spectroradiometers are high-resolution instruments used to measure UV radiation, allowing for the determination of spectral irradiance at specific wavelengths. According to the guidelines of the Global Atmosphere Watch (GAW) program by the World Meteorological Organization (WMO), UV spectroradiometers must cover at least the 290–325 nm range, and ideally the full solar UV range from 290–400 nm. The spectral bandwidth (full width at half maximum – FWHM) should be less than 1 nm [75].

Below is an overview of two types of instruments commonly used in global UV monitoring networks:

**Brewer Spectrophotometer:** Among the UV spectroradiometers used globally, the Brewer spectrophotometer is the most widespread, accounting for over 75% of all actively operating instruments. It was developed in Canada in the early 1980s, initially to support ozone measurements within the WMO’s Global Atmosphere Watch (GAW) program. Today, a global network of Brewer instruments span’s locations from deserts to

Antarctica, providing data to the World Ozone and Ultraviolet Radiation Data Centre (WOUDC). The EUBREWNET network includes more than 100 Brewer instruments across 60 monitoring stations worldwide, aiming to provide consistent measurements of ozone, $SO_2$, UV radiation, and Aerosol Optical Depth (AOD). Among its various models, the Brewer Mark III is the most advanced. It uses a double-monochromator optical system to minimize stray light, a significant improvement over previous model. Additionally, it features a UV-enhanced photomultiplier tube, improving measurement performance [76]. The Brewer Mark III spectrophotometer operates within the wavelength range of 286.5 nm to 363 nm, with a spectral resolution of 0.6 nm, and thermal stability of 0.01 nm over an operational temperature range from –20 °C to +50 °C. This instrument offers researchers powerful capabilities to better understand solar UV radiation and its biological and environmental impacts, both now and in the future. It also serves as a reference-grade instrument for calibrating lower-performance broadband UV sensors [77–78].

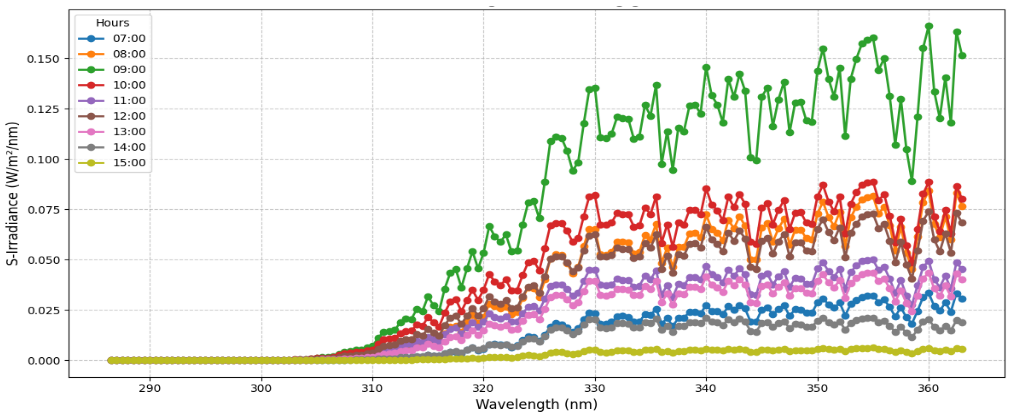


*Fig. 27. UV Radiation Spectrum Measured by the Brewer Mark III Spectrophotometer on December 21, 2023*

Figure 27 shows the spectrum of UV radiation (280–363 nm) measured at the Earth's surface at an altitude of 1590 m, recorded at the Davos monitoring station in Switzerland (Coordinates: 46.81°N, 9.84°E, 1590 m, UTC+1). Only a portion of the solar UV-B and UV-A radiation reaches the Earth's surface.

**SUV-100 Spectroradiometer:** The SUV-100 spectroradiometer [79] employs a Czerny-Turner optical system with a double monochromator and a diffraction grating operating at 240 nm, featuring 2400 grooves/mm. The instrument has a nominal bandwidth of 1 nm, while in the visible range, the bandwidth varies between 0.8 and 1 nm. The SUV-100 scans the spectrum from 280 nm to 605 nm in 0.2 nm steps, with a total scan time of approximately 16 minutes. The device uses a photomultiplier tube

(PMT) as the signal detector, housed in a temperature-stabilized system to maintain accuracy. A Teflon diffuser acts as the radiation collector. The system also includes built-in automatic calibration lamps, which monitor and correct for wavelength and intensity stability. Measurement data are acquired and processed directly by a computer. Each station in the ultraviolet radiation monitoring network of the U.S. National Science Foundation (NSF) is equipped with either an SUV-100 or an SUV-150B spectroradiometer manufactured by Biospherical Instruments. These spectroradiometers are designed for fixed installation and continuous operation under harsh environmental conditions. The system operates fully automatically, requiring operator intervention only for periodic manual calibrations and operational checks.

**Array-Type Spectroradiometers:** Array-type spectroradiometers measure UV radiation based on a different principle compared to traditional scanning spectroradiometers. Instead of rotating a diffraction grating to scan each wavelength step-by-step through an exit slit before reaching a photomultiplier detector, these devices project the UV spectrum directly onto a multi-element sensor, such as a diode array [80]. As a result, the entire spectral range of interest can be measured almost simultaneously. Advantages of array spectroradiometers include fast measurement speed, compact design, high portability, and improved stability and reliability due to the absence of moving parts. However, the main drawback of array spectroradiometers is their low sensitivity, with the capability to measure only wavelengths above 300 nm, and difficulties in correcting stray light. Despite certain limitations, the outstanding advantages in measurement speed and stability make array-type spectroradiometers a promising choice for many applications in UV radiation research.

#### 5.2.1.2. Multi-Filter Narrowband Radiometers:

Multi-filter narrowband radiometers use several filters (typically between 4 and 7) to sample UV radiation at specific wavelengths, with a spectral resolution of approximately 1–10 nm (full width at half maximum – FWHM) [81]. These instruments can be used to reconstruct the global solar irradiance spectrum, calculate important quantities such as erythema-weighted irradiance, or determine the total column ozone

#### 5.2.1.3. Broadband Filter Radiometers

Broadband filter radiometers are instruments that use filters to transmit radiation over a wide wavelength range. They have been deployed at numerous sites for decades, providing continuous records of daily UV radiation data.

Advantages of broadband filter radiometers [82] include:

- Lower cost compared to spectroradiometers.
- Ease of use and deployment under various environmental conditions.

Disadvantages of broadband filter radiometers include difficulty in calibration, the ability to measure only a composite parameter, and the inability to distinguish between different factors affecting UV radiation levels, such as ozone, clouds, or aerosols.

Despite these limitations, broadband filter radiometers remain an important tool for UV radiation monitoring, especially in long-term studies and practical applications requiring simple and user-friendly instruments.

### 5.2.2. Satellite instruments

TOMS (Total Ozone Mapping Spectrometer) operated from 1978 to 2005 and was installed on several satellites launched by NASA and international partners. It collected continuous global UV data at six wavelengths: 312.5, 317.5, 331.2, 340, 360, and 380 nm [83–84]. The main functions of TOMS included:

- Measuring total column ozone
- Monitoring the ozone hole
- Observing volcanic dust, aerosols, and smoke from wildfires
- Measuring surface UV radiation

The output of the TOMS algorithm was the Total Column Ozone (in Dobson Units, DU) for each ground pixel, from which surface UV index and the global temporal distribution of ozone could be derived.

Global Ozone Monitoring Experiment (GOME) is a remote sensing instrument designed to measure ozone and other atmospheric constituents from space. It was mounted on the European Remote Sensing Satellite 2 (ERS-2) of the European Space Agency [85]. GOME operates across the UV–VIS–NIR spectral range (240–790 nm), measuring backscattered radiation from Earth's surface into space. GOME products include Total Column Ozone, Ozone Profile by altitude, and various atmospheric gases.

Ozone Monitoring Instrument (OMI), a Dutch Finnish instrument aboard NASA's Aura satellite, was launched in July 2004 and continues long-term UV monitoring using an algorithm similar to TOMS.

Figure 28 shows the global distribution of the UV index under clear-sky conditions at local solar noon on June 3, 2005. The data in the figure is based on the OMUVB grid with a resolution of 1×1 degree.

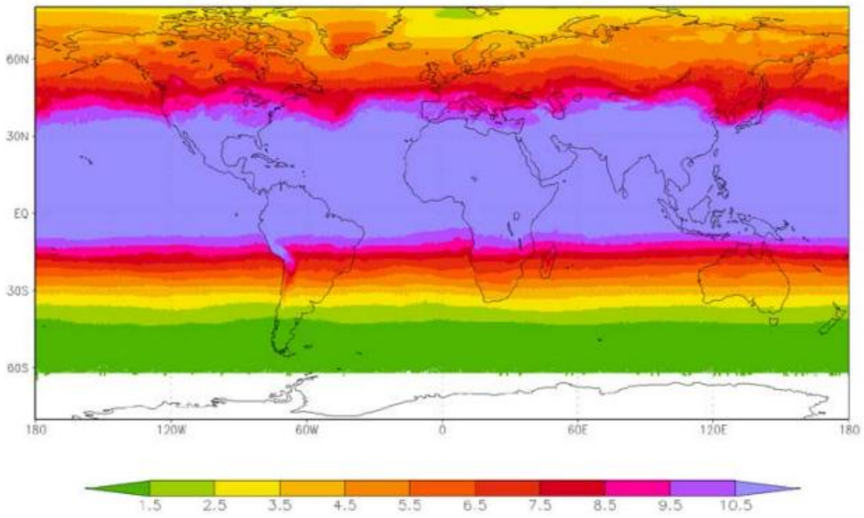


*Fig. 28. Global distribution of the UV index under clear-sky conditions at local solar noon on June 3, 2005, derived from OMI measurement data [86]*

**5.3. Measurement of UV Radiation at the Earth's Surface**

At present, numerous ground-based stations around the world operate either independently or as part of networks to monitor surface UV radiation. Whether functioning individually or within a network, the research objectives of ground-based UV monitoring instruments include:

- Establishing a UV climatology database through long-term monitoring, for example, within a network of UV spectroradiometers.
- Detecting trends-particularly spectral trends-in global UV radiation intensity.
- Providing datasets for studying specific processes and for validating radiative transfer models as well as satellite-derived surface UV radiation data.
- Gaining a better understanding of regional differences in global UV spectral radiation intensity.
- Collecting information on actual UV levels and their variations with daily and seasonal cycles.
- Enabling the determination of the UV index.

- Supplementing UV spectral measurements.
- Supporting quality control of UV spectral measurements.

Table 9. Summarizes several global UV radiations monitoring networks

| **Network** | **Coverage** | **Main Function** | **Sources** |
|---|---|---|---|
| WOUDC | Global | UV monitoring, ozone layer, air quality | [87] |
| ELDONET | Europe | Monitoring UV-B, UV-A, and visible light; supporting ozone layer change detection; satellite data validation and calibration | [88] |
| USDA UV-B Monitoring and Research Program | USA (30 trạm) | Monitoring surface UV-B radiation and studying its effects on biological systems and agriculture | [89] |
| AEMET – Agencia Estatal de Meteorología | Spain | UV Index (UVI), Irradiance UV-A/B, Total Ozone Column | [90] |
| Chinese Ecosystem Research Network | China | Hourly UV data are aggregated into daily values. | [91] |

Several measurement stations, such as those in Łódź, Poland [92], Recife, Brazil [72], Baghdad, Iraq [93], and Northeast China [94], monitor long-term changes in UV radiation and contribute to the development of surface UV radiation forecasting models.

Table 10 presents the daily maximum UV radiation values recorded at various stations around the world, corresponding to the geographic coordinates of each site, along with the global UV index values. The data are sourced from the WOUDC database, stations within the Eldonet network [88], and several independently reported stations.

Table 10. The daily maximum UV radiation values

| **Location** | **Latidude** | **Longtitude** | **Peak value Irradiance (W/m²)** | **Ref.** |
|---|---|---|---|---|
| Recife, Brazil. 2011 | -8.05⁰ | -34.8⁰ | 70.4 | [72] |
| Łódź, Poland (1997-2001) | 51.7⁰ | 19.50⁰ | 47 | [92] |
| Baghdad, Iraq (2015) | 33.30⁰ | 44.44⁰ | 51.75 | [93] |
| Northeast China (2005-2011) | 52.00⁰ | 134.00⁰ | 50 | [94] |
| Abisko (1997-2005) | 68.83⁰ | 19.00⁰ | 34.76 | [88] |
| Lund (1997-2000) | 55.12⁰ | 13.07⁰ | 60.47 | |
| Helgoland (1997-2000) | 54.17⁰ | 7.85⁰ | 44.85 | |
| Erlangen | 49.58⁰ | 11.02⁰ | 54.03 | |
| Karlsruhe | 49.05⁰ | 8.38⁰ | 50.62 | |
| Ljubljana | 46.07⁰ | 14.55⁰ | 61.49 | |
| Bonassola | 44.17⁰ | 09.50⁰ | 62.83 | |
| Pisa | 43.72⁰ | 10.38⁰ | 56.51 | |
| Logrono | 42.47⁰ | -2.45⁰ | 59.01 | |
| Lisbon | 38.70⁰ | -9.17⁰ | 63.68 | |
| Athens | 37.07⁰ | 23.77⁰ | 57.58 | |
| Sierra Nevada | 37.07⁰ | -3.33⁰ | 63.4 | |
| Malaga | 36.72⁰ | -4.38⁰ | 63.78 | |
| Gran Canaria | 27.92⁰ | -15.58⁰ | 66.31 | |
| Joinville | -26.25⁰ | -48.92⁰ | 56.72 | |
| Playa Union | -43.25⁰ | -65.00⁰ | 64.2 | |
| Lauder | -45.02⁰ | 169.68⁰ | 63.01 | |

| | | | | |
|---|---|---|---|---|
| *Zacatecas (2005)* | $22.77^0$ | $-102.57^0$ | 52.8 | [95] |
| ARG-342 (2013) | –45.78° | -67.50° | 0.32 * | [96] |
| AUT-167(2013) | 48.23° | 16.42° | 0.2 * | [97] |
| KOR-516 | 36.54° | 126.33° | 0.25* | [98] |
| LTU-Kaunas 312 | 54.53° | 23.50° | 0.25* | [99] |
| LUX-Die Kirch 412 | 49.87° | 6.17° | 0.19* | [100] |
| MDA-Chisinau 455 | 47.00° | 28.82° | 0.37* | [101] |
| MDG- Antananarivo 531 | -18.91° | 47.53° | 0.2* | [102] |
| SYC- Mahe 207 | 4.67° | 55.17° | 0.25* | [103] |

( $^{(*)}$ – values in UV-B)

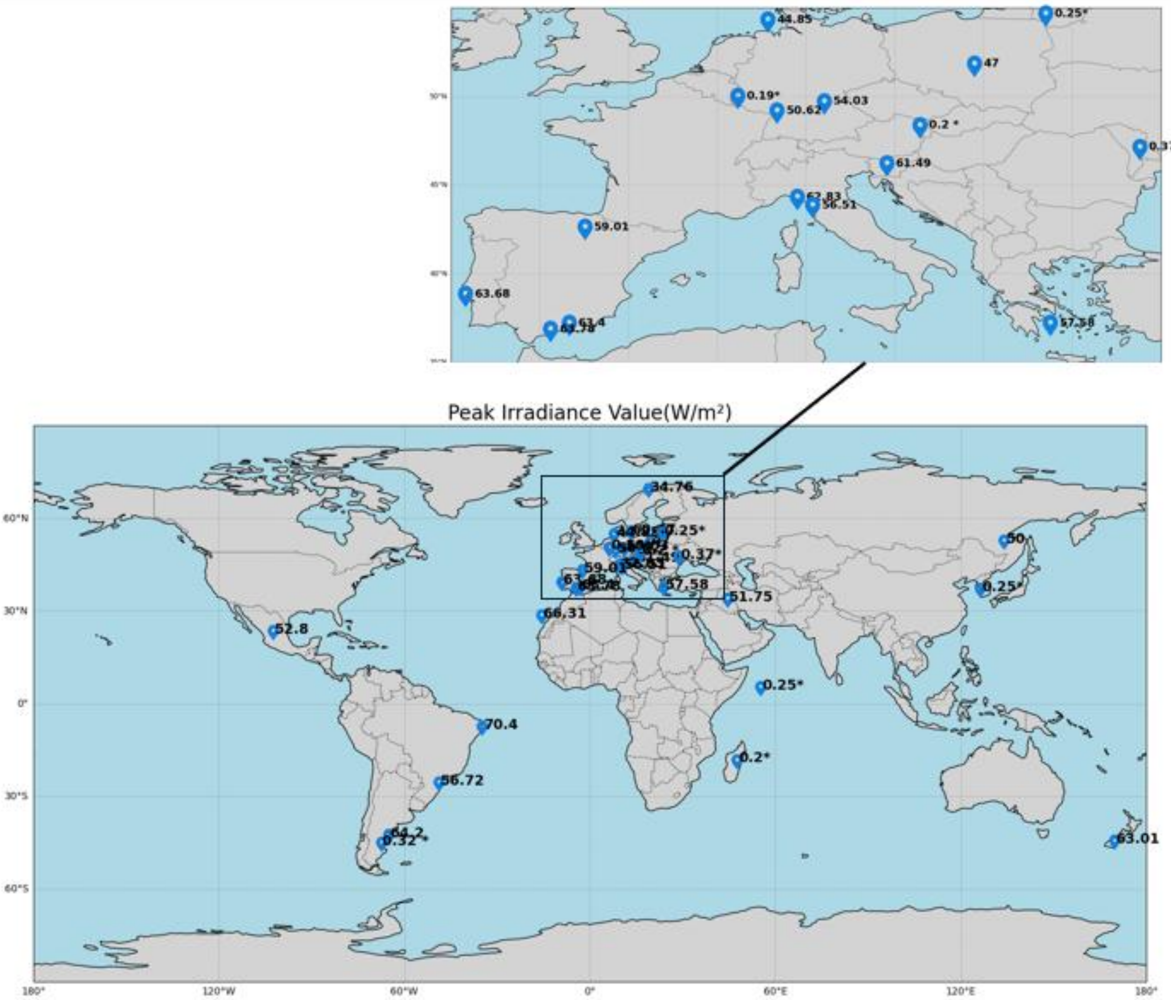


*Fig. 29. Distribution of UV radiation at selected locations on the Earth's surface*

Solar UV radiation on the Earth's surface is influenced by many factors. In addition to systematic factors such as geometric parameters, variations in ozone concentration, aerosols, etc., are more difficult to control and accurately predict.

- Spatial factors and geographic location significantly affect surface UV radiation. To achieve accurate large-scale forecasting, it is necessary to deploy multiple ground-based stations in combination with satellite data calibration to produce a comprehensive map of surface UV radiation distribution.
- Published data on surface UV radiation indicate that there is no evidence for the presence of UV radiation in the 250–295 nm range at the Earth's surface.

To investigate whether UV-C radiation (250–295 nm) reaches the Earth's surface and to evaluate its potential applicability in military technologies, this dissertation focuses on the development of a highly sensitive ground-based UV background radiation measurement system. It also includes measurements of UV radiation in the 250–295 nm range at the Earth's surface. Based on the data collected, the study aims to assess the detectability of UV-C radiation and determine whether solar UV-C is completely absorbed by ozone and other atmospheric components.

The next chapter will present the detailed process of building the high-sensitivity UV measurement device, the measurement procedures, and the conclusions drawn in response to the research question.

## 6. Photon counting detector used in measurement of UV (250-295nm) background

### 6.1. Station for Measuring UV Background Radiation in the 250–295 nm Range

The conceptual design of the background radiation measurement station in the UV-C spectral range is illustrated in figure 30. It consists of three fundamental functional blocks, as detailed below:

- Optical system: Focuses background radiation into the entrance slit of the monochromator.
- Monochromator: Disperses the radiation into specific monochromatic wavelengths.
- Detection and signal processing system: Determines the photon count of the background radiation corresponding to the specific wavelengths selected by the monochromator. This system employs a highly sensitive photomultiplier tube as the detector, operating within the UV-C spectral region.
- Computer with software: Controls the radiation measurement process.

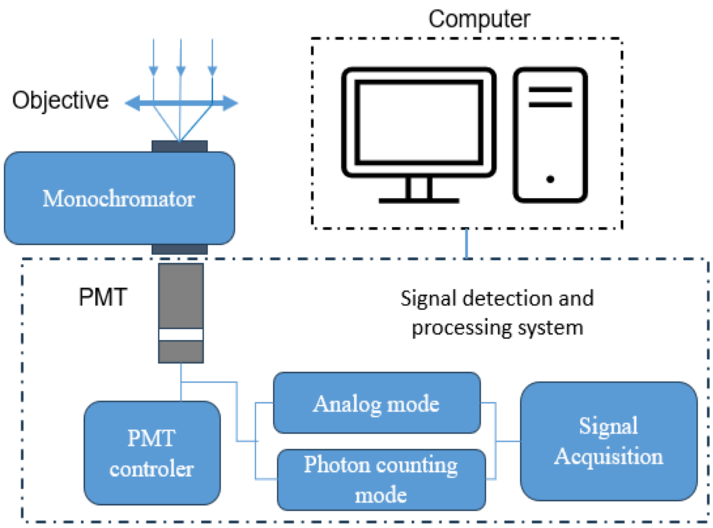


*Fig. 30. Conceptual Diagram of the Radiation Measurement Station*

Additionally, calibration of the measurement station requires an ultraviolet radiation source with a well-characterized spectral profile.

#### 6.1.1. Monochromator

A monochromator is a spectroscopic instrument used to isolate a specific range of monochromatic wavelengths from a broader spectral source. It is an optomechanical device that employs either a diffraction grating or a prism (referred to as the dispersive element) to disperse the incoming beam into a monochromatic output beam.

To obtain a specific monochromatic wavelength at the output, the dispersive element must be rotated (scanned) by an appropriate angle corresponding to the desired wavelength. The monochromator consists of key components such as entrance slits, lenses, mirrors, windows, and either a diffraction grating or a prism. The materials used to fabricate these components depend on the designed operational wavelength.

Monochromators designed for the UV, visible, and infrared spectral regions share a fundamentally similar structure, differing primarily in the materials used to accommodate each spectral range. There are two commonly used types of monochromators:

- Diffraction grating monochromators
- Prism monochromators

#### 6.1.1.1. Diffraction Grating Monochromator

For the construction of the measurement station, the Omni-λ300 monochromator (based on the Czerny-Turner configuration) available in the laboratory was selected. Figure 31 illustrates the optical schematic of a diffraction grating-based monochromator, which consists of the following components:

1. Entrance slit: Provides a rectangular optical image.
2. Collimating mirror M1 (or lens): Produces a collimated radiation beam directed onto the grating.
3. Diffraction grating (dispersive element): In principle, this can be either a transmission or reflection grating. However, most commercial monochromators utilize a reflection grating, which allows for a more compact and efficient optical design.
4. Focusing mirror M2: Reconstructs the entrance slit image and focuses it onto the focal plane.
5. Exit slit: Positioned at the focal plane to isolate the desired spectral band.

Moreover, most spectrometers are equipped with input and output windows, which are designed to protect internal components from dust and harmful laboratory fumes.

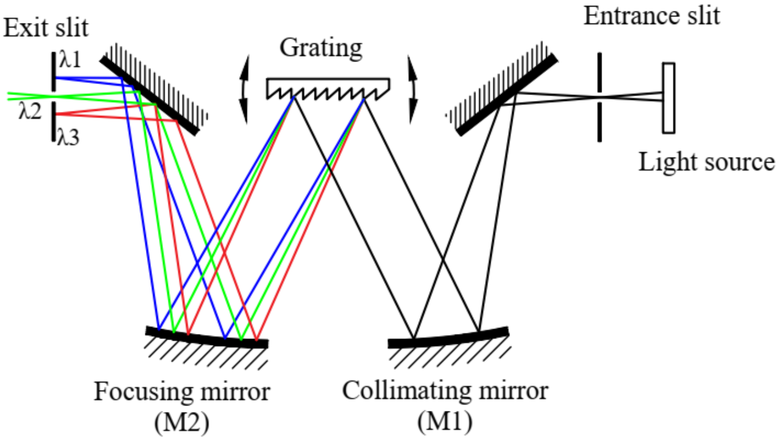


*Fig. 31. Schematic drawing of a monochromator setup [104].*

In the illustration, for simplicity, the incident beam is depicted as consisting of only three wavelengths. This radiation enters the monochromator through a narrow rectangular slit and is collimated by the collimating mirror M1, directing it onto the grating surface at an incidence angle. Angular dispersion of the wavelengths occurs at the reflective surface as a result of diffraction. The dispersed beam is then focused onto the focal plane by focusing mirror M2, where a rectangular image of the entrance slit is formed for the three wavelengths. The exit slit blocks wavelengths $\lambda_1$ and $\lambda_3$, allowing only $\lambda_2$ to pass through. By rotating the grating, the desired wavelength range can be focused onto the exit slit.

**Diffraction Phenomenon at the Grating**

The dispersion of a broadband light beam at the grating surface is based on the diffraction phenomenon. The relationship between the incidence angle and the diffraction angle is expressed by Equation:

$$\sin\theta_m + \sin\theta_i = \frac{m\lambda}{g} \tag{33}$$

Where:

- $\theta_i$ is the incidence angle of the incoming beam,
- $\theta_m$ is the diffraction angle for order m,
- $\lambda$ is the wavelength of the incident light in vacuum,
- g is the grating constant, representing the spacing between adjacent grooves.

The primary advantage of the monochromator in this configuration lies in its simple structure and the fact that its spectral resolution is independent of the radiation wavelength being dispersed. The wavelength selection scanning mechanism is integrated into the system and can be controlled via external software.

The technical specifications of the monochromator are presented in Table 11.

Table 11. Specifications of the Omni-λ300 Monochromator

| | |
|---|---|
| Focal Length | 300 mm |
| Numerical Aperture | F/3.9 |
| Wavelength Range | 185nm - far infrared (with different gratings) |
| Resolution | 0.1nm (1200 l/mm grating @435.8nm) |
| Dispersion | 2.7 nm/mm (1200 l/mm grating) |
| Wavelength Accuracy | 0.2 nm (1200 l/mm grating) |
| Wavelength Repeatability | 0.1 nm |
| Step Size | 0.005 nm |
| Focal Plane | 25mm x 14mm (W x H) |
| Slit | Width:10μm-3mm (micrometer driven) |
| | Height: 14 mm |

The manufacturer has pre-installed several communication protocols and command formats to control the monochromator, through the UART serial communication port. Using some existing programming software such as (C++, Python, MATLAB ...) can write control programs.

To ensure that the monochromator works properly, the parameters need to be set in accordance with the manufacturer's requirements. Some of the parameters that need to be taken care of are Settings of the number of turrets currently used, the zero position of the grating, the correction factor, the initial position of the grating and the Blaze Wavelength.

- Adjust the width of the Slit to ensure the desired output wavelength resolution is obtained.

- Set the turret’s rotation speed to match the engine response time.

- Control monochromator to separate monochromatic waves in the desired spectral region from 200 nm to 300 nm with a resolution of 1 nm.

A major drawback of diffraction grating monochromators is the occurrence of higher-order diffraction. This issue arises because the interference condition described by Equation (34) is satisfied not only with the first-order diffracted wavelength but also for its integer multiples at higher diffraction orders. As a result, multiple wavelengths can appear at the monochromator's output simultaneously.

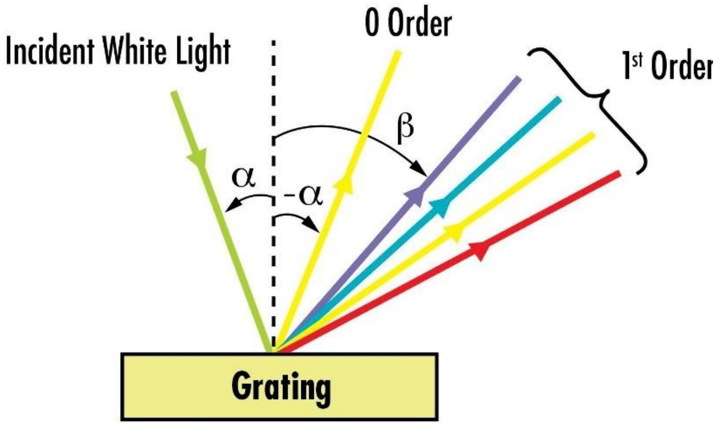


*Fig. 32. Higher-order diffraction [105]*

Although the intensity of higher-order diffraction is lower, its presence can lead to erroneous radiation intensity measurements at the monochromator's output.

In most applications, this issue is mitigated by using optical filters at the monochromator's input, which narrows the spectral range of the source, effectively eliminating unwanted higher-order diffraction components. However, in the case of background radiation analysis in the ultraviolet region from the Sun, using filters may also result in the removal of the weak background radiation that needs to be measured.

#### 6.1.1.2. Prism Monochromator

The basic operating principle of a prism monochromator is similar to that of a diffraction grating monochromator, with the key difference being that the dispersing element is a prism instead of a diffraction grating.

The separation of light in a prism results from the variation in refractive index for different wavelengths. The propagation of light through a prism is illustrated in Figure 33. The angle of refraction at which radiation of a given wavelength exits the prism is determined by Equation (34).

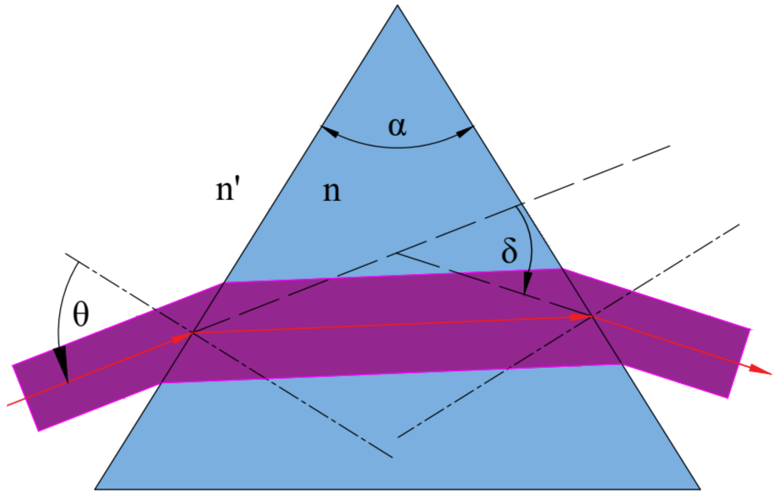


*Fig. 33. Deviation of the Monochromatic Beam by a Dispersive Prism*

$$\delta = \arcsin\left(\sin\alpha\sqrt{\left(\frac{n'}{n}\right)^2 - \sin^2\theta} - \sin\theta\cos\alpha\right) - \theta + \alpha \tag{34}$$

Where:

- δ is the deviation angle between the incident ray and the refracted ray.

- $\alpha$ is the prism angle

- θ is angle of incidence

- n’ is the refractive index of the medium in which the prism is embedded (n’ ≈ 1 for air).

- n is the refractive index of the prism material,

In this study, the Mirror Monochromator SPM-2 was selected. Figure 34 illustrates the optical diagram of the Carl Zeiss SPM-2 monochromator [106].

Broadband radiation from the source enters through the input slit (2) and is reflected by the reflecting prism (6) towards the off-axis parabolic mirror (2). This mirror focuses on the beam and directs it to the prism (3), which then directs the beam to the plane mirror (4).

After reflection, the beam is refocused by mirror (5) and sent back through the prism (3). The refractive dispersion within the prism causes different spectral components of the radiation to be refracted at different angles. The dispersed radiation is then collected and focused by mirror (1). Finally, after being reflected once more from the prism (6), the beam exits through the output slit.

The output wavelength is selected by rotating prism (3) to a specific angle.

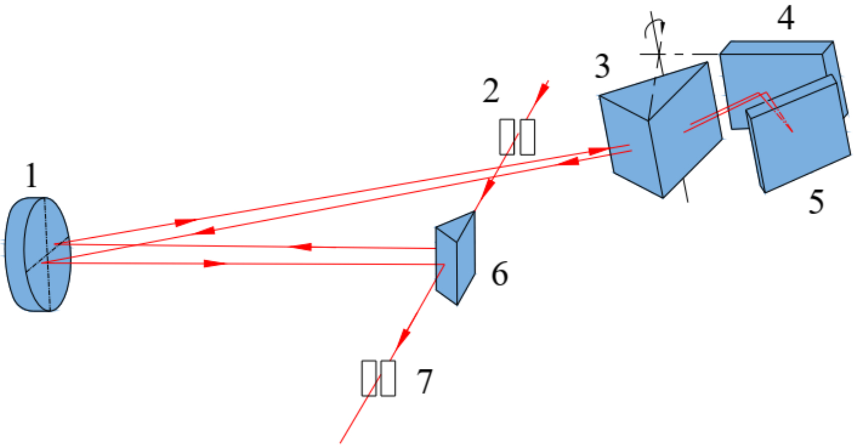


*Fig. 34. Optical Diagram of the SPM-2 Monochromator*

*1, off-axis, tilted parabolic mirror; 2, entrance slit; 3, dispersing prism; 4, plane mirror; 5, autocollimation mirror; 6, reflecting prism; 7, exit slit.*

Some key parameters of the monochromator include: an off-axis parabolic mirror with a focal length of f = 400 mm and an f/d ratio of 1:5.6; the usable wavelength range between 200 nm and 4 µm; and the spectral resolution, which depends on the dispersion of the prism used (since the refractive index variation with wavelength affects resolution) as well as the entrance slit width. Determining the spectral line width is crucial for accurately measuring the radiation reaching the detector. For the purpose of constructing a measurement station in the UV spectral range, a quartz prism was selected.

The dispersion of the prism monochromator can also be expressed as the linear dispersion $\frac{d\lambda}{dx}$ in the focal plane of the mirror along the x-axis, which is perpendicular to the exit slit length. The linear dispersion is given by the following equation (for a prism in air):

$$\frac{d\lambda}{dx} = \frac{a}{b}\frac{1}{f}\frac{1}{\frac{dn}{d\lambda}} \tag{35}$$

Where:

- b is the base length of the prism,
- a is the beam width in the incident plane, perpendicular to the outgoing beam,
- *f* is the focal length of the monochromator mirror,
- dn/dλ is the material dispersion of the prism with refractive index n.

Given a specific linear dispersion dλ/dx determined by equation (35), the spectral bandwidth obtained is calculated as:

$$\Delta\lambda = s.\frac{d\lambda}{dx} \quad (36)$$

Where: Δλ is the spectral bandwidth and s is the width of the entrance slit.

The refractive index of quartz depends on the wavelength of light and is commonly expressed using the Sellmeier equation, a widely used empirical formula for describing the optical dispersion of materials. The Sellmeier equation for fused quartz is given as: [107].

$$n^2(\lambda) = 1 + \frac{B_1\lambda^2}{\lambda^2 - C_1^2} + \frac{B_2\lambda^2}{\lambda^2 - C_2^2} + \frac{B_3\lambda^2}{\lambda^2 - C_3^2} \quad (37)$$

Where:

- n(λ) is the refractive index at wavelength λ (measured in micrometers, µm).
- $B_1$, $B_2$, $B_3$ and $C_1$, $C_2$, $C_3$ are empirical coefficients.

For fused quartz at room temperature, the coefficients are:

- $B_1 = 0.6961663$, $C_1 = 0.06840432$
- $B_2 = 0.4079426$, $C_2 = 0.11624142$
- $B_3 = 0.8974794$, $C_3 = 9.89616120$

The parameters of the SPM2 monochromator are predetermined [106], and to balance the signal and the output resolution of the monochromator, an entrance and exit slit width of s = 0.7 mm was selected. The spectral line width for wavelengths ranging from 200 nm to 600 nm, determined using equation (37), is presented in Figure 35.

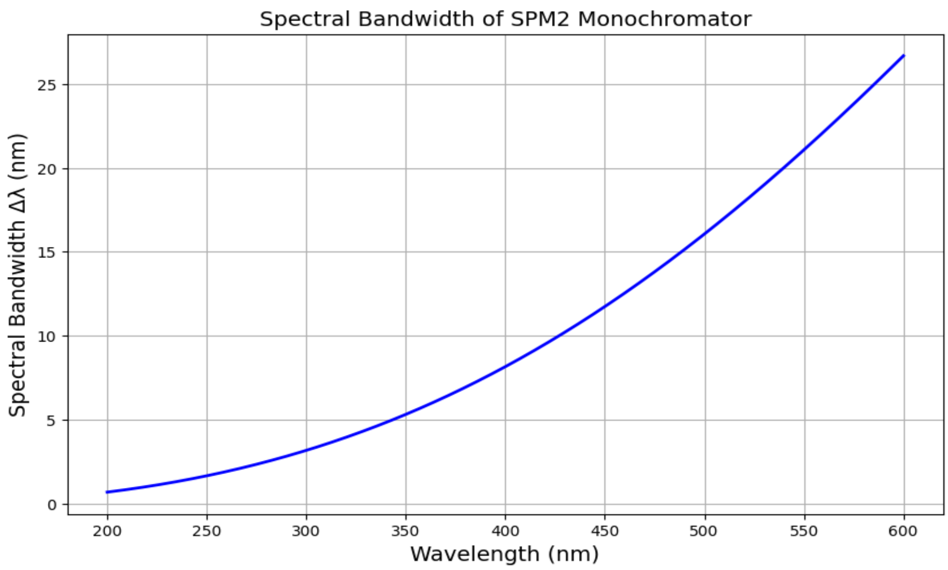


*Fig. 35. Spectral Bandwidth of SPM2 Monochromator*

A major drawback of the SPM2 monochromator is that the wavelength scanning process must be performed manually, making long-term radiation data collection challenging. Additionally, the output wavelength resolution depends on the material of the dispersing prism.

#### 6.1.1.3 Analysis of Monochromator Selection

As presented above, both diffraction grating monochromators and prism monochromators have distinct advantages and disadvantages. Table 12 compares key criteria of these two types of monochromators [108-109]:

Table 12. Compare the characteristics of the monchromator:prism and reflective diffraction grating

| | Prism | Reflective Diffraction Grating | Note |
|---|---|---|---|
| Dispersion Principle | Exploits differences in the material refractive index according to the wavelength | Exploits diffraction from a reflective surface with a regular grating structure. | |
| Light Utilization Efficiency | High (Generally has high efficiency despite light losses from boundary reflection and absorption during transmission through the material. A single prism covers the range from 185 to 2500 nm.) | Low (Light with the same wavelength is dispersed in several directions as higher-order light. High efficiency near the blaze wavelength.) | |
| Wavelength Dependency of Dispersion | High for UV; low for visible to NIR light. | High and approximately constant. | |
| Temperature dependency of Dispersion | High (Effects of temperature on refractive index.) | Low (Deformation due to temperature.) | |
| Higher-Order Light | None | Yes (Requires higher-order light cut-out filter.) | |

| | | | |
|---|---|---|---|
| Stray Light | Low | High (Dispersion due to higher-order light and surface roughness) | |
| Polarization | Low | High | |

Based on the comparison in the table above, selecting a prism-based monochromator is a reasonable choice, as it minimizes errors caused by higher-order diffraction and stray light when measuring weak background radiation. However, since the SPM2 monochromator only allows manual wavelength scanning, it poses limitations for long-term automated measurements. Automatic scanning will be implemented in the next phase of this dissertation

**6.1.2 Signal Detection and Processing System**

The system for receiving UV radiation signals follows the diagram shown in Figure 36. It consists of the following main components:

- Photomultiplier tube: Responsible for detecting weak UV radiation and converting it into an electrical signal.
- High-voltage source: Provides the necessary operating voltage for the PMT.
- Photon counting and analog mode: Enables signal processing either in photon-counting mode or analog mode, depending on the intensity of the detected radiation.
- Microcontroller: Manages data acquisition, controls system operation, and communicates with external devices.
- Software program: Interfaces with the microcontroller to process and visualize measurement data.

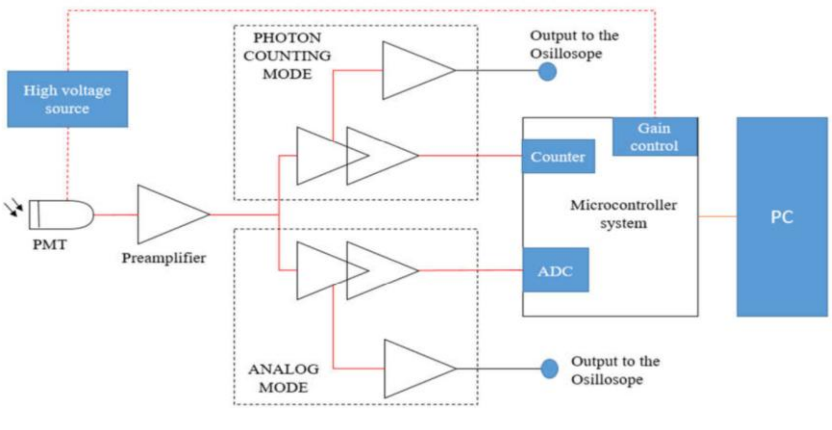


*Fig. 36. Block diagram of signal detection and processing system*

### 6.1.3. Photomultiplier Tubes

A photomultiplier tube is a vacuum tube consisting of an input window, a photocathode, focusing electrodes, an electron multiplication stage (dynodes), and an anode, all enclosed within a vacuum-sealed glass tube.

For this study, the ET-Enterprises 9402B photomultiplier tube was selected as the detector. The spectral characteristics of the PMT are shown in Figure 37.

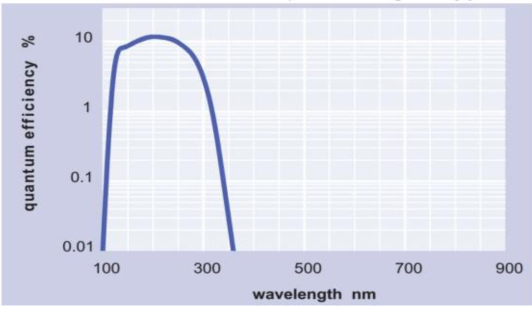


*Fig. 37. Spectral response curver [110]*

### 6.1.4. High-Voltage Source

For the PMT to operate, a high-voltage power supply unit is required to provide the necessary voltage. Additionally, the high-voltage source should allow for adjustable voltage levels to control the gain of the PMT via a microcontroller.

### 6.1.5. Analog and Digital (Photon Counting) Modes

Both analog and digital (photon counting) modes can be used to process the output signal of the photomultiplier tube depending on the incident light intensity, the output signal processing circuit design, and its bandwidth. When light strikes the photocathode of the PMT, photoelectrons are emitted, as illustrated in Figure 38. These electrons undergo multiplication within the dynode chain, typically increasing by a factor of $10^6$–$10^7$, before reaching the anode, which is connected to the output signal processing circuit.

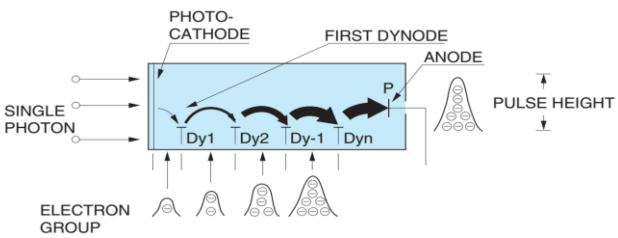


*Fig. 38. Photomultiplier tube operation in photon counting mode [111]*

When the light intensity is high, the time intervals between output pulses become shorter, leading to pulse overlapping and forming a continuous analog waveform. Conversely, when the light intensity decreases to extremely low levels, the output signal consists of discrete pulses, increasing the proportion of the AC component in the signal. The number of these discrete pulses can be digitally counted by distinguishing individual pulses at an appropriate binary threshold. This method is known as photon counting

### 6.1.6. Microcontroller

The microcontroller is responsible for:

- Processing signals in both pulse mode and analog mode: It counts pulses in photon counting mode and performs analog-to-digital conversion in analog mode.
- Controlling the high-voltage power supply for the photomultiplier tube.
- The microcontroller system used in the device is an STM32 Kit, featuring an ARM Cortex-M4F 32-bit microcontroller.

### 6.1.7. Software Program

The software program consists of two main components:

- Embedded microcontroller software: Handles signal processing and computations.
- User interface software: Allows parameter configuration input, displays measurement results, and stores data.

In Figure 39, the signal processing circuit for the photomultiplier tube is shown during laboratory testing.

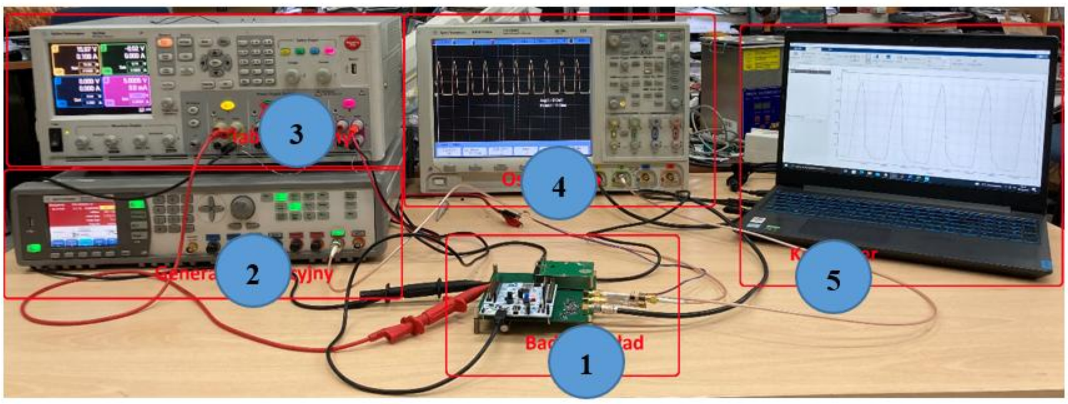


*Fig. 39. Photo of the complete measuring system*

1-Signal processing circuit; 2- Function generator; 3-Power supply; 4-scilloscope; 5-Computer

### 6.1.8 Optical System

An optical system is employed to focus the beam from the optical fiber output into the entrance slit. Figure 40 presents the schematic diagram of the beam focusing process into the monochromator.

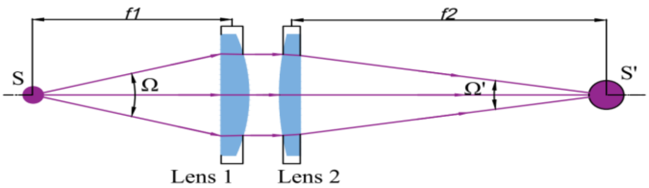


*Fig. 40. A lens pair collecting and focusing light from a source*

When coupling a light source to an optical system, whether it is an optical fiber or a monochromator, optimal coupling efficiency is achieved by matching the image (S') of the light source (S - fiber) to the width of the monochromator slit while ensuring that the solid angle (Ω') of the focused beam aligns with the acceptance solid angle of the monochromator.

The refractive index of glass exhibits strong dispersion in the ultraviolet region, leading to chromatic aberration in lens systems. To mitigate this effect, a parabolic mirror was selected as the optical element for focusing radiation from the source into the entrance slit of the monochromator. To minimize reflection losses, aluminum-coated mirrors were chosen for the optical system. Consequently, the coupling system employs a parabolic mirror setup, which provides a uniform reflectance across the UV region, improved beam focusing, and efficient fiber-optic coupling via an SMP connector. The schematic of the coupling system is illustrated in Figure 41

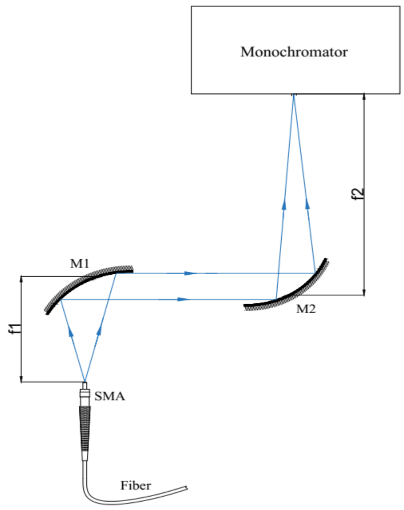


*Fig. 41. Mirrors system*

Mirror M1 collects radiation from the optical fiber and acts as a collimating mirror, producing a parallel beam directed toward mirror M2. Mirror M2 then focuses the beam onto the entrance slit of the monochromator. The lateral magnification of the system is determined by the ratio fM2/fM1, which is 3. With an optical fiber core diameter of 0.6 mm, the system produces a focal spot with a diameter of 1.8 mm at the monochromator's entrance focal plane.

### 6.2. Calibration

In addition to the monochromator and the high-sensitivity measurement system described earlier, the calibration of the station requires a reference light source with a well-characterized spectral distribution.

The calibration setup is illustrated in the following diagram:

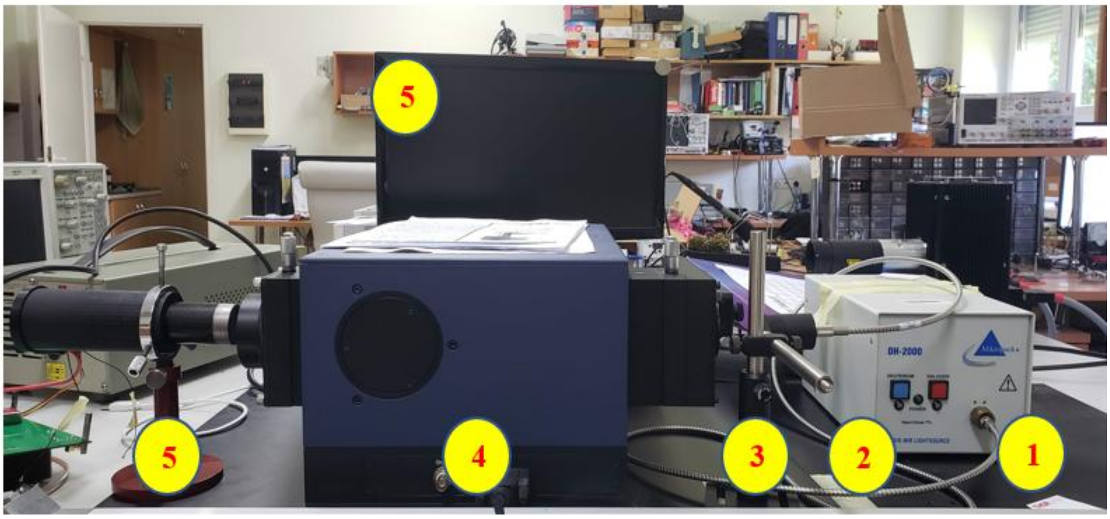


*Fig. 42. UV measuring station calibration diagram*

#### 6.2.1. The UV Light Source

For the calibration process, a light source with a known intensity profile and a continuous spectrum in the ultraviolet (UV) range is required. After evaluating various UV sources, the Ocean Optics DH-2000-CAL deuterium lamp was selected. The intensity characteristics of this source are provided by the manufacturer.

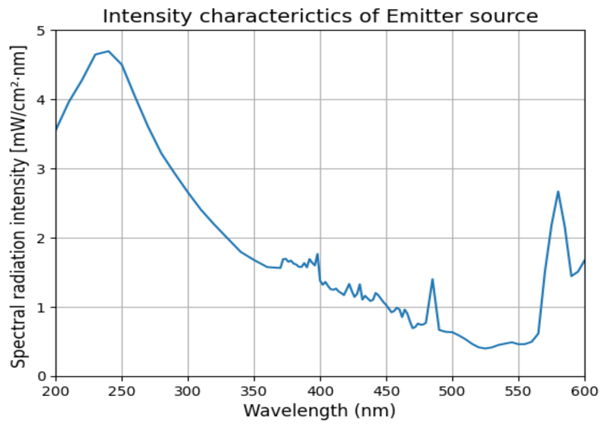


*Fig. 43. Spectral characteristics of Deuterium lamps (D2)*

Conversion to photon/s format:

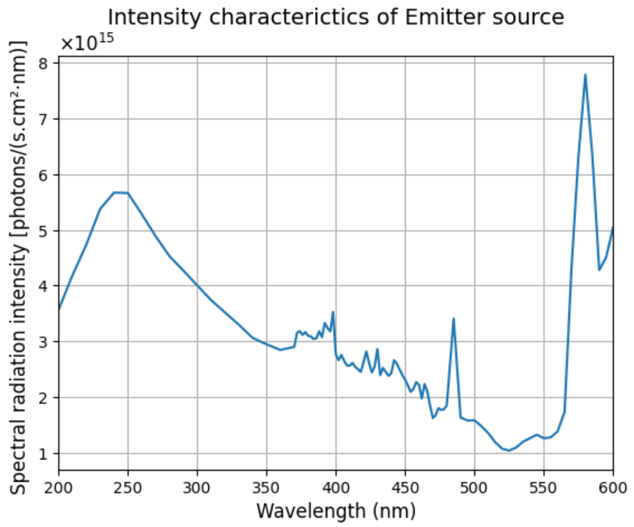


*Fig. 44. Spectral characteristics of Deuterium lamps in photons/s*

### 6.2.2. Radiometric Calibration Procedure for the Measurement Station

#### 6.2.2.1. Monochromator Calibration

To verify the proper operation of the monochromator-ensuring that its scale corresponds accurately to the output wavelength, the following calibration steps are performed:

- Select a monochromatic light source with a narrow spectral bandwidth and a known wavelength.

- Set the monochromator scale to the position corresponding to the selected source wavelength.

- Position a photodiode detector at the monochromator's output so that the output plane is directly behind the exit slit and perpendicular to the optical axis (using an optical rail for precise alignment).

- Manually adjust the wavelength selection knob to scan around the preset wavelength and identify the position where the detector records the maximum signal. This position on the monochromator scale corresponds to the wavelength of the selected light source.

- Repeat the process multiple times to ensure accuracy.

For calibration, we use an Nd:YAG laser at 532 nm as the light source and a PIN photodiode (FDS100) as the detector.

**6.2.2.2. Calibration of the Measurement Station**

Figure 45 illustrates the transfer function in the calibration of the measurement station.

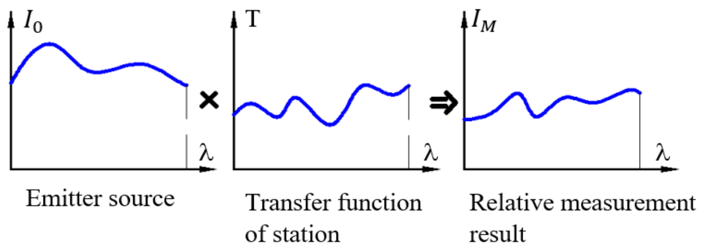


*Fig. 45. The influence of the position on the recorded signal*

The photon count value of the measurement station can be expressed by the relation:

$$I(\lambda) = I_0(\lambda).T_{fiber}(\lambda).T_{optic}(\lambda).T_{Monochromator}(\lambda).\eta_{PMT}(\lambda) \quad (38)$$

Where:

- $I(\lambda)$ is Detected photon count [photon/s]
- $I_0(\lambda)$ is Photon count emitted by the source at the fiber input [photon/s]
- $T_{fiber}(\lambda)$ is Transmission coefficient of the optical fiber [%]
- $T_{optic}(\lambda)$ is Transmission coefficient of the optical system [%]
- $T_{Monochromator}(\lambda)$ is Transmission coefficient of the monochromator [%]
- $\eta_{PMT}(\lambda)$ is Quantum efficiency of the PMT photocathode.

Since the transmission characteristics of the monochromator are entirely unavailable, and energy losses due to absorption and scattering within the system components inevitably occur during operation, the overall transmission coefficient of the measurement station is determined experimentally. This is achieved using an Nd:YAG laser at a wavelength of 532 nm and a PiN photodiode detector to measure the ratio of the output signal to the input signal, as described by the following relationship:

$$\gamma = \frac{U_{out}}{U_{in}} \quad (39)$$

Where:

- $\gamma$: Transmission coefficient of the measurement station (excluding PMT) at the 532 nm wavelength of the Nd: YAG laser.

- $U_{out}$: Voltage value proportional to the measured radiation power at the monochromator exit [V].

- $U_{in}$: Voltage value proportional to the measured radiation power at the fiber optic input[V].

Thus, the number of photon incidents on the photocathode surface is determined as follows:

$$n_{in}(\lambda) = I_0(\lambda).\gamma/\Delta\lambda(\lambda) \quad (40)$$

Where:

- $n_{in}(\lambda)$ is the number of photons incident on the photocathode surface [1/s]
- $\Delta\lambda$ is the spectral bandwidth of the monochromator from equation (36).

Thus, $n_{in}(\lambda)$ can be calculated using the spectral characteristics of the calibration source $I_0(\lambda)$, the coefficient $\gamma$ from Equation (39), and the spectral bandwidth $\Delta\lambda$.

Assuming $n_{out}(\lambda)$ is the number of photons detected at the output of the measurement station (PMT) when the number of photons emitted from the source at the fiber optic input is $I_0(\lambda)$ the measurement station calibration factor $H(\lambda)$ is determined as follows:

$$H(\lambda) = \frac{n_{in}(\lambda)}{n_{out}(\lambda)} \quad (41)$$

The steps for determining the calibration factor are as follows:

- The light source is turned on and allowed to stabilize for a period of time to ensure stable operation.
- The spectral range is measured from 250 nm to 300 nm with a scan step of 5 nm.
- The entrance and exit slits of the monochromator are set to a width of s=0. 7 mm.
- The voltage supplied to the PMT is set to 1.6 kV.
- The threshold voltage is set to 700 mV.

The results obtained are presented in the figure 46.

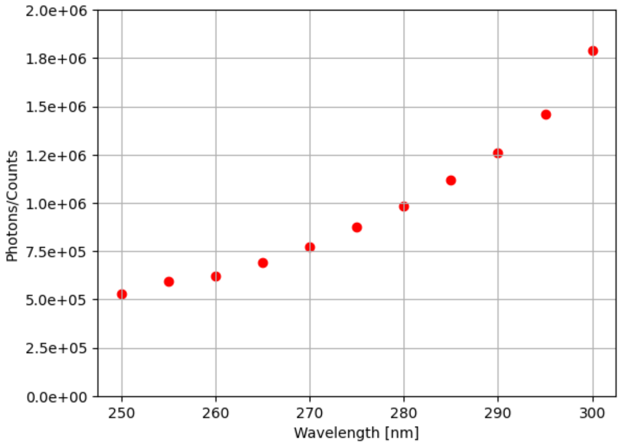


*Fig. 46. Calibration Factor of the Measurement Station*

The calibration values are presented in Figure 47 and are used to calculate the actual number of background radiation photons.

Accordingly, the background radiation measurement system has been fully developed, including installation, testing, and calibration under laboratory conditions. Following this stage, the device is deployed for field measurements to evaluate its operational performance under real conditions. This constitutes a critical evaluation step, providing the basis for accurate measurement and reliable acquisition of background UV radiation data.

### 6.3. Testing, Calibration, and System Upgrading

#### 6.3.1. Installation of the Measurement Station

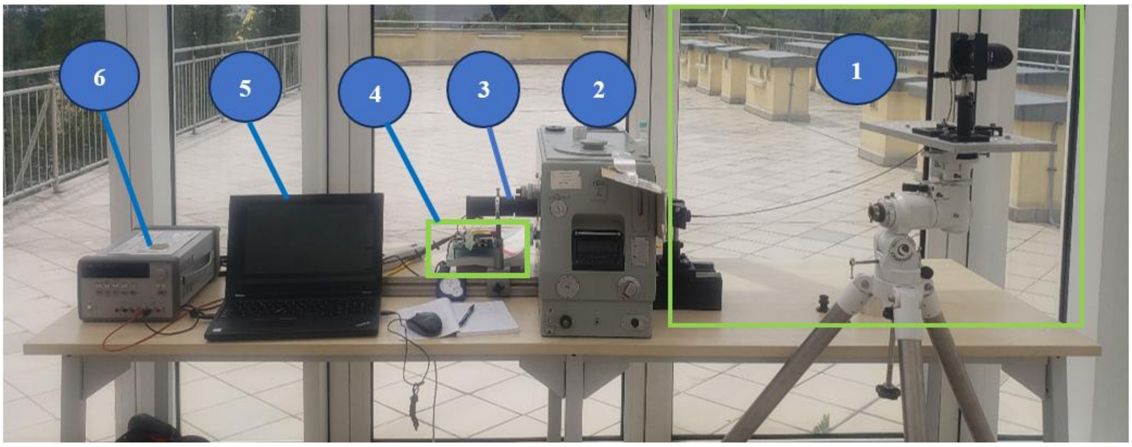


*Fig. 47. Setup of the Measurement System on the Roof of the IOE Building*

(1) Optical System – Collects radiation from the environment and directs it into the entrance slit of the monochromator.

(2) Monochromator – Selects specific wavelengths from the collected radiation.

(3) Photomultiplier Tube – Detects the filtered radiation and converts it into an electrical signal.

(4) Electronic Circuitry

(5) Computer Software

- Interfaces with the electronic circuit.
- Controls the PMT operation, setting parameters such as measurement time and wavelength range.
- Stores measured data in CSV files and displayed real-time results.

(6) Power Supply

The wavelength is scanned in the range of 200 nm to 300 nm with a resolution of 5 nm.At each wavelength, the number of detected photons per second is counted. The measurement is repeated 10 times, and the average value is taken. The measurement results are saved in a CSV file for further analysis.

### 6.3.2. Factors Influencing Field Measurements

Background UV radiation at the Earth's surface is of very low intensity. The use of a high-gain photomultiplier tube enables the detection of such low-level radiation; however, it also introduces significant noise, which is influenced by multiple factors.

Background UV radiation data were collected at various times between June and October 2023. Although a large volume of data was recorded, only representative measurement results obtained from the UV radiation monitoring station are presented within the scope of this study.

Based on these results, potential system upgrades are proposed to improve the stability and reliability of the measurements. Representative background UV radiation measurements acquired using the developed UV measurement station are presented below.

Meteorological conditions: During the background UV radiation measurements, meteorological conditions were relatively stable. The ambient temperature ranged from 28 °C to 33 °C, with relative humidity between 30% and 40%. The sky was mostly clear with light cloud cover. Images of the sky at different measurement times are shown in Figure 48

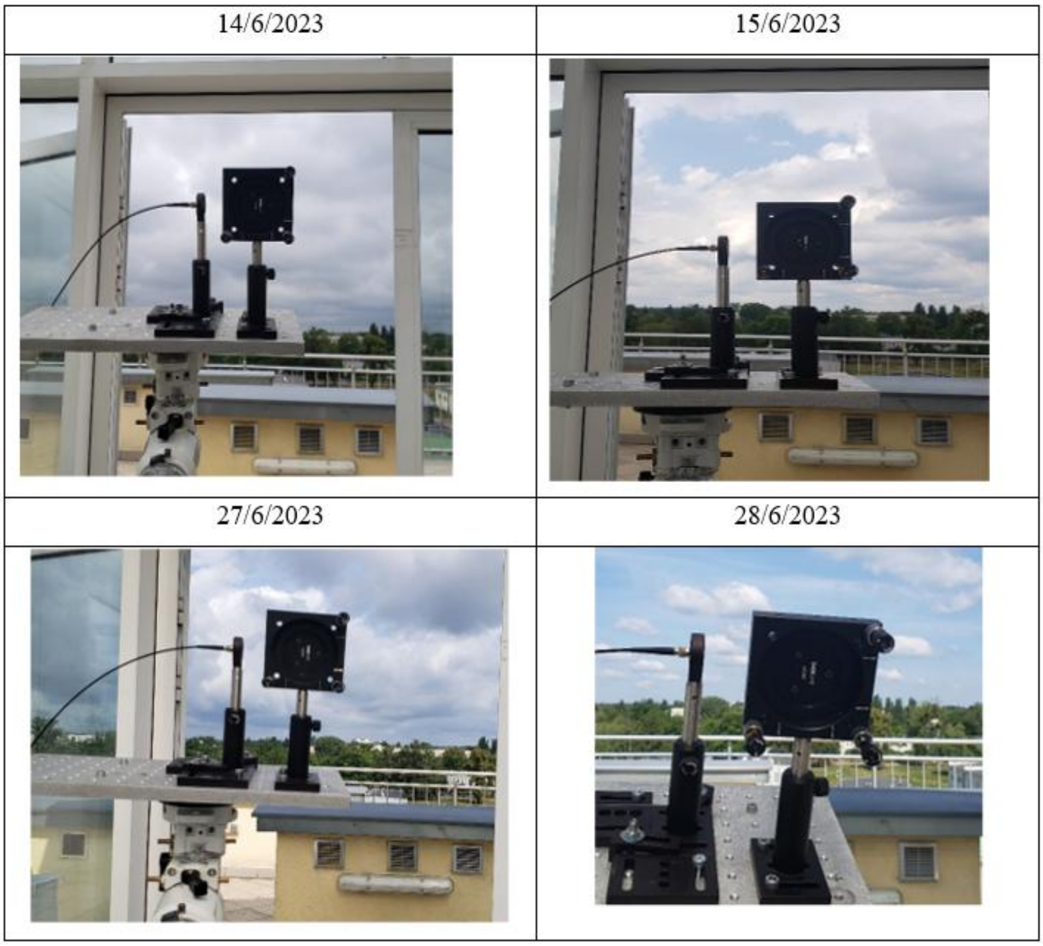


*Fig. 48. The sky background at certain times measured UV radiation*

Figure 49 illustrates several representative measurement results, which reveal the presence of noise and signal fluctuations during the data acquisition process.

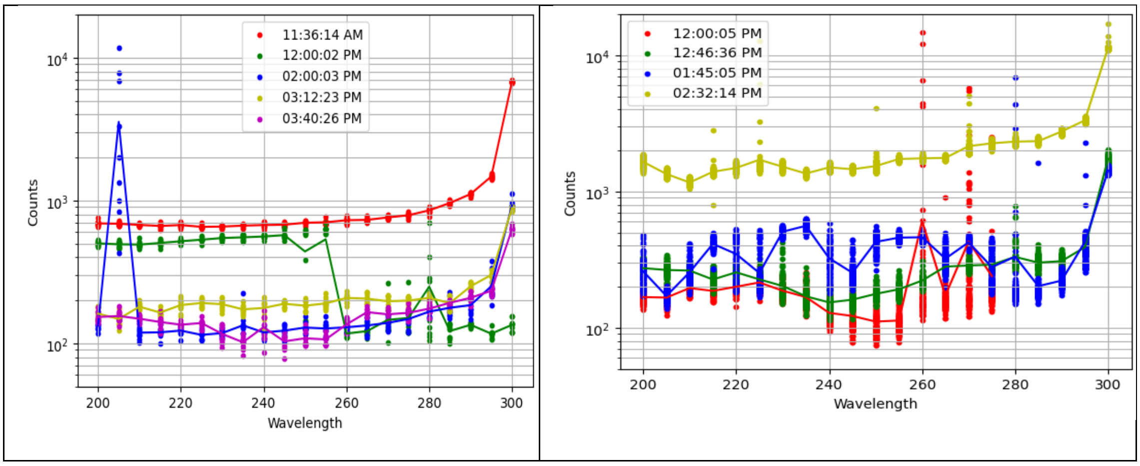


*Fig. 49. Noise and fluctuations during the data acquisition process*

Observations from Figure 49 indicate that the spectral characteristics of the radiation are affected by noise, resulting in sudden variations in the number of detected photons

at certain wavelengths. The measured results show that background UV radiation varies with the time of day, reaching a maximum around noon and gradually decreasing in the afternoon. However, noise measurement and signal fluctuations remain significant.
The primary sources of these effects are electromagnetic interference and stray light. To mitigate these issues, the following measures were implemented:

- The electronic circuitry and the photomultiplier were enclosed in a shielded housing to reduce electromagnetic interference, and shielded cables were used for signal connections.
- The entire measurement system, including the optical components and the monochromator, was covered with black fabric to prevent external stray light from entering the system and affecting the measurement accuracy.

After calibration and system upgrades, the results obtained demonstrate that the major sources of interference were effectively reduced. Subsequent measures and data acquisition were then carried out under improved and more stable conditions.

## 7. Background UV radiation.

### 7.1. Measurement of background UV radiation.

The measurement stand was installed on the rooftop of the Institute of Optoelectronics building, located at geographic coordinates: latitude 52.2° N and longitude 21° E. The stand was configured to measure diffuse radiation from the atmosphere. The setup diagram of the measurement stand is shown in Figure 50.

The diffuse component of solar radiation, after propagating through the atmosphere, is focused by a parabolic mirror (1). This mirror has a clear aperture of $D =$ 2 inch and an effective focal length of $f' = 6$ inch (numerical aperture $F/\# = 3$). The beam focused by mirror (1) is directed to the input of an optical fiber (2). The output of the fiber is coupled to a mirror–lens system (3) to form a beam of suitable size for the entrance slit of the SPM-2 prism monochromator (4).At the output of the monochromator, an ET-9402B photomultiplier tube (5), optimized for operation in the UVC range, is installed and operated in photon-counting mode. Signals from the photomultiplier are recorded by the data acquisition system (6).

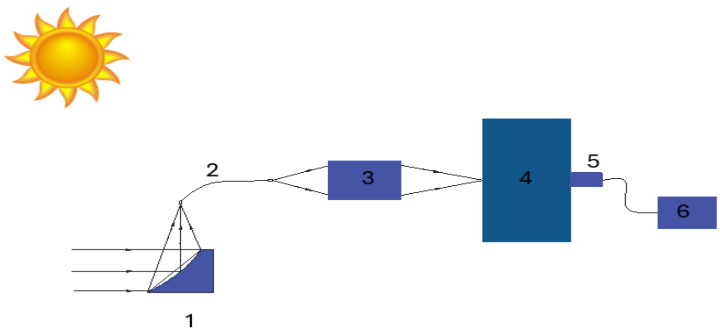


*Fig. 50. Schematic of measurement stand*

*1-off-axis parabolic mirror, 2 – optical fiber (d=0.6mm); 3-Optical lens; 4-monochromator SPM-2; 5– PMT ET-4902B,; 6 – data acquisition system*

The number of counts recorded in a measurement by the data acquisition system and the number of photons of the diffuse solar radiation incident on the measuring system are related by the following expression:

$$n_{\mathrm{cnt}}(\lambda) = n_{\mathrm{ph}}(\lambda) \cdot T(\lambda) \cdot \eta(\lambda) \quad (42)$$

Where:

- $n_{\mathrm{cnt}}(\lambda)$: number of counts recorded by the data acquisition system at wavelength $\lambda$;
- $n_{\mathrm{ph}}(\lambda)$: number of photons incident on the optical system at wavelength $\lambda$;

- $T(\lambda)$: total transmittance of the optical system, including the off-axis parabolic mirror (1), optical fiber (2), optical coupling system (3), and the monochromator (4).
- $\eta(\lambda)$: quantum efficiency of the photomultiplier tube.

Each component of the measurement system exhibits its own spectral characteristics within certain tolerances. In addition, for the monochromator, the spectral transmission characteristics are not precisely known. Therefore, a calibration procedure (as presented in the previous chapter) must be performed.

The calibration process aims to determine the calibration coefficient $K(\lambda)$, which enables the conversion of the recorded counts into the number of incident photons of diffuse ultraviolet radiation reaching the measurement system. The relationship between the counts, the incident photons, and the calibration coefficient is given by:

$$N_{\mathrm{ph}}(\lambda) = N_{\mathrm{cnt}}(\lambda) \cdot K(\lambda) \tag{43}$$

Where:

- $N_{\mathrm{cnt}}$: total number of counts recorded per second by the data acquisition system at wavelength $\lambda$.
- $K(\lambda)$: calibration coefficient at wavelength $\lambda$;
- $N_{\mathrm{ph}}(\lambda)$: total number of photons incident per second at wavelength $\lambda$.

The radiant power collected by the optical system can be expressed as:

$$\Phi(\lambda) = N_{\mathrm{ph}}(\lambda) \cdot \frac{hc}{\lambda} \tag{44}$$

On the other hand, the radiant flux at the detector (i.e., the total energy received per unit time, in watts) can be expressed in terms of the spectral radiance $L(\lambda)$(W·m$^{-2}$·sr$^{-1}$·nm$^{-1}$) as follows:

$$\Phi(\lambda) = L(\lambda) \cdot \mathrm{A} \cdot \frac{\pi}{4(F\#)^2} \tag{45}$$

Where:

- A: effective area of the optical fiber
- $F \quad = f/D$

  : parabolic mirror's F-number (numerical aperture).
- $L(\lambda)$: spectral radiance of the source or scene, defined per unit area and per unit solid angle.

From this, it can be derived that:

$$L(\lambda) = \frac{4(F/\#)^2}{\pi A}\,\Phi(\lambda) \tag{46}$$

Atmospheric conditions during the measurement period:

The data collection was carried out in August 2025. The general atmospheric conditions during the measurements were characterized by sunny weather with no rain, the presence of light cumulus clouds, and occasional occurrences of dense cloud formations. Figure 51 presents several images of the sky captured during the measurement period. The presence of clouds also had a significant influence on the measured background radiation values.

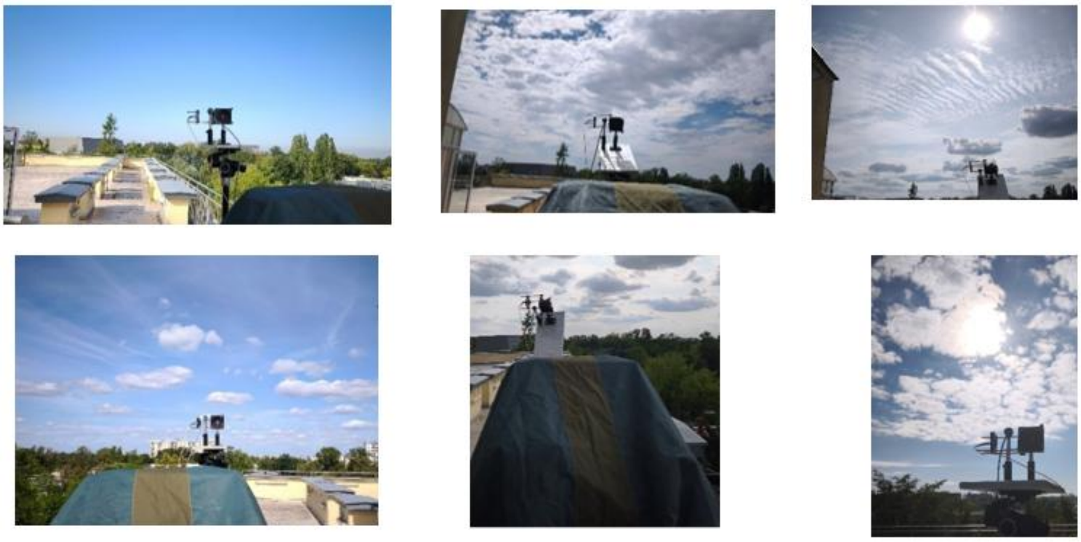

*Fig. 51. Sky background images*

**Sun position:**

The objective of the measurement process was to record the diffuse background radiation in several specific observation directions. Therefore, the position of the Sun could influence the selection of measurement directions and the timing of the measurements.

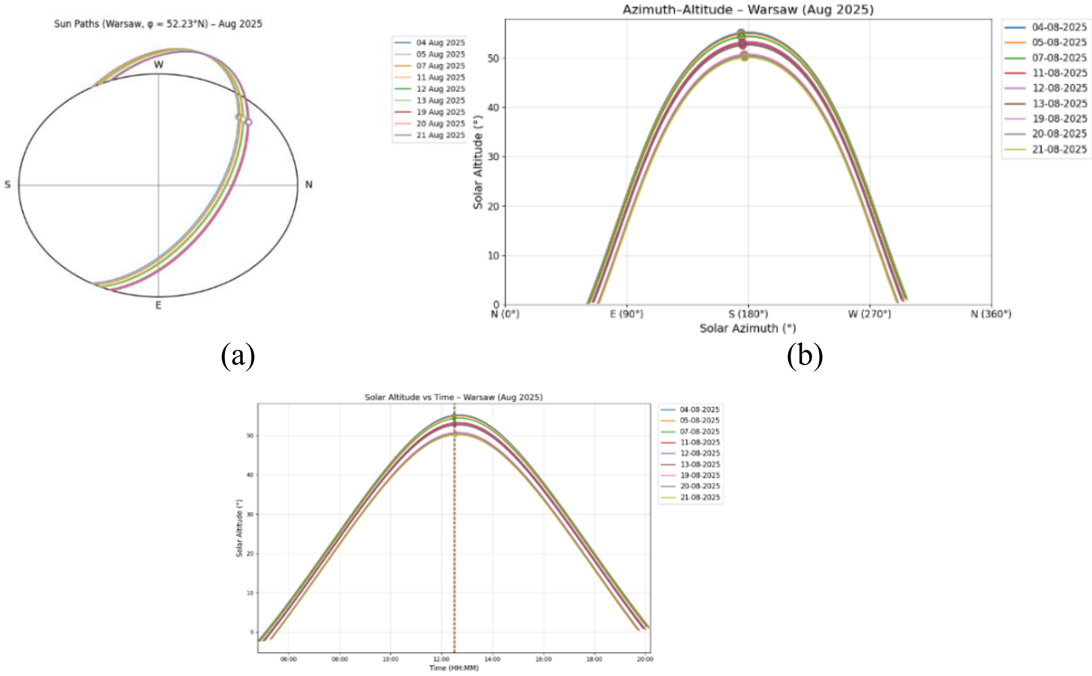


(a) (b)

(c)

*Fig. 52. Location of the Sun*
*(a)- Sun's paths, (b) - Solar altitude vs solar azimuth, (c)- Solar altitude vs time*

Figure 52 illustrates the Sun's trajectory, including the solar elevation angle as a function of azimuth and its variation over the course of the day at the measurement site. The results shown in Figure 52 indicate that the Sun's path is symmetric along the East–West direction and slightly shifted toward the North. Consequently, during the data acquisition process, measurements were conducted toward the East, North, and South directions.

UV radiation was measured in Warsaw throughout the day. Data was recorded from 8:00 a.m. to 4:00 p.m. local time. For each measurement series, the radiation spectrum in the 250–295 nm range was acquired with a spectral resolution of 5 nm. The acquisition time for each wavelength was set to 10 seconds. Photon-count results were calibrated over the 250–295 nm range. The detector head orientation varied across specific directions, and the sensor elevation angle was set in turn to 0°, 30°, and 60°.

The measurement results are presented in Figures 53, 54, and 55, corresponding to August 4, 2025; August 5, 2025; and August 7, 2025, respectively.

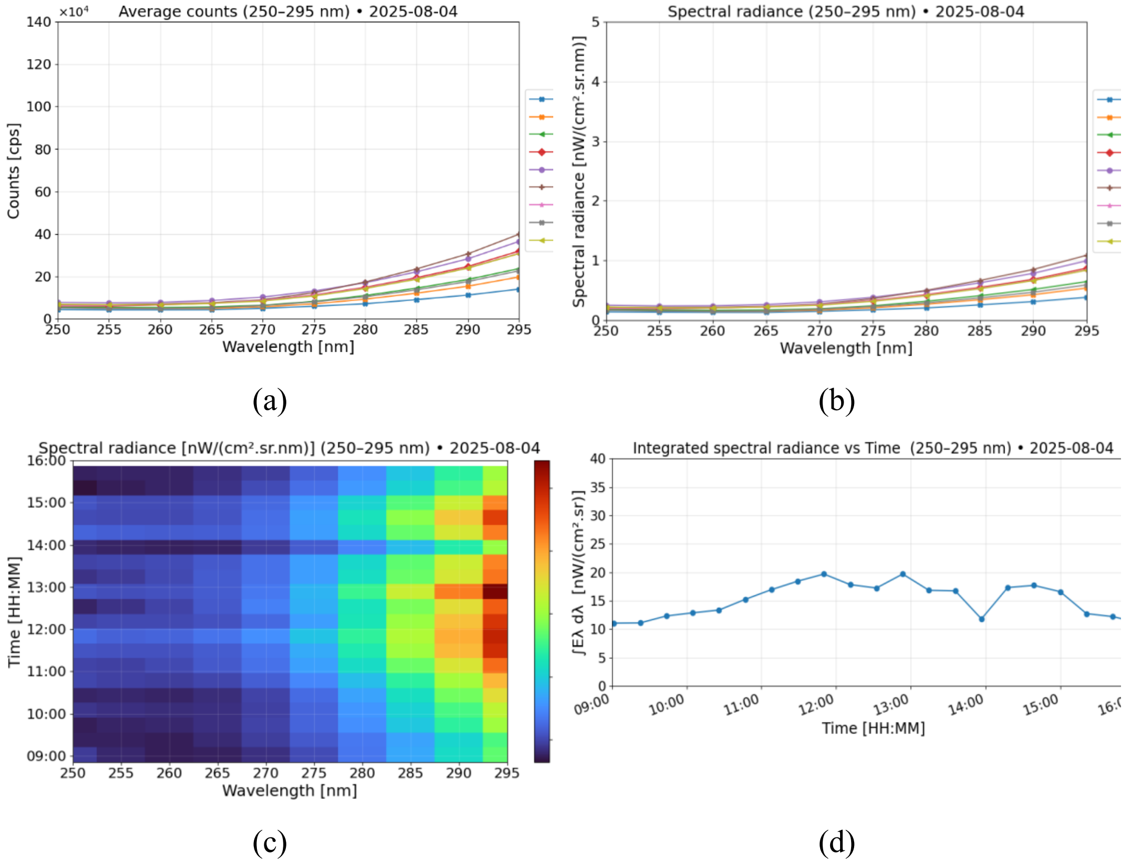


*Fig. 53. Background UV radiation. Measurement direction: South. Elevation angle: 0° (a) - calibrated photon counts per second in the 250–295 nm, (b)- spectral radiance, (c)- a pseudo-color map of spectral radiance, (d) - wavelength-integrated spectral radiance*

In Figure 53, the panels show, respectively: (a) calibrated photon counts per second in the 250–295 nm wavelength range; (b) spectral radiance; (c) a pseudo-color map of spectral radiance versus wavelength and time of day; and (d) the wavelength-integrated spectral radiance as a function of time of day.

From Fig. 53, the shapes of the background spectral count-rate curve (photons $s^{-1}$) and the spectral-radiance curve are very similar, since spectral radiance is computed from the detected photon counts together with the photon energy. Therefore, in the subsequent results we present only (i) the spectral-radiance-versus-wavelength curves and (ii) the pseudo-color map of spectral radiance versus wavelength and time of day, as these provide a clearer overview of the spectral energy distribution. Figures 55 and 56 show the background radiation for the same southward viewing direction with sensor elevation angles of 30° (Fig. 54) and 60° (Fig. 55), respectively.

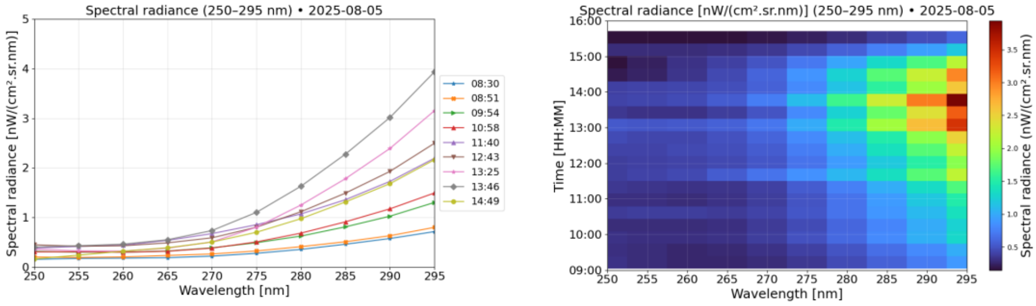


*Fig. 54. Background UV radiation. Measurement direction: South. Elevation angle: 30°*

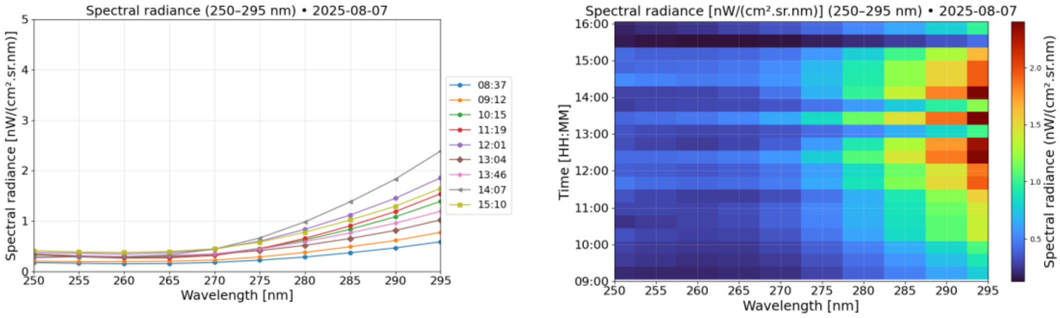


*Fig. 55. Background UV radiation. Measurement direction: South. Elevation angle: 60°*

From these measurements, a non-zero background UV radiation is present in the 250–295 nm band. The radiance level depends on wavelength, time of day, meteorological conditions, and day-to-day variations in the Sun's trajectory. The spectra peak around local noon and toward the longer wavelengths. The retrieved background level also varies with the sensor's elevation angle. Figure 55 shows the wavelength-integrated spectral radiance (250–295 nm) at different times of day, across different dates, for sensor elevation angles of 0°, 30°, and 60° relative to the horizontal.

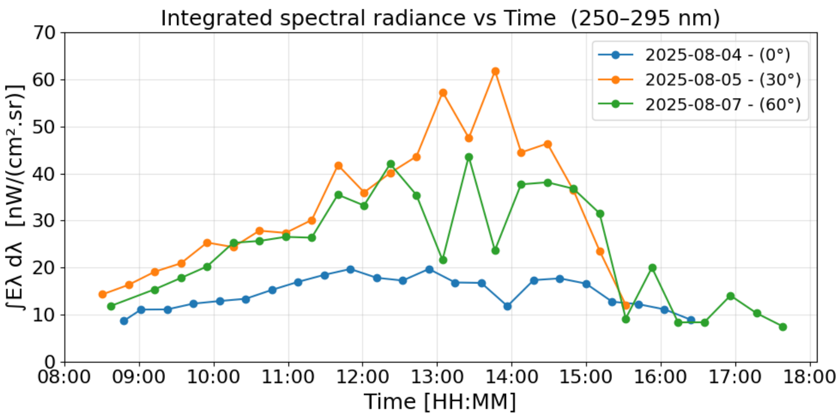


*Fig. 56. Wavelength-integrated spectral radiance. Measurement direction: South*

It is evident that changing the sensor's elevation angle alters the background UV level. The wavelength-integrated spectral radiance tends to increase with elevation angle;

however, the increase is not proportional to the angle, as it also depends strongly on the measurement time, meteorological conditions, and cloud cover. Figure 56 shows that, within the 250–295 nm band, the radiance ranges from approximately 10 to 60 nW/m².

To determine how the background UV varies with viewing direction, additional measurements were performed for different pointing directions, following the same procedure as above.

## 7.2. Investigation of Diffuse UV Background Radiation with Viewing Direction

Figure 57 shows the background measurements when the sensor points East, with elevation angles of 0° (Fig. 57a), 30° (Fig. 57b), and 60° (Fig. 57c)

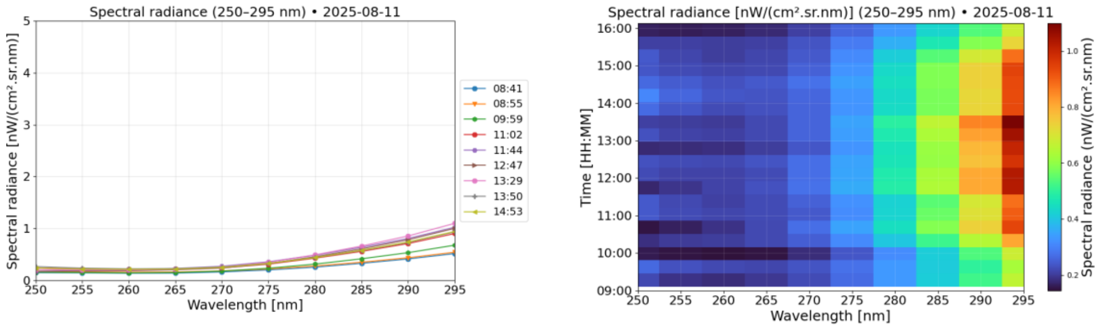


(a)

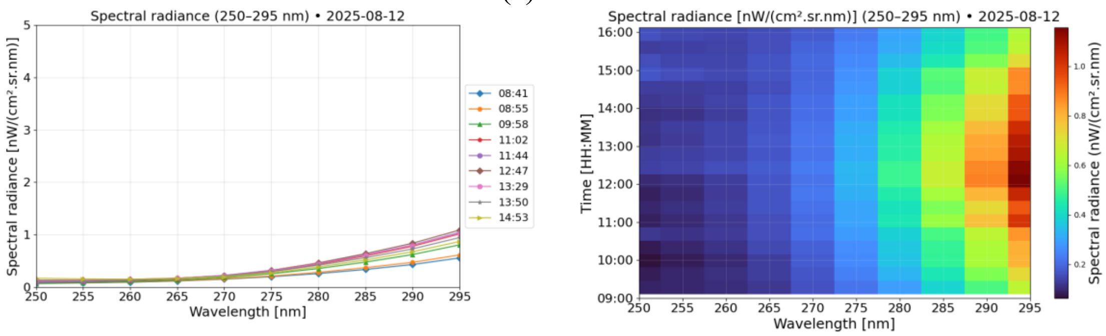


(b)

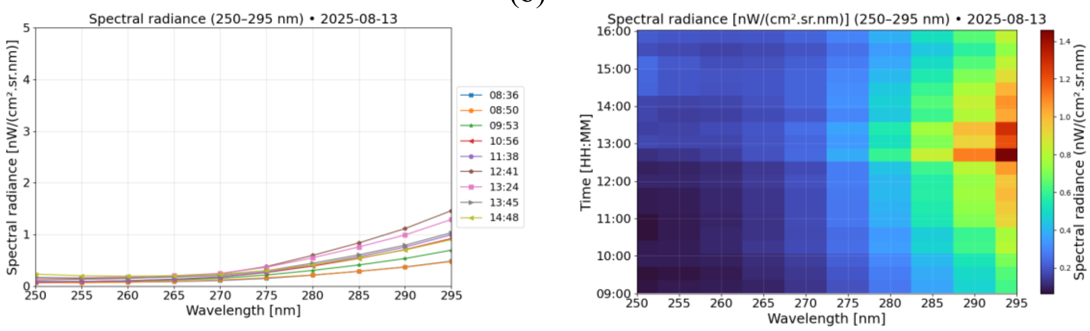


(c)

*Fig. 57. Background UV radiation. Measurement direction: East*

*(a) elevation 0°, (b) 30°, (c) 60°*

Figure 58 presents the background measurements when the sensor points North, with elevation angles of 0°, 30°, and 60°, respectively.

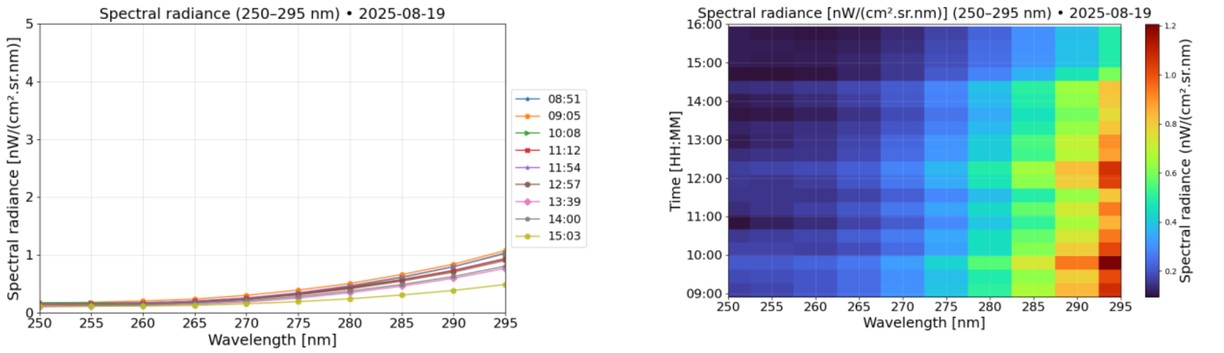


(a)

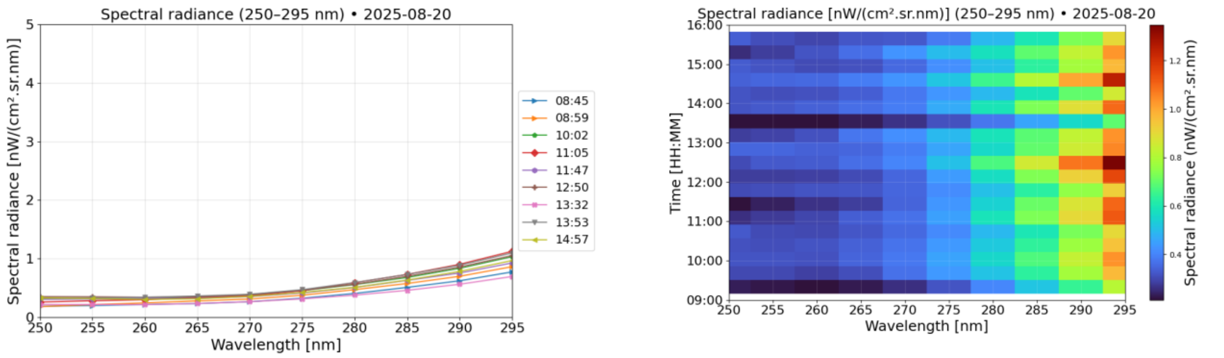


(b)

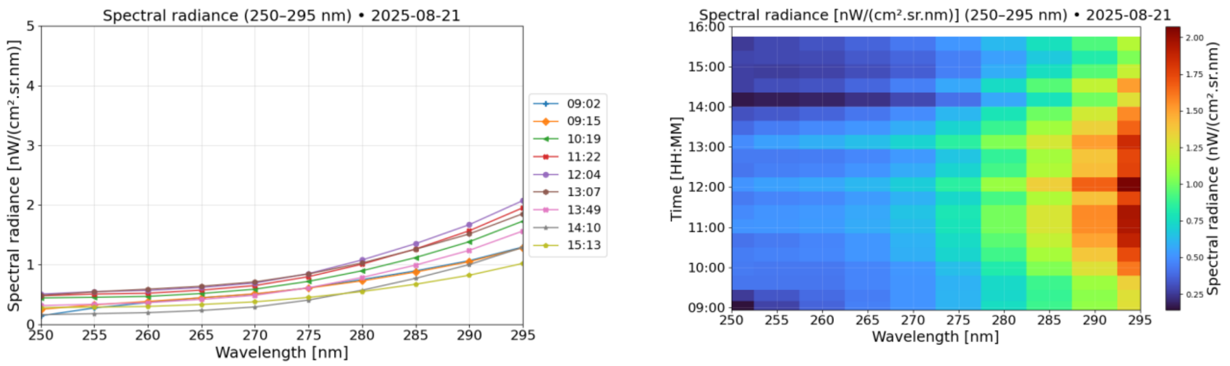


(c)

*Fig. 58. Background UV radiation. Measurement direction: North*

*(a) elevation 0°, (b) 30°, (c) 60°.*

The results of the wavelength-integrated spectral radiance for different viewing directions and sensor elevation angles are shown in Figure 59.

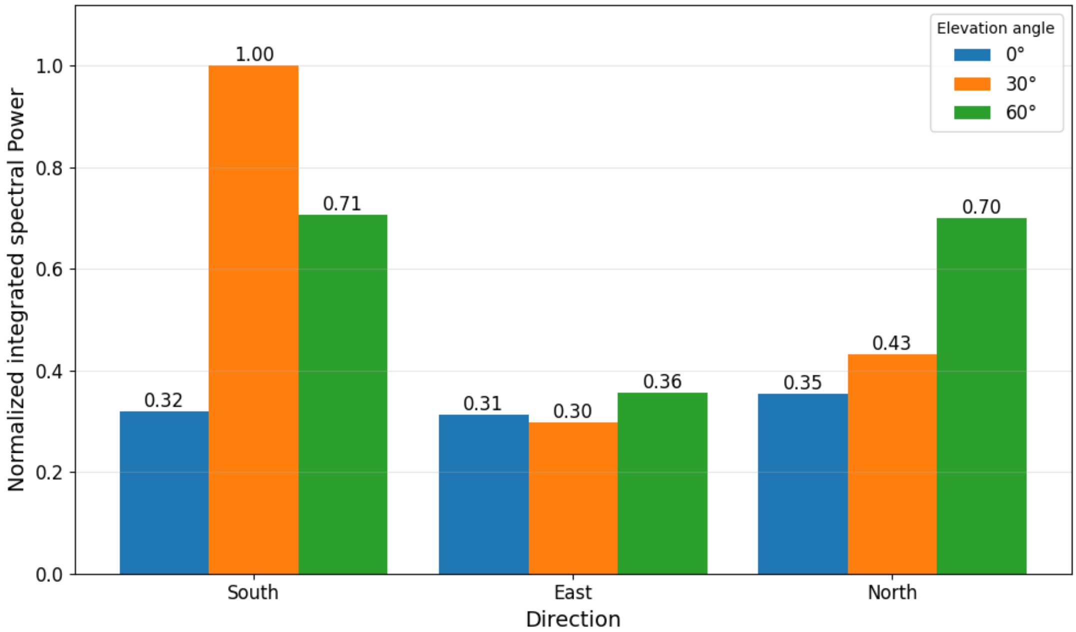


*Fig. 59. Normalized integrated spectral Power*

From the directional investigations, we observe that:

- Changing the viewing direction and elevation angle affects the measured background UV level.
- When the sensor is kept horizontal (0° elevation), the relative background level is nearly unchanged.
- As the elevation angle increases, the measured background UV generally increases.

Apart from meteorological factors (clouds, haze, etc.), changes in the sensor's viewing direction also modify the measured diffuse UV radiation because the Sun's apparent trajectory relative to the site varies by date, and the viewing azimuth relative to the Sun changes throughout the day.

### 7.3. Summary

The UV measurement results and UV background investigation prove that the applied UV sensor (photomultiplier tube) can detect background UV radiation at wavelengths greater than 250 nm. Below this threshold (≈200–245 nm) number of photon counts is very low and approximately at the level of the detector's intrinsic noise. Author's finding that background radiation appears in the solar-blind UV region is an important factor for designing and evaluating sensors operating in this band.

Within the 250–295 nm range, the station records incident photon counts. The spectral radiance lies in the range of 0.1–5 $nW \cdot m^{-2} \cdot nm^{-1}$, and the wavelength-integrated spectral radiance over 250–295 nm is about 10–60 $nW \cdot m^{-2}$. This indicates that under real atmospheric conditions a residual UV background persists within the solar-blind region.

The results also show substantial variability of diffuse background UV with meteorological conditions, time of day, day-to-day changes, and with the sensor's elevation angle and viewing direction. In addition, latitude / the Sun's apparent path influences the background level. These factors are important for the design and optimization of detection systems, especially for applications requiring high sensitivity.

The presence of residual diffuse UV background in the solar-blind region can significantly affect UV-source detection in practical applications (e.g., Missile Warning System (MWS) via plume UV emission, fire warning and monitoring, or other high-temperature sources). This residual background can reduce the signal-to-noise ratio (SNR) and compress the system's dynamic range. Therefore, it should be accounted for in design models, and detection systems should be adapted to real-world conditions.

## 8. UV negative contrast of aircraft in 300-400 spectrum

In recent armed conflicts, unmanned reconnaissance and combat devices have been widely and effectively used. Drones have become a central weapon in the Russia–Ukraine war, with the number of unmanned systems-mostly aerial but not exclusively- reaching astonishing levels. It is estimated that around 100 different types of drones are being used in Ukraine, ranging from toy-sized systems to larger models with wingspans approaching 20 meters [112].

UAVs (Unmanned Aerial Vehicles) are typically small and equipped with low-power engines, resulting in thermal emissions that are shifted toward the long-wave infrared (LWIR) region. The thermal signature of a target is a complex function that varies depending on several parameters such as geometric structure, radiative flux in different areas, and the target's dynamic state, among others. These variations require infrared seekers to be developed with specific characteristics to counter flying platforms:

- Weak thermal signatures shift the radiation peak toward the LWIR region.
- Active protection technologies on UAVs (such as DIRCM – Directional Infrared Countermeasures) to counter infrared-guided missiles.

Currently, there is a global trend toward developing new-generation infrared seekers by enhancing detector sensitivity, employing multi-spectral detectors operating in the long-wave infrared band or using UV anti-contrast techniques, and utilizing imaging focal plane arrays. There is also a focus on accelerating signal processing and analysis through improved electronic circuitry systems…

### 8.1. Target Detection in the UV Background Scene

As discussed in the previous chapter, natural sources of UV radiation primarily originate from solar radiation. For applications near the Earth's surface, solar UV radiation is absorbed by ozone, allowing only UV-A and a portion of UV-B to reach the surface. As a result, the UV radiation background is relatively uniform and less affected by natural noise sources.

However, in practice, artificial noise sources may appear within the field of view of detection devices operating in the ultraviolet range. If these artificial sources are strong enough, the resulting noise signal on the detector may exceed the signal from an aerial target-leading to a failure in detection or loss of the target.

The following section presents a target discrimination method based on negative contrast, which is employed in the seeker heads of certain modern man-portable missiles that utilize dual-channel IR/UV guidance.

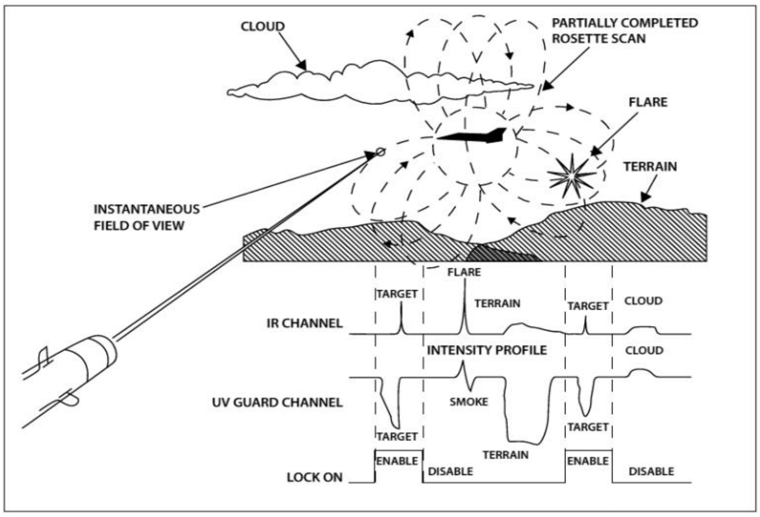


*Fig. 60. Theory of dual band Rosette Scan Missile Seeker [7]*

Several published studies have shown that the optical system of the Stinger POST missile seeker is designed to detect targets in two spectral bands: IR and UV. The CdS detector is sensitive in the UV spectrum, while the InSb detector is sensitive in the MWIR band. The modulated radiation-both from the background and the target-generates an electrical signal proportional to the incoming radiation intensity in both the UV and MWIR bands within the dual-band detection system [13]. The actual target in the thermal scene appears with positive contrast in the IR band but negative contrast in the UV band.

Figure 60 illustrates a third-generation MANPADS using a rosette scanning seeker and a UV guard channel. The rosette scanning seeker is an example of a "pseudo-imager" system, in which a small instantaneous field of view (IFoV) is scanned across the entire field of view in a rosette pattern. This allows the system to detect light intensity from specific areas within the scene, thereby constructing an image over the duration of a complete scan [7]. To distinguish a target from flares or the sun, the UV channel is employed. Flares and the sun produce strong positive contrast in the UV band, whereas the target generates negative contrast. As shown in Figure 60, when the pulse amplitudes of both channels at the same moment have opposite signs relative to their reference levels, the seeker interprets the signal as originating from a valid target. Conversely, if both bands show the same sign, the system interprets the source as a false target, such as a cloud. “If both spectral bands exhibit the same signature, the seeker regards the sequence as a false target, e.g., a flare” [7], [113],[114].

The input signal at each sensor is a combination of several components: target signal, flare, background (e.g., clear sky), and noise. To analyze the pulse characteristics in the input sequence, a reference level must be defined for both the UV and IR bands. However, due to the presence of noise, determining these reference levels is challenging. If the reference level is incorrectly set, the system may fail to distinguish a target pulse and risk misidentifying false signals (e.g., flares) as actual targets.

### 8.2. Negative Contrast in the near UV Spectrum

#### 8.2.1. Components of the UV Scene

The term optical signature refers to the radiometric features of an object, which include its self-emitted radiation, transmitted radiation, and the portion of incoming radiation reflected from its surface. These optical characteristics are influenced by various object-specific and atmospheric factors. The primary influencing parameters are:

- Object characteristics: including size, geometry, surface temperature, texture, emissivity, and reflectivity.
- Environmental conditions: such as solar zenith angle, geographic location, time of day and season, as well as aerosol density and type.

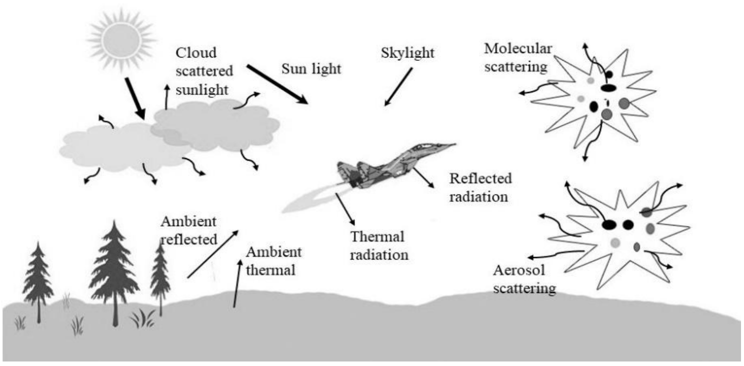


*Fig. 61. Radiation components in scene [115]*

A comprehensive scene simulation model for optoelectronic sensors operating within the 0.2–20 µm spectral range is described in [115]. The radiative components incorporated in this model (see Fig. 61) include:

- Direct solar radiation, solar radiation scattered by clouds, thermal background radiation, and skylight.
- Reflected ambient radiation and environmental thermal emission.

- Atmospheric thermal emission and sunlight scattered by atmospheric molecules and aerosols.
- Target's thermal emission and reflected radiation from the target (including sunlight, skylight, and ambient light).

Visibility is limited by the composition of the atmosphere, as well as the characteristics of aerosol particles, clouds, and water vapor. Assume that a UV- absorbing target is positioned in front of the atmospheric background (EB) at a distance *R* from the observer. This target completely absorbs UV radiation and is too cold to emit UV radiation, thus neither reflecting nor emitting any UV.

At short distances, the observer sees the target as a black object. As the distance between the target and the observer increases, UV radiation is increasingly scattered into the observer's field of view, reducing the contrast between the target and the background. The farther the distance, the stronger the scattered light becomes, and at a certain distance, the observer can barely distinguish the target from the background radiation.

Visibility is limited not only by atmospheric composition but also by the properties of aerosol particles, clouds, and water vapor. We assume a non-emitting UV target is placed in front of a background at a distance *R* from the observer (Figure 62), that is searching for objects against the background.

(a) (b) (c)

*Fig. 62. The visibility of the target depends on the distance between the target and the observer*

*(a) R=0.5km, $C_{neg}$=0.8; (b) R=1.5km, $C_{neg}$=0.6; (c) R=4.5km, $C_{neg}$=0.22*

### 8.2.2. Negative contrast

The target completely absorbs UV radiation and is too cold to emit any UV radiation; therefore, there is no reflection or emission from the target. At close range, the observer perceives the target as black. As the distance between the target and the observer increases, UV radiation is scattered into the observer's field of view, reducing the contrast between the target and the background. The farther the distance, the stronger the scattered light becomes, and at a certain distance, the observer can hardly distinguish the target from the background.

The Weber contrast C between the target and the background is defined as [116]:

$$C = \frac{E_T - E_B}{E_B} \quad (47)$$

where:

$E_B$ - the background radiance,

$E_T$ - the path radiance between a target and a sensor.

The negative contrast $C_{neg}$ is equal to ( $C_{neg} = -C$ ) :

$$C_{neg} = \frac{E_B - E_T}{E_B} \quad (48)$$

In this study, the PcModWin software (based on the MODTRAN code) was used to investigate various observation conditions. The model for calculating negative contrast was defined as follows:

- Geographic locations:
  –Warsaw (Poland), with latitude and longitude coordinates of 52.2°N, 21.0°E
  – Hanoi (Vietnam), with latitude and longitude coordinates of 21.0°N, 105.8°E
- Atmospheric models: Mid-Latitude Winter (MLW) and Mid-Latitude Summer (MLS) for Warsaw, and a Tropical atmospheric model for Hanoi

- Aerosol is a major cause of reduced visibility in the atmosphere. Therefore, in the survey, we conducted simulations for four different aerosol models, which are rural with 23km visibility, rural with 5km visibility, urban with 5km visibility, and urban with 2 km visibility.

- Radiance is calculated on summer and winter solstice, at noon

- The sensor observes along an oblique path, with the zenith angle depending on the position of the airborne platform.

Figure 63 illustrates the calculated radiance from the observer to the target as a function of distance R and under different atmospheric (aerosol) conditions.

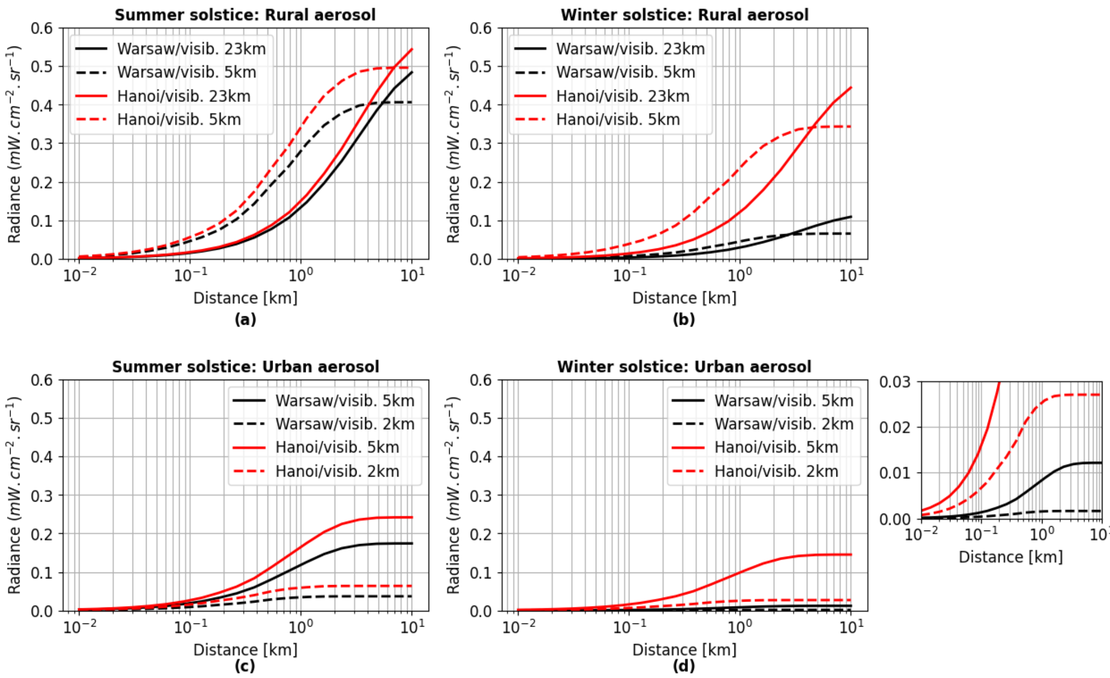


*Fig. 63. Path UV (300-400nm) radiance in Warsaw and Hanoi (ground situated observer), rural aerosol with 23km and 5km visibility on summer (a) and winter (b) solstice, urban aerosol with 5km and 2km visibility on summer (c) and winter (d) solstice.*

Next, Weber's contrast between the target and the background is calculated according to formula (45). The results are shown in Figure 65.

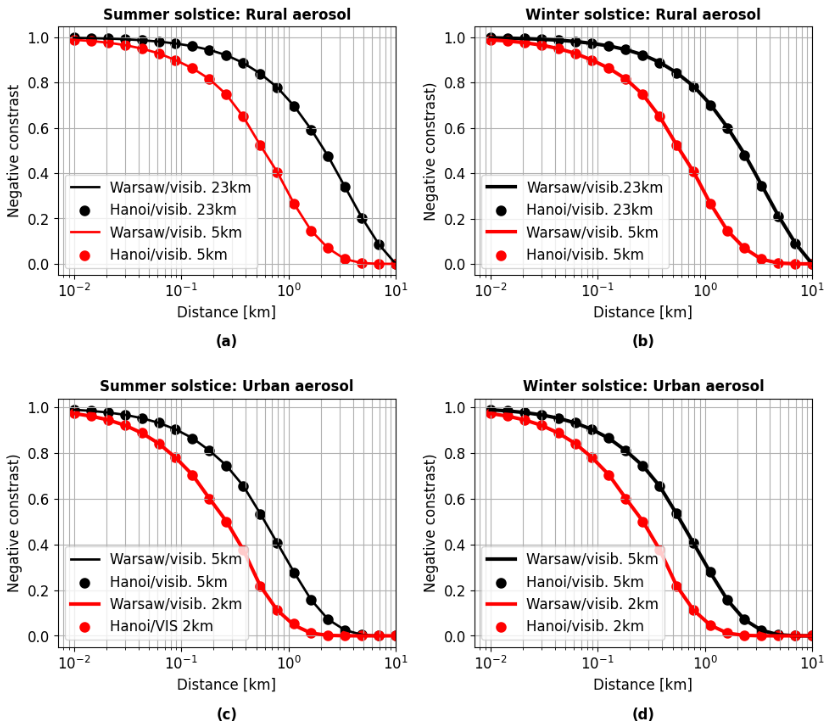


*Fig. 64. Negative contrast versus range, rural aerosol with 23km and 5km visibility on summer (a) and winter (b) solstice, urban aerosol with 5km and 2km visibility on summer (c) and winter (d) solstice.*

It is noticeable that the contrast curves are almost the same and overlap for Hanoi and Warsaw (Fig. 65) despite much higher UV insolation in Hanoi than in Warsaw (Fig. 64). Both background radiance $E_B$ and path radiance $E_T$ between the target, and the observer result from the scattered sunlight. Therefore, they are proportional to solar irradiance, so the level of solar irradiance does not change the resulting contrast despite it influences detection capability as the difference between background and path radiances is proportional to this level. Moreover, it is shown that for rural and urban aerosols, the calculated UV contrast depends almost only on meteorological visibility, which is determined by aerosol scattering, aerosol absorption, and molecular scattering. In contrast to the case of near UV radiance (Fig.65), for the above two types of aerosols (rural and urban) with the same 5 km visibility, there is little difference in the calculated UV negative contrasts.

### 8.3. Further Comparison calculation with Measured Data in the UV Band

The ability to accurately simulate background solar radiation plays a crucial role in understanding the operation of missile systems equipped with ultraviolet (UV) surveillance channels. Theoretically, the UV channel of such systems detects the silhouette of the target, which is formed due to the "negative contrast" against the UV background radiation. Therefore, variations in the level of background UV radiation can directly affect the performance of UV-guided missile systems.

In this study, we compare the negative contrast values calculated using the MODTRAN code with those measured in the field within the UV spectral range (300–400 nm), using Silicon Amplified Photodetectors with Fixed Gain manufactured by Thorlabs.

The technical specifications of the Si photodetector, as provided by the manufacturer, are listed in Table 13.

Table 13. Electrical Specifications

| | | |
|---|---|---|
| Detector | - | Si |
| Active Area | - | $\phi$1 mm (0.8 mm$^2$) |
| Wavelength Range | $\lambda$ | 200 to 1100 nm |
| Peak Wavelength | $\lambda_p$ | 730 nm (Typ) |
| Peak response | $\Re(\lambda_p)$ | 0.44 A/W (Typ) |
| Small signal Bandwidth | - | 150 MHz |
| NEP ($\lambda_p$) | $W/\sqrt{Hz}$ | 5 x $10^{-14}$ |
| Output current | Iout | 0 to 10 mA |
| Dark current | - | 0.3 nA (Typ.)<br>2.5 nA (Max) |

The measurement station consists of the following components:

- Detector: Silicon Amplified Photodetector – DET10A2
- Objective lens with an integrated UV bandpass filter (300–400 nm)
- Telescope lens
- Observation camera
- Oscilloscope
- Computer

In this experiment, we utilized available environmental conditions by measuring UV radiation blocked by buildings and comparing it to the background UV radiation in unobstructed areas. This was observed through a telescope equipped with a rear-mounted observation camera. The detector was aligned parallel to the observation lens. An oscilloscope was used to measure the output voltage of the detector. Measurements were conducted for targets positioned at varying distances behind the foreground objects.

*Fig. 65. Measuring device: Si Photodiode with a UV filter (upper) with visible sight camera (lower)*

Table 14. Presents the calculated negative contrast based on the signal received from the photodetector in the UV spectral range

| Distance to object [m] | Signal [mV] | Background [mV] | Contrast (%) |
|---|---|---|---|
| 50 | 2.5 | 19.3 | 87.05 |
| 100 | 3.3 | 20.8 | 84.13 |
| 150 | 4.2 | 22.4 | 81.25 |
| 400 | 8.6 | 19.1 | 54.97 |
| 520 | 10.1 | 19.2 | 47.4 |
| 1000 | 13.8 | 19.3 | 28.5 |

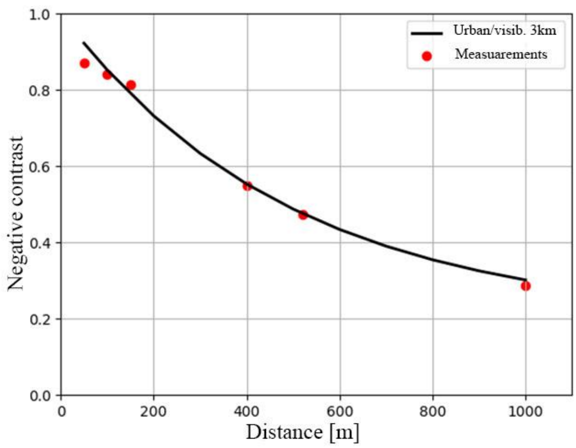


*Fig. 66. The measured (red points) and calculated (black curve) negative contrast*

The calculations were compared with some measurements of negative contrast given by a few buildings in Warsaw located at various distances. The contrast was measured with Thorlabs DET10A2 Si Detector with Schott UG11 UV filter (as shown in Fig. 66). Measurements were performed on a partly cloudy summer day at 10 a.m. Calculations of contrast for summer model of the atmosphere with urban aerosols and 3 km visibility show good agreement with the results of measurements (Fig. 66).

## 8.4. Range analysis of aircraft detection using negative contrast

### 8.4.1. Signal-to-noise ratio in UV

The target detection range can be determined based on signal-to-noise ratio (SNR). In general, the performance limit of a photon detector depends on photon noise, which appears as a random voltage or current at the detector's output terminals. The total noise from the detector is the root mean square (rms) sum of the detector's intrinsic noise plus the photon noise [117].

$$SNR = \frac{\gamma(\Phi_b - \Phi_{ts})}{\sqrt{\frac{1}{\eta}\left((1-\gamma)\Phi_b + \gamma\Phi_{ts}\right)\frac{hc}{\tau\lambda} + NEP^2}} \tag{49}$$

$\Phi_{ts}$ and $\Phi_b$ are the radiant flux from the target silhouette area and from the background at a pixel, η is the quantum efficiency of the detector, h is Planck's constant, c is the speed of light in vacuum, τ is the integration time of image acquisition, λ is the central wavelength, NEP is the equivalent power of the readout and dark current noise of the pixel. The γ coefficient depends on the ratio of the solid angles of the target silhouette ($\Omega_{ts}$) and the single pixel ($\Omega_p$)

$$\gamma = \begin{cases} \Omega_{ts} / \Omega_p & \text{if } \Omega_{ts} \le \Omega_p \\ 1 & \text{otherwise} \end{cases} \tag{50}$$

The SNR was calculated for an observation device (UV sensor) with the following parameters: spectral band 300-400 nm, pixel size 15x15 μm, quantum efficiency η=0.5, integration time τ equal to 20ms (bandwidth 25Hz), specific detectivity $D^*=5\cdot 10^{10}$ $cm\cdot Hz^{1/2}\cdot W^{-1}$ (that corresponds to NEP of $1.5\cdot 10^{-13}$W). The parameters of the objective lens are 50mm focal length F, 20mm aperture diameter D (F/2.5, NA=0.196) and optics transmission $T_{opt}$ = 90%.

The radiant flux $\Phi_{ts}$ or $\Phi_b$ on a single pixel of the array is gathered from optics aperture ($\pi D^2/4$) and pixel's field of view (solid angle $A_p/F^2$) and are equal to [118]:

$$\Phi_{b/ts} = T_{opt} E_{b/ts} \frac{\pi D^2}{4} \frac{A_p}{F^2} = T_{opt} E_{b/ts}\, \pi N A^2 A_p \quad (51)$$

where $L_{b/s}$ is radiance from a target silhouette or background and $A_p$ is a pixel area. The radiances were calculated using PcModWin for the noon on the spring equinox, cloudless sky, rural aerosols of visibilities 23km and 5km, and urban aerosols of visibilities 5km and 2km.

The calculations were performed for a target of 20m$^2$ area and flying at 1km altitude.

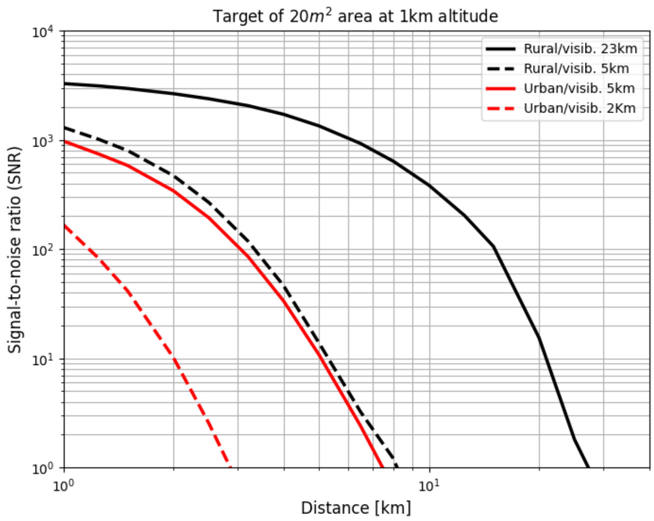


*Fig. 67. SNR as a function of distance of various visibilities*

It can be noticed that the SNRs (and therefore detection ranges) for the defined target and sensor depend mostly on visibility and only slightly on the type of aerosol. For the same visibility equal to 5 km and two aerosol models, the calculated SNRs are very similar. It also results from the above diagram (Figure 67) that the range of detection for the selected device is close to ranges of atmospheric visibilities, as scattering is dominant in both the UV and VIS bands.

### 8.4.2. Range Analysis of aircraft detection

It results from the above diagrams (Fig. 67) that the range of detection for the selected device is close to ranges of atmosphere visibilities as scattering is dominating in both UV and VIS bands.

The general model for UV signatures of airborne objects includes many factors: radiation from the target, background, solar path radiation, and others. However, only the solar path radiation plays a major role in the total radiance at the sensor. The remaining components of the UV signature are insignificant.

The airborne target blocks the radiation path behind it resulting in negative contrast. Calculating the negative contrast for various environmental conditions is important for the prediction of detection, recognition and/or identification range of optoelectronic devices.

Comparing simulation results under different conditions, it has been found that:

- background radiation depends mainly on the level of isolation i.e., the elevation of the Sun, cloudiness, aerosol density and characteristics, etc.
- The negative contrast of airborne targets does not depend on the level of insulation but only on visibility (cloudiness, aerosol density and characteristics, etc.)
- contribution of thermal emission to UV signatures of airborne targets is negligible
- as direct sunlight is much higher than scattered one sunlight blinks (sunlight reflected by the target) may significantly disturb the process of detection
- negative contrast has a value close to the transmittance of the atmosphere
- typical ranges of airborne target detection for UV observation devices are close to those for VIS ones.

## 9. Range analysis of detection of UV radiation emitted by rocket plumes

The threat posed by low-altitude, passive infrared-homing surface-to-air missiles (man-portable passive infrared-homing surface-to-air missiles, MANPADS) has driven the development of passive missile warning sensors. These sensors are used to trigger an alarm when an aircraft is attacked by a missile. Passive missile warning sensors typically employ wide–field-of-view ultraviolet or infrared detectors to detect radiation emitted by a missile plume.

The middle-ultraviolet region is particularly important because the sky background observed from low altitudes is almost signal-free, enabling detection of plume radiation. The plume itself is a near-axisymmetric medium in which non-equilibrium emission processes of gas molecules occur, while metal-oxide particles within the plume emit, absorb, and scatter the radiation field. In the infrared, molecular vibrational bands and thermal emission from particles are the dominant emission sources; in the ultraviolet, chemiluminescence becomes the primary emission mechanism.

The signature of energy radiated by rocket-engine plumes and emitted into space is widely used in military applications such as missile launch early-warning systems. Compared with infrared detection systems, ultraviolet detection offers advantages including strong real-time capability and a less cluttered environmental background. Therefore, analyzing the detection range of UV radiation emitted by plumes is meaningful and has substantial practical value for developing early countermeasures against missile launches to reduce potential damage.

A Missile Warning System (MWS) is a passive defensive warning system designed to detect, track, and warn of missile threats approaching a protected platform.

MWS operates in a portion of the UV spectrum known as the “solar-blind” band (250–280 nm). In this band, the only significant natural illuminant, the Sun is almost completely absorbed by stratospheric ozone. The remaining sunlight is scattered, producing an almost uniform sky background. In addition, background objects are typically too cold to emit any appreciable UV radiation. Consequently, at low altitudes, UV sensors operating in the solar-blind band are subject to relatively little background-radiation interference. In such an environment, even very weak UV sources can be readily detected. The only significant radiation sources received by a solar-blind UV detector include natural high-energy radiation sources (fires and explosions), artificial non-threat sources (industrial and urban high-temperature emitters), and rocket plumes from ground-to-air and air-to-air missiles (surface-to-air and air-to-air). However, choosing the solar-blind band also introduces challenges: even at low altitudes, atmospheric transmission in the solar-blind region is considerably poorer than in the visible or IR bands. Ozone in the solar-blind region strongly scatters the emitted energy from the source. Therefore, this chapter focuses on analyzing UV radiation from rocket plumes and on how background radiation and atmospheric attenuation affect the ability to detect plumes.

### 9.1. Radiation sources

The calculation of the plume signal is carried out in two steps. First, the thermochemical and gas-dynamic properties of the plume are determined by solving the flow-field equations using computational fluid dynamics (CFD). Then, the radiative transfer equation is integrated to obtain radiation maps or the angular dependence of plume intensity.

Most solid-propellant missiles contain aluminium particles added to the propellant to achieve high specific impulse, which results in the formation of micro-sized alumina particles in the plume. Afterburning of intermediate products such as $H_2$ and CO with entrained air increases the temperature and generates free radicals such as O and OH. These radicals produce ultraviolet emission through chemiluminescent reactions.

The greatest difficulty in solving the RTE lies in describing the in-scattering term, i.e., the portion of radiation scattered by particles from all directions into the line of sight. Over the past three decades, many methods have been proposed to solve the RTE in media with scattering and absorption; the main differences among these methods lie in how scattering is represented.

Numerous researchers have conducted extensive studies on the UV radiation characteristics of missile plumes. Representative approaches include using SHDOM to simulate and calculate the UV radiation characteristics of the CO+O reaction in missile plumes[119]; employing the discrete ordinate method to study the UV radiation characteristics of CO+O and alumina particles in two-phase missile plumes; and applying direct Monte Carlo methods to simulate the UV radiation characteristics of OH in spacecraft plumes [120]. References [121] investigated the effects of OH and soot on the UV radiation characteristics of Supersonic Rocket Plume. Reference [122] proposed a model to predict the UV spectral characteristics of missile plumes and to calculate radiation generated by CO+O and alumina particles in the plume. Reference [123] performed a quantitative analysis of the UV spectral radiation of CO, $CO_2$, NO, HCl and soot particles in missile plumes using a band-model code combined with experimental measurements.

From these studies, it can be concluded that the UV signature of a missile plume mainly originates from CO+O chemiluminescence and radiation from hot $Al_2O_3$ particles, with prominent emission in the 250–290 nm (solar-blind UV) region. The intensity depends on factors such as propellant composition, engine design, altitude, and ozone concentration. However, these studies primarily focus on simulating influencing factors and do not provide results for the detailed spectral characteristics of the plume within the narrow 250–290 nm band. Consequently, there is a lack of data for performing detection-capability assessments of plume signatures.

Chemiluminescence from the recombination reaction between carbon monoxide (CO) and atomic oxygen (O) is a phenomenon commonly observed in flames and has been identified as the dominant source of ultraviolet (UV) emission in aluminum-containing missile plumes at low altitudes. The emitting reaction is [28]:

$$\mathrm{CO} + \mathrm{O} \rightarrow \mathrm{CO}_2^* \rightarrow \mathrm{CO}_2 + h\nu$$

produces UV photons, and its emission intensity follows a proportional relationship.

$$I \propto [\mathrm{CO}][\mathrm{O}],$$

demonstrating that the emission process depends directly on the concentrations of CO and O in the plume. In shock-tube experiments, Grillo and Slack measured low–spectral-resolution distributions of CO + O emission heated to 1300–2700 K.

The results of Grillo and Slack show that the CO + O emission spectrum is relatively smooth in the 250–300 nm wavelength range, consistent with the characteristics of a continuous emission band (continuum) originating from the excited $CO_2$ state. This is particularly important for modeling the UV radiation of missile plumes, since this wavelength range lies within the solar-blind region, where UV sensors can operate without interference from atmospheric background radiation or reflected sunlight. The dependence of the emission intensity on the product of concentrations [CO][O] also implies that chemical processes in the nozzle exit region and during the initial expansion stage of the plume have a direct impact on the strength of the UV signal.

In plumes from aluminized solid-propellant engines, the CO + O reaction becomes especially important because atomic oxygen is generated through thermal dissociation of $CO_2$ and through oxygen–hydrocarbon reaction chains. As the plume interacts with the surrounding air, the concentration of O increases due to recombination and late-stage oxidation (afterburning), further enhancing chemiluminescence intensity in the outer regions of the plume. This mechanism explains why aluminized propellant missiles operating at low altitudes exhibit strong UV signatures that can be detected at long ranges.

From a modeling perspective, the data of Grillo and Slack provide a basis for constructing a temperature-dependent spectral emission function $J_{\text{chem}}(\lambda, T)$, which is often implemented in plume models in the form of a coefficient $K_\lambda(T)$. When combined with the spatial distributions of CO and O concentrations obtained from flow-field simulations, this function enables accurate calculation of the volumetric emission rate according to:

$$J_{\text{chem}}(\lambda, x, r) = K_\lambda\big(T(x,r)\big)\,[CO](x,r)\,[O](x,r) \tag{52}$$

where:

- $J_{\text{chem}}$: UV emission rate at wavelength $\lambda$($W\cdot m^{-3}\cdot sr^{-1}\cdot nm^{-1}$)
- $[CO]$, $[O]$: concentrations of CO and O at position $(x|r)$
- $K_\lambda(T)$: specific emission coefficient, dependent on wavelength $\lambda$ and temperature $T$

In aluminized solid-propellant engines, aluminum is an important additive used to enhance propulsion efficiency, but it also gives rise to a distinctive radiation structure in the missile plume. When aluminum burns in the combustion chamber, intense oxidation reactions produce liquid alumina ($Al_2O_3$) droplets at very high temperatures, typically ranging from about 2500 to over 3000 K. These alumina droplets are carried by the expanding flow and exit the nozzle as hot particles with strong radiative emission. During expansion into the ambient atmosphere, alumina cools rapidly and may solidify into different crystalline phases, primarily $\gamma$-$Al_2O_3$ or the more stable $\alpha$-$Al_2O_3$. According to Anfimov et al. [124], the $\gamma$ phase forms under high cooling rates and exhibits stronger absorption and emission in the ultraviolet region due to the characteristics of its fundamental absorption edge. This mechanism contributes significantly to the enhancement of the plume's UV brightness.

The size of alumina particles in the plume is observed to be highly diverse and often exhibits a multimodal distribution, with larger modes around approximately 20 µm and smaller modes below 2 µm. Nevertheless, in radiation simulations, a unimodal log-normal distribution is commonly adopted to ensure computational feasibility while still capturing the dominant optical trends of the system. The actual particle shapes in the plume are very difficult to measure; therefore, many models assume spherical particles and employ Mie theory to simulate their optical properties. For particle sizes in the micrometer range and short UV wavelengths (≈ 250–290 nm), the Mie size parameter of alumina particles becomes very large, resulting in strong forward-peaked scattering.

In addition to their scattering role, alumina particles are also an important source of thermal emission because they retain high temperatures from the combustion chamber. The radiation emitted by alumina does not follow a purely Planckian distribution but is strongly influenced by absorption coefficients that depend on the crystalline phase and impurities, as described by Anfimov et al. in their optical model for solid alumina.

Aluminum also indirectly influences the UV brightness of the plume through chemical reactions in the afterburning region. The ability of alumina droplets to maintain high temperatures creates favorable conditions for reactions such as CO + O and $H_2$ + O to proceed more vigorously, leading to a significant increase in the concentrations of O and OH radicals. These species are key precursors for CO + O chemiluminescence, which is the dominant radiation source in the solar-blind region. Therefore, the presence of aluminum not only generates radiation directly through alumina particles themselves but also enhances gas-phase emission mechanisms, making the UV signature of aluminized plumes several times stronger than that of non-aluminized plumes.

According to Kirchhoff's law, the spectral emissivity of an alumina particle is equal to its spectral absorptivity. Consequently, the volumetric thermal emission rate at each point in the plume can be expressed as:

$$J_{\text{part}}(\lambda, x, r) = \frac{k_{\text{abs}}(\lambda, x, r)}{4\pi} B_\lambda\big(T(x, r)\big), \tag{53}$$

where $B_\lambda(T)$is the Planck function describing blackbody radiation at temperature (T), while the volumetric absorption coefficient $k_{\text{abs}}(\lambda)$is determined from Mie theory combined with the complex refractive index of alumina as given by Anfimov.

According to Mie theory, the absorption coefficient of a particle ensemble can be written as:

$$k_{\text{abs}}(\lambda, x, r) = N_p(x, r)\, \pi a^2\, Q_{\text{abs}}(\lambda, a) \tag{54}$$

where $N_p(x, r)$is the number density of alumina particles at a given point in the plume, $a$is the characteristic particle radius, and $Q_{\text{abs}}$is the Mie absorption efficiency, which depends on the complex refractive index $(n|k)$of alumina.

In many practical cases, the alumina particle size distribution is described by a log-normal distribution. In that case, the absorption coefficient is obtained as a weighted average integral over the entire range of particle radii present in the size distribution.

At each plume grid cell, the total spectral emission rate of the gas–particle medium is formed by two mechanisms: chemical emission and particle thermal emission. Therefore:

$$J_{\text{tot}}(\lambda, x, r) = J_{\text{chem}}(\lambda, x, r) + J_{\text{part}}(\lambda, x, r). \quad (55)$$

These are the two intrinsic emission sources before being affected by radiative transfer through the medium. To determine the radiation observed along an arbitrary viewing direction, the radiative transfer equation must be integrated along the line of sight (LOS).

Determining the input parameters for calculating the UV radiation of a missile plume is relatively complex. For this study, which focuses on assessing the influence of background radiation on missile plume detection, the data are specified as follows:

- Assume the plume is confined within a cylinder of dimensions equal to 0.07× 1 m. The domain is discretized into a 200 × 600 grid (cells).

- $K_\lambda(T)$: the specific emission coefficient, dependent on wavelength $\lambda$and temperature $T$

The concentrations $[CO]$and $[O]$are calculated using CFD in ANSYS Fluent with the following nozzle parameters: a small solid-propellant rocket motor with a diameter of 0.07 m and a length of approximately 1 m is positioned near the ground. The engine nozzle has a circular cross-section, with an expansion ratio and a nozzle half-angle of 7.5°. The plume downstream of the nozzle is assumed to be axisymmetric and operate under steady-state conditions [125]. Boundary conditions based on the nozzle-exit plane parameters are given in Table 15 [9].

Table 15. Parameters for plume structure of Propellant composition of HTTB–AP–Al

| | |
|---|---|
| exit radius [mm] | 11.5 |
| Axial velocity [m/s] | 2404.6 |
| Radial velocity [m/s] | 356.7 |
| Exit pressure [kPa] | 200.4 |
| Exit temperature [K] | 2327.2 |
| Exit plane mole fractions | |
| CO | $2.106\times10^{-1}$ |
| H2O | $1.368\times10^{-1}$ |
| CO2 | $1.713\times10^{-2}$ |
| H2 | $2.985\times10^{-1}$ |

| | |
|---|---|
| OH | $3.210\times10^{-4}$ |
| O2 | $1.000\times10^{-6}$ |
| O | $3.000\times10^{-6}$ |
| N2 | 0.336645 |

To simplify the calculation process, only a subset of photochemical reactions is considered, as listed in Table 16.

Table 16. Reaction mechanism [125]

| Reactions | Reaction rates |
|---|---|
| O +O +M → O2 +M | $k = 1.09\times10^{14}\ \exp(7.48/RT)$ |
| CO +O +M → CO2 +M | $k = 2.54 * 10^{15}\ \exp(\ 18.29/RT)$ |
| OH +H2 → H2O +H | $k = 1.14 * 10^{9}\ T^{1.3}\exp(\ 15.17/RT)$ |
| O +H2 → OH +H | $k = 1.81 * 10^{10}\ T\ \exp(\ 37.25/RT)$ |
| H +O2 → OH +O | $k = 1.45 * 10^{14}\ \exp(\ 68.59/RT)$ |
| CO +OH → CO2 +H | $k = 1.69 * 10^{7}\ T^{1.3}\ \exp(2.74/RT)$ |
| OH +OH → H2O +O | $k = 6.02 * 10^{12}\ \exp(4.57/RT)$ |
| CO +O2 → CO2 +O | $k = 2.53 * 10^{12}\ \exp(\ 199.54/RT)$ |

Figure 68 shows the distribution of the mole fraction of CO (Figure 68.a) and O (Figure 68.b) in the plume at a side-on viewing cross-section in the OXY plane passing through the plume center

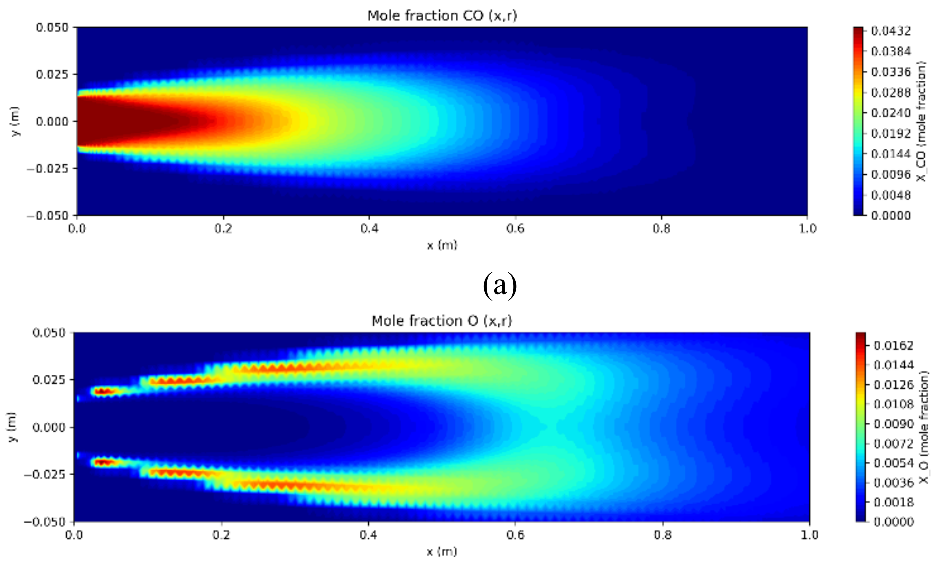

(a)

(b)

*Fig. 68. Mole fraction of CO and O in the plume.*

*a) Mole fraction of CO; b) Mole fraction of O*

Assume that the Worster model is used to represent the $Al_2O_3$ particle size distribution. This model uses the following parameters for the particle size distribution in the plume:

$$\frac{dN}{dD} = fAe^{-AD} \tag{56}$$

where:

$D$ is the particle diameter (μm),

$\frac{dN}{dD}$ is the particle number density per unit diameter,

$A$ is the slope parameter of the distribution ($\mu m^{-1}$),

$f$ is the normalization constant.

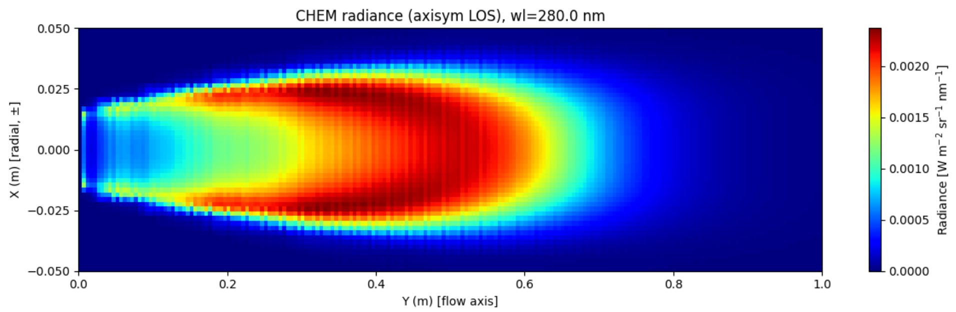


(a)

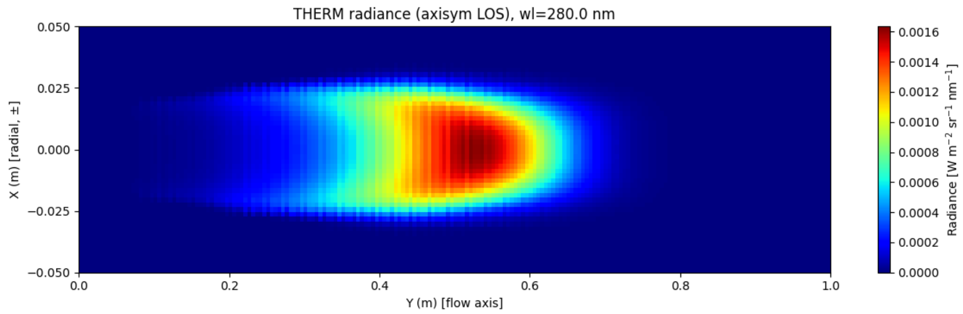


(b)

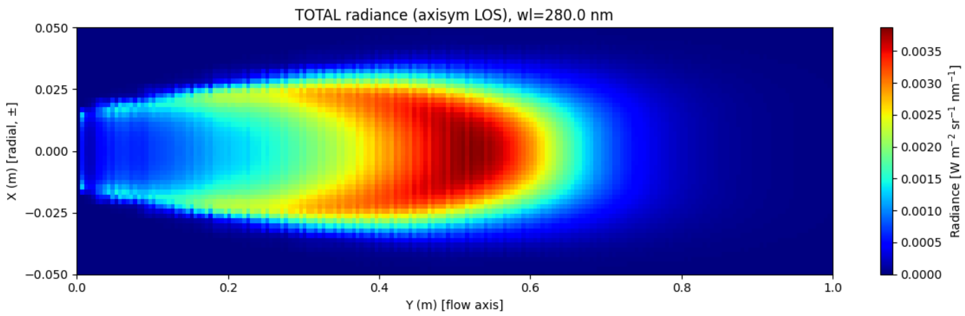


(c)

*Fig. 69. Plume radiation at a wavelength of 280 nm*

*a) Chemiluminescent emission; b) Thermal emission from aluminum particles; c) Total emission*

The normalization factor is calculated as:

$$f = \frac{N_{tot}}{e^{-AD_{min}} - e^{-AD_{max}}} \tag{57}$$

where:

$N_{tot}$ is the total particle number density per unit volume,

$D_{min}$ and $D_{max}$ are the minimum and maximum particle diameters.

In the present calculations, the following parameters are used: $A = 1$, $N_{tot} = 2.96 \times 10^6\ /cm^{-3}$. The particle diameters range from 0.1 µm to 100 µm.

Based on the above assumptions, the calculated plume radiation at a wavelength of 280 nm is shown in Figure 69. The plume radiation includes chemiluminescence (Fig.69a), thermal emission from particles (Fig.69b), and the total emitted radiation (Fig.69c).

Although each grid cell within the plume has an emission spectrum with a different intensity, to evaluate plume detectability in the solar-blind UV region it is assumed that the spectral distribution is uniform, and the value is taken as the average over the entire plume. Figure 70 shows the plume's mean emission spectrum for the side-on viewing direction in the 250–295 nm spectral range.

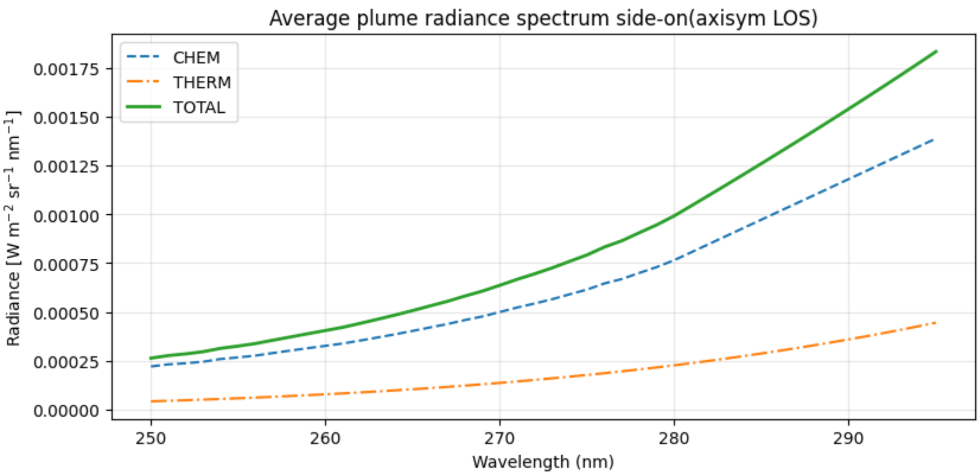


*Fig. 70. Average plume emission spectrum along the side-on direction*

Comparison with the results reported by Neele F. *et al.* [9] shows that the calculated radiation intensity at a wavelength of 280 nm for the side-on viewing geometry is comparable and is approximately 1 mW/sr/nm. A slight difference is observed, which can be attributed to the assumptions regarding the size distribution and number density of $Al_2O_3$ particles.

## 9.2. Attenuation of the plume UV signature in the atmosphere

Ultraviolet radiation in the solar-blind region experiences significant attenuation when propagating through the Earth's atmosphere, primarily due to ozone absorption and scattering by atmospheric aerosols.

In this study, MODTRAN is employed to calculate atmospheric transmittance as a function of propagating distance under different aerosol models.

The selected atmospheric model is Mid-Latitude Summer, with the calculation location set to Warsaw. The considered aerosol models include Rural with visibilities of 23 km and 5 km, and Urban with visibilities of 5 km and 2 km.

The selected spectral range is 250–295 nm.

The calculated attenuation of UV radiation emitted from missile plumes under different aerosol conditions as a function of propagation distance is presented below. These results are also compared with the experimentally measured background radiance.

The sensor is assumed to be located on the Earth's surface, observing the target as shown in Figure 71

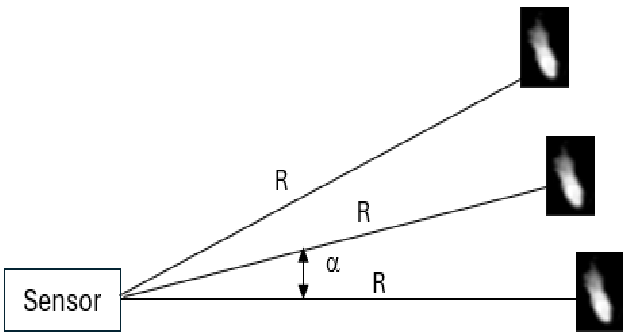


*Fig. 71. Sensor on the ground*

In the case where the sensor is located on the Earth's surface, changes in range and elevation angle significantly affect the attenuation of radiation from the rocket plume. Figure 72 shows the atmospheric attenuation coefficient for horizontal observation and elevation angles of 30° and 60° at 1 km.

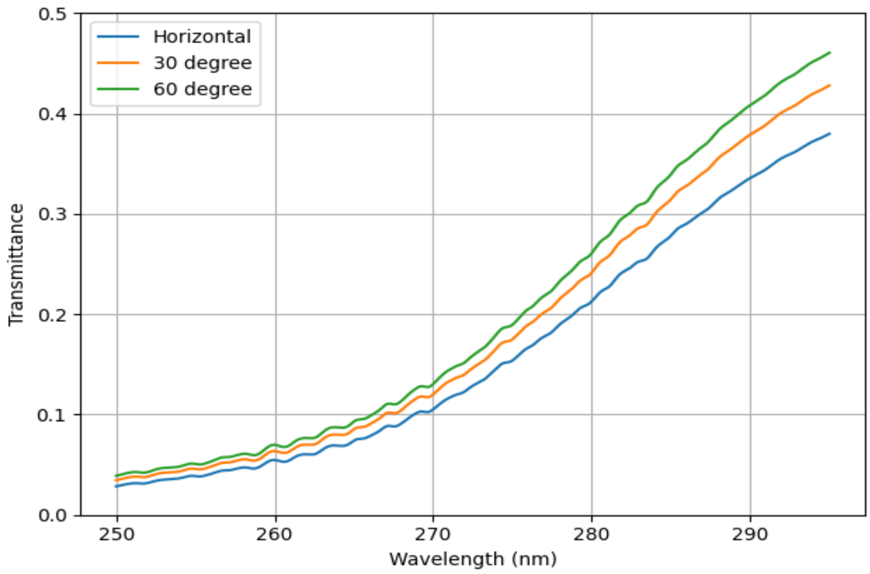


*Fig. 72. Spectral atmospheric transmittance (1km)*

It is evident that changes in the sensor elevation angle significantly affect atmospheric transmittance. Within the elevation angle range of 0°–90°, higher elevation angles result in increased atmospheric transmittance, especially in the 250–295 nm UV band.

Figure 73 compares the attenuated rocket-plume radiation with experimentally measured background radiation for horizontal (a), 30° (b), and 60° (c) lines of sight. Atmospheric attenuation and aerosol effects corresponding to Rural 23 km conditions (good visibility) near the ground are included in the calculations.

The radiance of the target observed at the sensor location is typically attenuated by atmospheric absorption and scattering. If we denote:

- $L_{s,0}(\lambda)$: the "intrinsic" (unattenuated) spectral radiance of the target at the target surface,
- $\tau(\lambda)$: the atmospheric transmittance along the target–sensor line of sight,

then the target radiance reaching the optical system can be approximated as:

$$L_s(\lambda) = \tau(\lambda)\, L_{s,0}(\lambda) \tag{56}$$

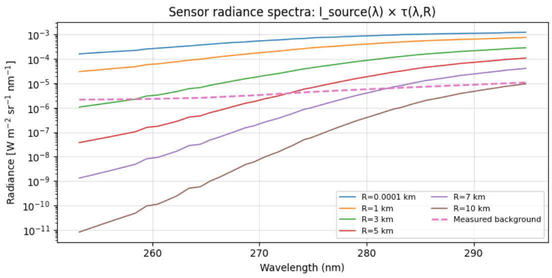


(a)

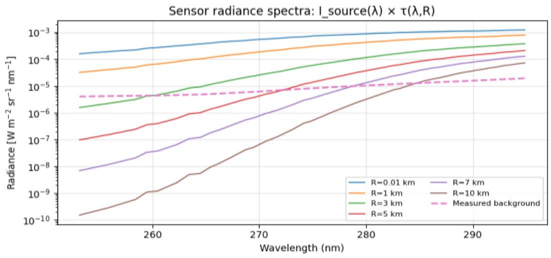


(b)

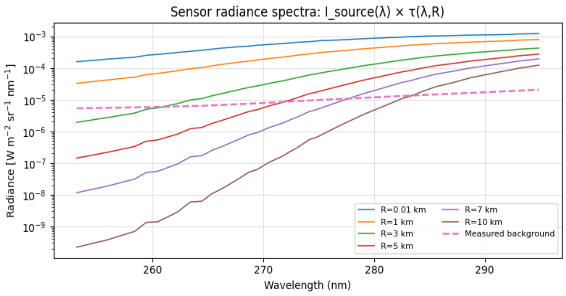


(c)

*Fig. 73. Spectral radiance received at the sensor for different elevation angles: (a) horizontal observation, (b) elevation angle of 30°, and (c) elevation angle of 60°.*

An increase in the sensor elevation angle enhances atmospheric propagation, thereby increasing the radiative flux received from the target, with the effect being particularly pronounced at shorter wavelengths. As shown in Figure 73, at a range of 5 km, the background radiance exceeds that of the target at wavelengths shorter than 280 nm.

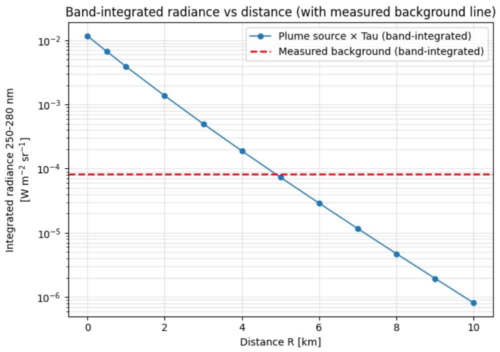


(a) Rural – 23km visibility

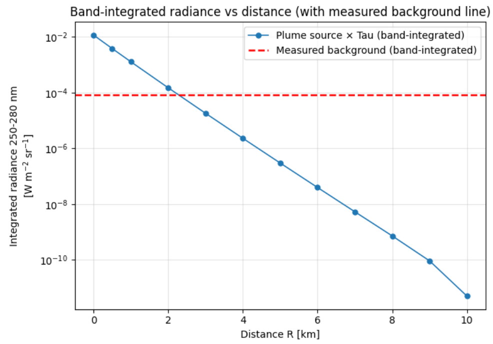


(b) Rural – 5km visibility

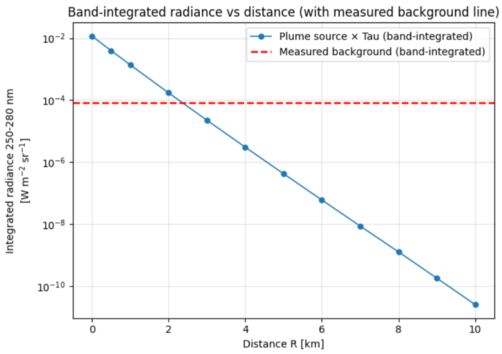


(c) Urban – 5km visibility

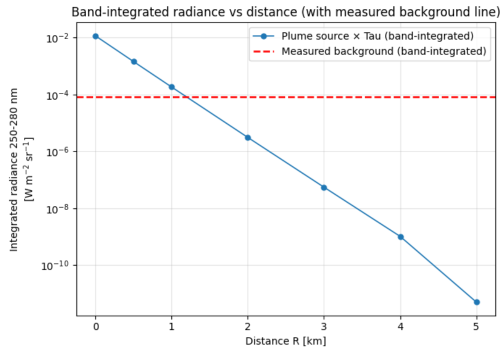


(d) Urban – 2km visibility

*Fig. 74. Spectrally integrated radiative flux over the 250–295 nm band for different aerosol conditions*

In the UV region, radiation is strongly attenuated due to scattering by aerosol particles. Figure 74 shows the integrated UV radiance in the 250–295 nm band at the sensor entrance aperture for different aerosol models, namely Rural and Urban. It can be observed that under reduced-visibility conditions caused by aerosol particles, the radiative flux is significantly attenuated.

### 9.3. UV Sensors in the Solar-Blind Region

UV sensors used in the ultraviolet spectral region are available in a wide variety of types, depending on the semiconductor material and the operating principle. Figure 75 illustrates the classification scheme of UV detectors.

Photomultiplier tubes or silicon-based photodetectors combined with UV bandpass filters are currently the only viable options for imaging in this critical spectral range. In missile approach warning (MAW) systems deployed on military aircraft, sensors are required to exhibit extremely high sensitivity in the solar-blind ultraviolet region; consequently, UV-sensitive photomultiplier tubes are still predominantly employed. The major drawbacks of PMT-based sensors are their bulky and complex structure, the requirement for high operating voltages, and the frequent need for additional optical filters to suppress out-of-band radiation [126].

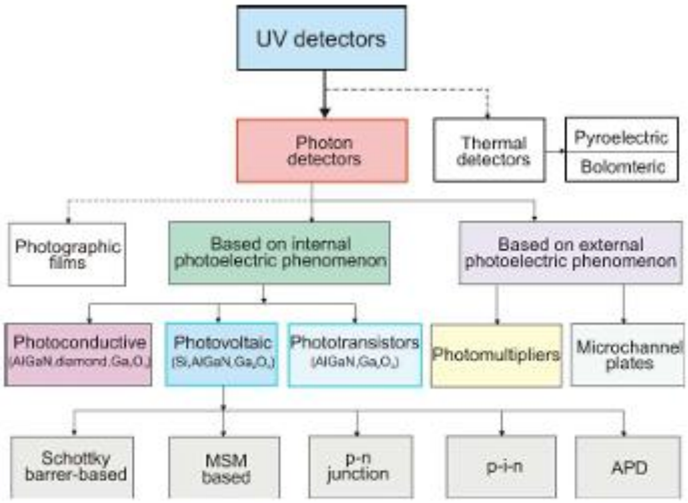


*Fig. 75. Classification of UV detectors [117]*

The development of III-nitride semiconductor materials, particularly $Al_xGa_{1-x}N$, has opened a fundamentally different approach for solar-blind UV sensors. Owing to the ability to tailor the bandgap by adjusting the aluminium composition, as well as through the design of the absorption layer structure and illumination configuration (front-illuminated or back-illuminated), AlGaN-based photodetectors offer intrinsic spectral selectivity. Experimental studies have demonstrated that back-illuminated AlGaN photodiodes can achieve very high quantum efficiency (QE) in the 250–280 nm range, with peak values reaching 80–89% at wavelengths around 275 nm, while simultaneously maintaining out-of-band rejection ratios exceeding $10^6$ without the use of additional optical filters [127], [128]. As a result, AlGaN photo detectors can exhibit intrinsic solar-blind characteristics. This indicates that eliminating optical filters is not only feasible but also provides significant advantages in terms of device performance, sensitivity, and operational stability.

Several recent studies have evaluated the feasibility of replacing PMTs with backside-illuminated AlGaN focal plane arrays. These devices consist of two-dimensional AlGaN detector arrays flip-chip bonded to a CMOS readout integrated circuit (ROIC) employing capacitive transimpedance amplification. The main advantages of such sensors include high quantum efficiency, radiation hardness, and fast temporal response. By adjusting the aluminum composition in the AlGaN alloy, the spectral response can be tailored without the need for optical filters, or with only minimal external filtering [129] .

At present, commercially available specifications for AlGaN-based focal plane array radiation sensors are not yet widely reported. Therefore, for the purpose of radiometric calculations, this study adopts a set of representative (assumed) sensor parameters based on previously published experimental and theoretical studies on AlGaN photodetectors [127], [128], [130] .

Table 17. Detector parameters

| **Parameters** | **Value** |
|---|---|
| FPA size | 320 × 256 |
| Pixel size | 27 µm × 27 µm |
| Peak λ | ~278 nm |
| EQE (PD) | 89–91% |
| Dark current | $<2\times10^{-9}$ A/cm² |
| Visible rejection | $>10^{6}$ |
| ROIC | FLIR ISC9809 |

The pixel quantum efficiency is illustrated in figure 10.

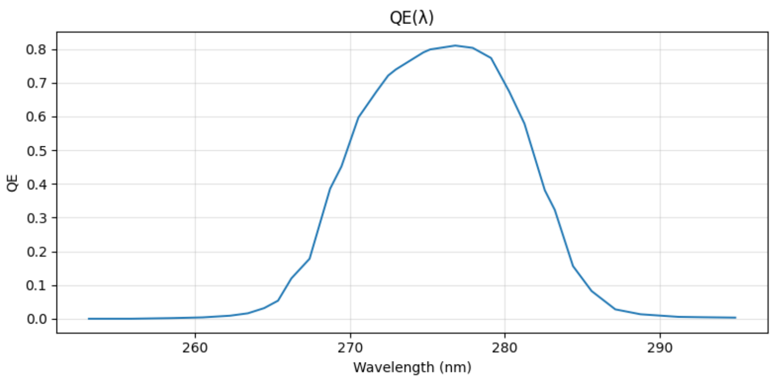


*Fig. 76. Spectral quantum efficiency of the UV detector [130]*

Backside-illuminated solar-blind $Al_xGa_{1-x}N$ photodiodes exhibit extremely low dark current, with a dark current density of at a reverse bias of 10 V. For a pixel area of approximately $A \approx 27 \times 27$ the dark current per pixel is on the order of $I_{dark} \lesssim 1.5 \times 10^{-14}$ . This indicates that the intrinsic noise of the photodiode is very small and does not limit the detector's sensitivity.

In focal plane array detectors, the dominant limitation on the signal-to-noise ratio does not originate from the photodiode itself but from the readout integrated circuit

(ROIC) noise. Previous studies report ROIC equivalent noise levels ranging from several tens to several hundreds of electrons RMS per pixel per frame, depending on the integration time and ROIC architecture. Consequently, in the SNR analysis of solar-blind AlGaN UV sensor systems, ROIC noise typically dominates the total noise budget, while the photodiode dark current noise can be neglected under room-temperature operating conditions.

### 9.4. Detection capability analysis using SNR

In electro-optical systems for detecting rocket plumes in the solar-blind ultraviolet band, the signal-to-noise ratio plays a central role in determining the detection capability and the discrimination of the target against the background. The SNR is directly related to the probability of detection $P_d$ and the probability of false alarm $P_{fa}$. Although background noise in the 250–290 nm band is often considered low, atmospheric scattering mechanisms, natural emission, and noise contributions from the optical system can still be significant. Therefore, a complete and accurate SNR model is required.

The parameters affecting the SNR include:

- UV sky radiance intensity.
- atmospheric structure (water vapor, ozone, aerosols).
- solar zenith angle.
- background reflectance (albedo).
- sensor–target range and observation geometry.
- optical transmittance of the imaging system and the detector quantum efficiency.
- integration time and electronic noise of the readout chain.

Once the target signal, atmospheric propagation (or transmittance), background noise, and related quantities are determined, these data are combined with the optical system parameters that can be used to convert the radiance at the entrance of the optical system into the spectral irradiance at the detector focal plane. After the radiation reaches the detector, it is converted into an electrical signal (photon-generated electrons) according to the detector's quantum efficiency.

The objective of this section is to develop an analytical model that describes the relationship between target radiance, background radiance, the field-of-view fill factor, and the electro-optical parameters, thereby deriving a complete SNR expression. The resulting model is then used to evaluate the detectability of rocket plumes through several representative examples.

The observed radiance at the sensor in the presence of a target is given by

$$L(\lambda) = \gamma L_s(\lambda) + (1-\gamma)L_{\mathrm{bg}}(\lambda) \tag{58}$$

where:

- $L_s(\lambda)$is the spectral radiance of the target at the entrance aperture of the optical system.
- $L_{\mathrm{bg}}(\lambda)$is the path background radiance, generated by the atmosphere and the surrounding environment.
- $\gamma$ is the fill factor, which represents the fraction of the pixel field of view (FOV) occupied by the target.

The fill factor is defined as the ratio between the solid angle subtended by the target and the solid angle of a pixel field of view:

$$\gamma = \begin{cases} \dfrac{\Omega_{target}}{\Omega_p}, & if\ \Omega_{target} \le \Omega_p \\ \quad 1 \quad , & otherwise \end{cases} \tag{59}$$

where:

- $\Omega_{\mathrm{target}}$ is the solid angle under which the target is observed from the sensor.
- $\Omega_{\mathrm{p}}$ is the pixel field-of-view solid angle.

For small targets, the above solid angles can be approximated as:

$$\Omega_{\mathrm{target}} \approx \frac{A_{\mathrm{tg}}}{R^2},\ \Omega_{\mathrm{p}} \approx \frac{A_{\mathrm{p}}}{\mathrm{f}^2} \tag{60}$$

where:

- $\mathrm{A_{tg}}$ is the projected area of the target along the line of sight.
- $\mathrm{A_p}$ is the pixel area.
- R is the sensor–target range.
- $f$ is the focal length of the optical system.

If the optical system has a F-number (F/#) and an optical transmittance $\tau_{\mathrm{opt}}(\lambda)$, the total radiative flux incident on a pixel over a given wavelength band can be expressed as:

$$\Phi(\lambda) = L(\lambda)\tau_{opt}(\lambda)\frac{\pi}{4(F^{\#})^2}A_p \tag{61}$$

With an optical system of $f = 50\ mm$ and $\tau_{\text{opt}} = 0.9$, the incident radiative flux on the pixel is computed using Eq. (60) for different target ranges, based on the target radiance from Section 1 and the sensor parameters in Table 16. The results are presented in Figure 77.

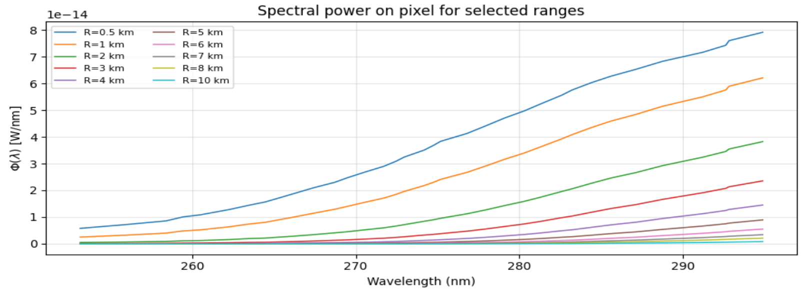


*Fig. 77. Spectral power on pixel*

Spectral radiative flux incident on the pixel accounting for the detector's quantum efficiency (Fig.78)

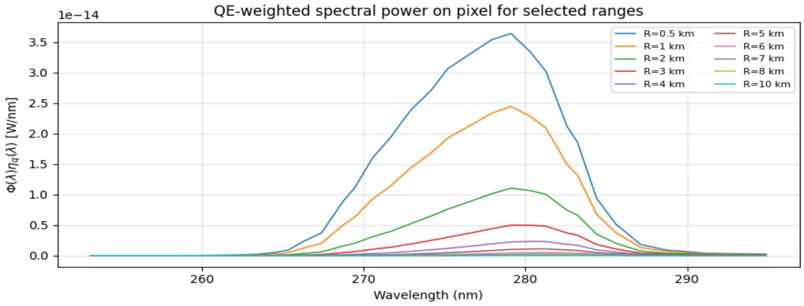


*Fig. 78. QE-weighted spectral power on pixel*

Total number of photons detected when a radiative flux $\Phi(\lambda)$is incident on the pixel surface, accounting for the detector's quantum efficiency

$$N_{sig} = \int_{\lambda_1}^{\lambda_2} \Phi(\lambda)\, \eta_q(\lambda) \frac{\lambda}{hc}\, t_{\text{int}} d\lambda \tag{62}$$

Where:

$\Phi(\lambda)$: spectral radiative flux incident on the pixel $[\text{W nm}^{-1}]$,

$\eta_q(\lambda)$: detector quantum efficiency (QE),

$h$: Planck's constant [J s],

$c$: speed of light $[\text{m s}^{-1}]$,

$t_{\text{int}}$: integration time [s].

Therefore, the general expression for the total number of signal photons incident on a pixel (accounting for the detector quantum efficiency) is:

$$N_{sig} = \int_{\lambda_1}^{\lambda_2} L(\lambda)\tau_{opt}(\lambda) \frac{\pi}{4(F/\#)^2} A_p \, \eta_q(\lambda) \frac{\lambda}{hc} \, t_{\text{int}} d\lambda \tag{63}$$

Let:

$$K(\lambda) = \tau_{opt}(\lambda) \frac{\pi}{4F^2} A_p \eta_q(\lambda) \frac{\lambda}{hc} \, t_{\text{int}}$$

Substituting into Eq. (62), we obtain:

$$N_{Sig} = \int_{\lambda_1}^{\lambda_2} K(\lambda) L(\lambda) \, d\lambda \tag{64}$$

Similarly, the total number of background photons incidents on the pixel (accounting for the detector quantum efficiency) can be expressed as:

$$N_{bg} = \int_{\lambda_1}^{\lambda_2} K(\lambda) L_{bg}(\lambda) \, d\lambda \tag{65}$$

The total detector noise is given by the root-mean-square (RMS) sum of the photon noise $\sqrt{N_{\text{sig}} + N_{\text{bg}}}$ and detector intrinsic noise $\sqrt{N_{\text{dark}}}$ and the read-out noise $\sigma_{read}$.

Finally, the signal-to-noise ratio (SNR) is calculated as:

$$\text{SNR} = \frac{N_{\text{sig}}}{\sqrt{N_{\text{sig}} + N_{\text{bg}} + N_{\text{dark}} + \sigma_{\text{read}}^2}} \tag{66}$$

This expression clearly represents the relationship between the target–background radiance contrast, observation geometry, atmospheric transmittance, and the electro-optical system parameters. It provides the fundamental basis for evaluating plume detectability under different atmospheric conditions and at long observation ranges.

Figure 79 shows the calculated SNR as a function of distance under different aerosol conditions. The background radiation is obtained from experimental measurements.

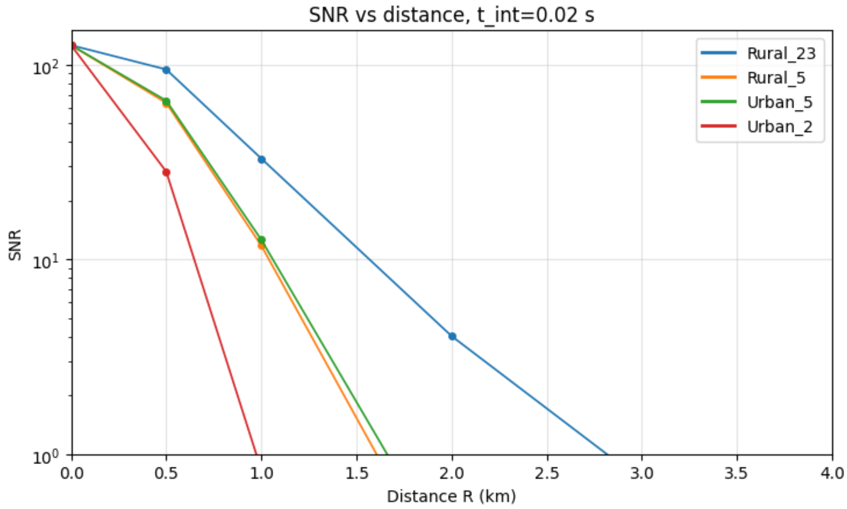


*Fig. 79. SNR for various aerosol conditions*

The calculated SNR results, considering experimentally measured background radiation, indicate that short-wavelength UV radiation is strongly scattered by aerosols and is characterized by the meteorological visibility parameter. Although two different aerosol models (urban and rural) are considered, the target detection capability is identical under the same visibility conditions.

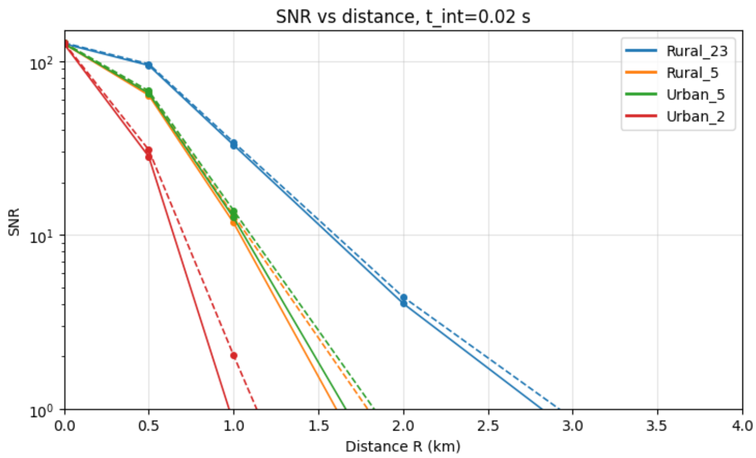


*Fig. 80. Comparison of SNR in the solar-blind region with background radiation (solid lines) and without background radiation (dashed lines)*

Figure 80 compares the SNR results for the case with experimentally measured UV background radiation (solid lines) and the commonly adopted assumption of no background radiation in the solar-blind region (dashed lines). It can be clearly observed that UV background radiation in the solar-blind region has a significant impact on target detection performance.

## 10. Conclusions

This dissertation focuses on the propagation of ultraviolet radiation in the atmosphere and its impact on target detection capability using UV sensing systems. The primary objective of the dissertation is to analyze both natural UV radiation (solar radiation) and UV radiation generated by targets (artificial sources), as well as the attenuation of these radiation components during atmospheric propagation. Based on this analysis, the UV background radiation is determined and its applications are analyzed. Two representative applications considered in this dissertation are airborne target detection in the near-UV spectral region (300-400nm) based on the negative contrast phenomenon between the target and the background, and rocket plume detection in the solar-blind region.

The research is conducted through a combination of theoretical analysis, numerical modelling using the MODTRAN computational code, and experimental measurements. Fundamental laws of radiation and the radiative transfer equation in the atmosphere are presented to establish the theoretical foundation of the dissertation.

- Author designed, calibrated, and deployed a UV radiation measurement station employing a photomultiplier tube operated in photon-counting mode in the 250–295 nm spectral range.
- Author performed a set of outdoor measurements to collect UV background radiation data under real atmospheric conditions.

Based on the measured results, an important conclusion can be drawn that the solar-blind region is not completely free of solar-induced UV background radiation; instead, a certain background level still exists. The magnitude of this background radiation depends on various factors, such as the solar zenith angle, cloud cover, aerosols, altitude, and atmospheric ozone concentration. These results demonstrate that UV background radiation is present in the solar-blind region and must be considered in target detection performance assessments.

The dissertation investigates the negative contrast phenomenon of aircraft in the near-ultraviolet spectral range (300–400 nm). By developing a computational model based on background radiation, path radiance, and atmospheric transmittance calculated using the MODTRAN software, the negative contrast results are compared with experimental measurements obtained using a Si PiN photodiode. The comparison shows good agreement between simulations and experimental data, thereby validating the proposed model. Detection range analysis based on the signal-to-noise ratio indicates that target detectability is strongly correlated with meteorological visibility and the degree of UV scattering caused by aerosols.

The dissertation also analyses the detection capability of UV radiation emitted by rocket engine plumes. The dominant radiation sources, including chemiluminescence and particle-related emission mechanisms, are identified and modelled. SNR-based detection analysis in the solar-blind region demonstrates that UV background radiation and atmospheric conditions have a significant influence on the performance of UV sensing systems.

From an application perspective, the obtained results provide practical value for the design, modelling, and performance evaluation of UV sensing systems for defense-related applications.

The author is aware of some limitations of the presented study but nevertheless it may constitute a useful base for further research. Future work may extend UV background radiation measurements to multiple geographical locations and diverse atmospheric conditions to establish a comprehensive database that enables more robust and reliable assessment of the existence and role of UV background radiation and its possible military applications.

## 11. References


[1]. D. Starikov, C. Boney, R. Pillai and A. Bensaoula, "Dual-band UV/IR optical sensors for fire and flame detection and target recognition," *ISA/IEEE Sensors for Industry Conference, 2004. Proceedings the*, New Orleans, LA, USA, 2004, pp. 36-40, doi: 10.1109/SFICON.2004.1287124.

[2]. X. Lin and Y. B. Zhang, “Application of Ultraviolet Imaging Technology to the Discharge of High-voltage Corona,” Journal of North China Institute of Water Conservancy and Hydroelectric Power, Vol. 32, No. 2, 2011, pp. 80-82. doi:10.3969/j.issn.1002-5634.2011.05.023

[3]. A. F. McKinlay and J. D. Diffey, “A reference action spectrum for ultraviolet induced erythema in human skin,” CIE J., vol. 6, pp. 17–22, 1987.

[4]. A. Auliciems, “Human bioclimatology: an introduction,” in Human Bioclimatology, pp. 1–6, 1998.

[5]. Yao, D. W., Hao, W., Yang, X. J., & Tian, Y. (2011, August). Research on UV detector technology and application in MAWS. In International Symposium on Photoelectronic Detection and Imaging 2011: Advances in Imaging Detectors and Applications (Vol. 8194, pp. 830-834). SPIE. https://doi.org/10.1117/12.901021.

[6]. Hirsh, I., Shkedy, L., Chen, D., Fishler, N., Hagbi, Y., Koifman, A., ... & Shtrichman, I. (2012, May). Hybrid dual-color MWIR detector for airborne missile warning systems. In Infrared Technology and Applications XXXVIII (Vol. 8353, pp. 189-200). SPIE. https://doi.org/10.1117/12.919462

[7]. L. Smith, M. Richardson, R. Ayling, and N. Barlow, “Effective expendable countermeasure model against dual-band infrared and ultraviolet man-portable air-defense seeker systems,” Optical Engineering, vol. 54, no. 8, p. 085104, Aug. 2015, doi: 10.1117/1.oe.54.8.085104.

[8]. T. Döhring, “Critical discussion on the UV absorption properties of Earth's atmosphere,” in Proc. SPIE 10453, Third International Conference on Applications of Optics and Photonics, vol. 10453, pp. 128–137, Aug. 2017. doi: 10.1117/12.2275808.

[9]. F. P. Neele and R. M. Schleijpen, “Electro-optical missile plume detection,” in Targets and Backgrounds IX: Characterization and Representation, Proc. SPIE, vol. 5075, 2003, pp. 270–280, doi: 10.1117/12.487510.

[10]. BAE Systems, “2-Color Advanced Warning System,” BAE Systems. [Online]. Available: https://www.baesystems.com/en-us/product/2-color-advanced-warning-system [Accessed: 18 Feb. 2026].

[11]. Northrop Grumman Corporation, “Northrop Grumman to Install AN/AAR-54(V) Warning Systems on Royal Netherlands Helicopters,”. Press Release, June 16, 2001. [Online]. Available: https://investor.northropgrumman.com/news-releases/news-release-details/northrop-grumman-install-anaar-54v-warning-systems-royal. [Accessed: 18 Feb. 2026].

[12]. Pastor, A. (2019). Infrared guidance systems. A review of two man-portable defense applications. OSF Preprints. doi:10.31219/osf.io/c6gxf.

[13]. J. Lyons, D. Long, and R. Chait, “Critical Technology Events in the Development of the Stinger and Javelin Missile Systems,” Center for Technology and National Security Policy, National Defense University, 2006.

[14]. M. Dura, “Telesystem Mesko: Będą nowe polskie rakiety. Lepsze od Piorunów,” Defence24, 7 Sept. 2023. [Online]. Available: https://defence24.pl/przemysl/telesystem-mesko-beda-nowe-polskie-rakiety-lepsze-od-piorunow [Accessed: 18 Feb. 2026].

[15]. Gurevich, M. S., Eskin, V. N., Chuprakov, A. M., & Shustov, N. Y. (2002). Trispectral target seeker for an optical homing head. Journal of Optical Technology, 69(9), 648. https://doi.org/10.1364/JOT.69.000648

[16]. Hietanen. M, Stuck. B.E, van Deventer.E, and Niu.S, Protecting workers from ultraviolet radiation, Vecchia.P., vol. 14. Oberschleißheim, Germany: nternational Commission on Non-Ionizing Radiation Protection, 2007.

[17]. R. E. Huffman, Atmospheric ultraviolet remote sensing, vol. 52. Academic Press, 1992

[18]. W. Tobiska and A. Nusinov, “ISO 21348-Space environment (natural and artificial) - Process for determining solar irradiances,” 2006.

[19]. W. L. Wolfe, “Radiation Theory,” in The Infrared and Electro Optical Systems Handbook, G. J. Zissis., vol. 1, Ann Arbor, MI; Bellingham, WA: Infrared Information Analysis Center; SPIE Press, 1993, ch. 1, pp. 8–9.

[20]. P. C. Simon, “Extraterrestrial Solar Irradiance in the Near and Medium UV Ranges,” in *Solar Ultraviolet Radiation*, Berlin, Heidelberg: Springer Berlin Heidelberg, 1997, pp. 1–12. doi: 10.1007/978-3-662-03375-3_1.

[21]. P. M. D. F. Forster, “Modeling Ultraviolet Radiation at the Earth’s Surface. Part I: The Sensitivity of Ultraviolet Irradiances to Atmospheric Changes,” *Journal of Applied Meteorology*, vol. 34, no. 11, pp. 2412–2425, Nov. 1995, doi: 10.1175/1520-0450(1995)034<2412:MURATE>2.0.CO;2.

[22]. “Standard Solar Constant and Zero Air Mass Solar Spectral Irradiance Tables,” 2000, ASTM International, West Conshohocken, PA. doi: 10.1520/E0490.

[23]. F. Kreith and J. F. Kreider, *Principles of Solar Engineering*. New York, NY: McGraw-Hill Book Company, 1978.

[24]. G. Hoffmann, *Principles and working mechanisms of water filtered infrared A (wIRA) in relation to wound healing*, vol. 2. *GMS Krankenhaushygiene Interdisziplinär*, 2007.

[25]. N. A. Anfimov, G. F. Karabadjak, B. A. Khmelinin, Y. A. Plastinin, and A. V. Rodionov, “Ultraviolet, Visible and Infrared Spectra Modeling for Solid and Liquid-fuel Rocket Exhausts,” AIAA Paper 2001-0660, 39th Aerospace Sciences Meeting & Exhibit, pp. 8–11, Jan. 2001.

[26]. D. Kilpin, *Ultraviolet Emission from Rocket Motor Plumes*, DSTO-TR-0002, Defence Science and Technology Organisation (DSTO), Australia, 1994.

[27]. E. Toscano, M. Martarelli, M. Pandarese, and A. Soria, “Optical Diagnostics for Solid Rocket Plumes Characterization: A Review,” *Energies*, vol. 15, no. 4, p. 1237, Feb. 2022. doi: 10.3390/en15041237.

[28]. M. Slack and A. Grillo, “High Temperature Rate Coefficient Measurements of CO + O Chemiluminescence,” *Combustion and Flame*, vol. 59, pp. 189–196, 1985.

[29]. D. E. Schmieder and G. W. Walker, “Camouflage, suppression, and screening systems,” in *The Infrared and Electro-Optical Systems Handbook*, Vol. 7: *Countermeasure Systems*, D. H. Pollock, Ed. Bellingham, WA, USA: SPIE Press, 1993, pp. 159–236.

[30]. Y. Yi, K. J. Yi, S. W. Baek, and B. Gu, “Infrared signature study of aircraft exhaust plume,” in *Proc. 15th Int. Symp. on Transport Phenomena and Dynamics of Rotating Machinery (ISROMAC-15)*, 2014.

[31]. S. P. Mahulikar, A. G. Marathe, A. G. Rao, and S. Sane, “Aircraft plume infrared signature in nonafterburning mode,” *J. Thermophys. Heat Transf.*, vol. 19, no. 3, pp. 413–415, 2005.

[32]. S. P. Mahulikar, H. R. Sonawane, and G. A. Rao, "Infrared signature studies of aerospace vehicles," *Prog. Aerosp. Sci.*, vol. 43, no. 7–8, pp. 218–245, 2007.

[33]. D.-m. Zhang and L. Bai, "Effects of alumina particle clusters on UV radiation signature in the aircraft plume," *J. Quant. Spectrosc. Radiat. Transf.*, vol. 252, p. 107082, 2020. https://doi.org/10.1016/j.jqsrt.2020.107082

[34]. A. Orzechowski, M. Nita, D. Powała, M. Pietraszak, T. Klemba, and A. Maranda, "Investigation of the ignition of MTV decoy flares," *Cent. Eur. J. Energ. Mater.*, vol. 18, no. 4, pp. 529–544, 2021, doi: 10.22211/cejem/145383.

[35]. E.-C. Koch and A. Dochnahl, "IR emission behaviour of magnesium/Teflon/Viton (MTV) compositions," *Propellants, Explosives, Pyrotechnics*, vol. 25, no. 1, pp. 37–40, 2000. https://doi.org/10.1002/(SICI)1521-4087(200001)25:1<37::AID-PREP37>3.0.CO;2-Z

[36]. E.-C. Koch, "Metal-Fluorocarbon-Pyrolants IV: Thermochemical and combustion behaviour of magnesium/Teflon/Viton (MTV)," *Propellants, Explosives, Pyrotechnics*, vol. 27, no. 6, pp. 340–351, 2002. https://doi.org/10.1002/prep.200290004

[37]. N. Brune, "Expendable Decoys," in *The Infrared and Electro-Optical Systems Handbook*, Vol. 7: *Countermeasure Systems*, J. S. Accetta and D. L. Shumaker, Eds. Bellingham, WA: SPIE Press, 1996, pp. 289–295.

[38]. E.-C. Koch, "Pyrotechnic countermeasures: II. Advanced aerial infrared countermeasures," *Propellants, Explosives, Pyrotechnics*, vol. 31, no. 1, pp. 3–19, 2006. https://doi.org/10.1002/prep.200600001

[39]. S. Elbasuney, A. A. Elmotaz, M. A. Sadek, M. Yehia, and H. Tantawy, "Superior spectral performance of decoy flares compositions via inclusion of graphite as a black body emitter," in *Proc. Int. Conf. Chem. Environ. Eng.*, vol. 10, no. 10, pp. 1–13, Military Technical College, July 2020. doi: 10.1088/1757-899X/975/1/012005.

[40]. D. W. Herbage and S. L. Salvesen, "Spectrally Balanced Infrared Flare Pyrotechnic Composition," U.S. Patent No. 5,472,533, 1995.

[41]. "Pyrophoric countermeasure flare," European Patent EP0800051B1, granted Nov. 27, 2002.

[42]. *U.S. Standard Atmosphere, 1976*, NOAA, NASA, and USAF, U.S. Government Printing Office, Washington, D.C., 1976.

[43]. United States Committee on Extension to the Standard Atmosphere, *U.S. Standard Atmosphere Supplements, 1966*, U.S. Government Printing Office, Washington, D.C., 1967.

[44]. T. W. Schlatter, "Atmospheric composition and vertical structure," *Environmental Impact and Manufacturing*, vol. 6, pp. 1–54, 2009.

[45]. J. M. Wallace and P. V. Hobbs, *Atmospheric Science: An Introductory Survey*, 2nd ed. Amsterdam: Elsevier, 2006.

[46]. "HITRAN: High resolution transmission molecular absorption database," HITRANonline, Harvard Smithsonian Center for Astrophysics, 2025. [Online]. Available: https://hitran.org/.

[47]. G. W. Petty, *A First Course in Atmospheric Radiation*, 2nd ed. Madison, WI: Sundog Publishing, 2006, pp. 343–347. ISBN: 978-0-9729033-1-8.

[48]. M. Sneep and W. Ubachs, "Direct measurement of the Rayleigh scattering cross section in various gases," *J. Quant. Spectrosc. Radiat. Transfer*, vol. 92, no. 3, pp. 293–310, 2005. doi: 10.1016/j.jqsrt.2004.07.025.

[49]. B. A. Bodhaine, N. B. Wood, E. G. Dutton, and J. R. Slusser, "On Rayleigh optical depth calculations," *J. Atmos. Oceanic Technol.*, vol. 16, no. 11, pp. 1854–1861, 1999. doi: 10.1175/1520-0426(1999)016<1854: ORODC>2.0.CO;2.

[50]. E. R. Peck and K. Reeder, "Dispersion of air," *J. Opt. Soc. Am.*, vol. 62, no. 8, pp. 958–962, 1972. doi: 10.1364/JOSA.62.000958

[51]. R. Penndorf, "Tables of the refractive index for standard air and the Rayleigh scattering coefficient for the spectral region between 0.2 and 20.0 μ and their application to atmospheric optics," *J. Opt. Soc. Am.*, vol. 47, no. 2, pp. 176–182, 1957. doi: 10.1364/JOSA.47.000176

[52]. D. R. Bates, "Rayleigh scattering by air," *Planet. Space Sci.*, vol. 32, no. 6, pp. 785–790, 1984. doi: 10.1016/0032-0633(84)90089-6

[53]. J. C. Owens, "Optical refractive index of air: Dependence on pressure, temperature and composition," *Appl. Opt.*, vol. 6, no. 1, pp. 51–59, Jan. 1967. doi: 10.1364/AO.6.000051

[54]. C. F. Bohren and D. R. Huffman, "Chapter 4: Absorption and scattering by a sphere," in *Absorption and Scattering of Light by Small Particles*, New York: John Wiley & Sons, 2008, pp. 83–129.

[55]. L. W. Abreu and G. P. Anderson, "The MODTRAN 2/3 report and LOWTRAN 7 model," Contract Report, vol. 19628(91-C), no. 0132, 1996.

[56]. Radiation Commission, *A Preliminary Cloudless Standard Atmosphere for Radiation Computation*, WCP-112, WMO/TD No. 24, World Meteorological Organization, 1986.

[57]. R. Jaenicke, "Tropospheric aerosols," Chapter 1 in *International Geophysics*, vol. 54, pp. 1–31, Academic Press, 1993.

[58]. D. A. G. Bruggeman, "The calculation of various physical constants of heterogeneous substances. I. The dielectric constants and conductivities of mixtures composed of isotropic substances," *Ann. Phys.*, vol. 416, pp. 636–791, 1935.

[59]. K. N. Liou, *An Introduction to Atmospheric Radiation*, vol. 84. San Diego, CA, USA: Academic Press, 2002.

[60]. A. Berk et al., *MODTRAN® 6.0.0 User's Manual*, Rev. 5, 2016.

[61]. J. B. Kerr, "Understanding the factors that affect surface UV radiation," in *Ultraviolet Ground- and Space-based Measurements, Models, and Effects III*, Proc. SPIE, vol. 5156, pp. 1–14, 2003. doi: 10.1117/12.509305.

[62]. C. R. Roy, H. P. Gies, D. J. Lugg, S. Toomey, and D. W. Tomlinson, "The measurement of solar ultraviolet radiation," *Mutation Research/Fundamental and Molecular Mechanisms of Mutagenesis*, vol. 422, no. 1, pp. 7–14, Nov. 1998, doi: 10.1016/S0027-5107(98)00180-8.

[63]. B. Weatherhead et al., "Ozone and ultraviolet radiation," in *Arctic Climate Impact Assessment: Scientific Report*, C. Symon, L. Arris, and B. Heal, Eds. Cambridge, UK: Cambridge University Press, 2005, ch. 5, p. 61.

[64]. J. B. Kerr and V. E. Fioletov, "Surface ultraviolet radiation," *Atmosphere-Ocean*, vol. 46, no. 1, pp. 159–184, 2008, doi: 10.3137/ao.460108

[65]. World Ozone and Ultraviolet Radiation Data Centre (WOUDC), "Spectral UV Irradiance Data, Station: Kaunas, Lithuania, 2025," Government of Canada. [Online]. Available: https://woudc.org. [Accessed: Jun. 23, 2025].

[66]. S. A. Kalogirou, "Chapter 2 – Environmental Characteristics," in *Solar Energy Engineering*, 2nd ed., Academic Press, 2014, pp. 51–123, doi: 10.1016/B978-0-12-397270-5.00002-9.

[67]. World Ozone and Ultraviolet Radiation Data Centre (WOUDC), "Spectral UV Irradiance Data, Station: Uccle, Belgium, 2024," Government of Canada. [Online]. Available: https://woudc.org. [Accessed: Jun. 23, 2025].

[68]. NOAA NESDIS, "Ozone Measuring Instrument on NOAA-21 Satellite Captures Its First Images," Feb. 22, 2023. [Online]. Available: https://www.nesdis.noaa.gov/news/ozone-measuring-instrument-noaa-21-satellite-captures-its-first-images. [Accessed: Jun. 23, 2025].

[69]. J. Calbó, D. Pagès, and J.-A. González, "Empirical studies of cloud effects on UV radiation: A review," *Reviews of Geophysics*, vol. 43, no. 2, 2005, doi: 10.1029/2004RG000155.

[70]. J. A. Bordewijk, H. Slaper, H. A. J. M. Reinen, and E. Schlamann, "Total solar radiation and the influence of clouds and aerosols on the biologically effective UV," *Geophysical Research Letters*, vol. 22, no. 16, pp. 2151–2154, Aug. 1995, doi: 10.1029/95GL01506.

[71]. J. Sabburg and J. Wong, "The effect of clouds on enhancing UVB irradiance at the earth's surface: A one year study," *Geophysical Research Letters*, vol. 27, no. 20, pp. 3337–3340, Oct. 2000, doi: 10.1029/2000GL011683.

[72]. C. Tiba and S. D. Silva Leal, "Enhancement of UV radiation by cloud effect in NE of Brazil," *International Journal of Photoenergy*, vol. 2017, Article ID 8107435, 2017. doi: 10.1155/2017/8107435.

[73]. NOAA, "Chapter 7: Surface Ultraviolet Radiation: Past, Present and Future," in *Scientific Assessment of Ozone Depletion: 2006*, WMO, Global Ozone Research and Monitoring Project—Report No. 50, Geneva, Switzerland, 2007. [Online]. Available: https://csl.noaa.gov/assessments/ozone/2006/chapters/chapter7.pdf

[74]. C. A. Gueymard, "SMARTS2, A Simple Model of the Atmospheric Radiative Transfer of Sunshine: Algorithms and Performance Assessment," Florida Solar Energy Center, FSEC-PF-270-95, 1995.

[75]. World Meteorological Organization (WMO), *Instruments to Measure Solar Ultraviolet Radiation – Part 1: Spectral Instruments*, GAW Report No. 125, WMO/TD-No. 1066, Geneva, Switzerland, 2001.

[76]. A. Redondas et al., "EUBREWNET: A global network of Brewer spectrophotometers for ozone, UV, and aerosol optical depth measurements," *Atmospheric*

*Chemistry and Physics*, vol. 18, no. 14, pp. 10347–10361, Jul. 2018. https://doi.org/10.5194/acp-18-10347-2018

[77]. Kipp & Zonen, "Brewer MkIII Spectrophotometer," Product Page, Delft, Netherlands. [Online]. Available: https://www.kippzonen.com/Product/50/Brewer-MkIII-Spectrophotometer.

[78]. WOUDC, "Davos, Switzerland (Station ID: DAV), 46.81°N, 9.84°E, 1590 m," Global UV and Ozone Data Archive, Environment and Climate Change Canada. [Online]. Available: https://woudc.org. [Accessed: Dec. 21, 2023].

[79]. NOAA Global Monitoring Laboratory, "Brewer Spectrophotometer Instrument (BSI) Program," NOAA, 2025. [Online]. Available: https://gml.noaa.gov/grad/antuv/Documents.jsp?grp=bsi.

[80]. N. Kouremeti and C. Sinclair, *Instruments to Measure Solar Ultraviolet Radiation. Part 4: Array Spectroradiometers*, GAW Report No. 191, WMO/TD-No. 1538, WMO, Geneva, Switzerland, 2010.

[81]. S. Diaz et al., *Instruments to Measure Solar Ultraviolet Radiation – Part 3: Multi-channel Filter Instruments*, GAW Report No. 163, WMO/TD-No. 1289, WMO, Geneva, Switzerland, 2010.

[82]. G. Seckmeyer et al., *Instruments to Measure Solar Ultraviolet Irradiance – Part 2: Broadband Instruments Measuring Erythemally Weighted Solar Irradiance*, WMO/TD-No. 1289, WMO, Geneva, Switzerland, 2005.

[83]. N. A. Krotkov et al., "Satellite estimation of spectral surface UV irradiance in the presence of tropospheric aerosols: 1. Cloud-free case," *J. Geophys. Res. Atmos.*, vol. 103, no. D8, pp. 8779–8793, Apr. 1998, doi: 10.1029/98JD00233.

[84]. N. A. Krotkov et al., "Satellite estimation of spectral surface UV irradiance: 2. Effects of homogeneous clouds and snow," *J. Geophys. Res. Atmos.*, vol. 106, no. D11, pp. 11743–11759, Apr. 2001, doi: 10.1029/2000JD900721.

[85]. J. P. Burrows et al., "The Global Ozone Monitoring Experiment (GOME): Mission concept and first scientific results," *J. Atmos. Sci.*, vol. 56, no. 2, pp. 151–175, Jan. 1999, doi: 10.1175/1520-0469(1999)056<0151:TGOMEG>2.0.CO;2.

[86]. A. Tanskanen et al., "Surface ultraviolet irradiance from OMI," *IEEE Trans. Geosci. Remote Sens.*, vol. 44, no. 5, pp. 1267–1271, May 2006, doi: 10.1109/TGRS.2005.861932.

[87]. WOUDC, "Data Search and Download," Environment and Climate Change Canada. [Online]. Available: https://woudc.org/en/data/data-search-and-download. [Accessed: 24-Jun-2025].

[88]. D. P. Häder et al., "ELDONET—a decade of monitoring solar radiation on five continents," *Photochemistry and Photobiology*, vol. 83, no. 6, pp. 1348–1357, 2007. https://doi.org/10.1111/j.1751-1097.2007.00189.x

[89]. X. Wang et al., "USDA UV-B monitoring system: An application of centralized architecture," *Computers and Electronics in Agriculture*, vol. 64, no. 2, pp. 326–332, 2008. https://doi.org/10.1016/j.compag.2008.05.018

[90]. A. W. Schmalwieser et al., "UV Index monitoring in Europe," *Photochemical and Photobiological Sciences*, vol. 16, pp. 1349–1370, 2017. https://doi.org/10.1039/c7pp00178a

[91]. Y. Jiang et al., "A 10 km daily-level ultraviolet-radiation-predicting dataset based on machine learning models in China from 2005 to 2020," *Earth System Science Data*, vol. 16, pp. 4655–4672, 2024. https://doi.org/10.5194/essd-16-4655-2024

[92]. A. Podstawczyńska, "UV and global solar radiation in Łódź, Central Poland," *International Journal of Climatology*, vol. 30, no. 1, pp. 1–10, Jan. 2010. https://doi.org/10.1002/joc.1864

[93]. A. M. Al Salihi and S. H. Abdulatif, "Analysis Global and Ultraviolet Radiation in Baghdad City, Iraq," *Journal of Natural Sciences Research*, vol. 6, no. 22, pp. 117–124, 2016.

[94]. B. Hu and Y. S. Wang, "Ultraviolet radiation in the background region over Northeast China," *Journal of Atmospheric Chemistry*, vol. 70, pp. 283–296, 2013. https://doi.org/10.1007/s10874-013-9269-2

[95]. J. L. Pinedo V. et al., "Spectral signature of ultraviolet solar irradiance in Zacatecas," *Geofísica Internacional*, vol. 45, no. 4, pp. 263–269, Oct.–Dec. 2006. https://doi.org/10.22201/igeof.00167169p.2006.45.4.163

[96]. WOUDC, "Station Metadata – ARG-342 Comodoro Rivadavia Aero, Argentina," Environment and Climate Change Canada. [Online]. Available: https://woudc.org/data/stations/?id=342. [Accessed: 24-Jun-2025].

[97]. WOUDC, "Station Metadata – ID 167: Wien (Vienna), Austria," Environment and Climate Change Canada. [Online]. Available: https://woudc.org/data/stations/167. [Accessed: 25-Jun-2025].

[98]. WOUDC, "Station Metadata – ID 516: Anmyeon do, Republic of Korea," Environment and Climate Change Canada. [Online]. Available: https://woudc.org/data/stations/516. [Accessed: 25-Jun-2025].

[99]. WOUDC, "Station Metadata – ID 312: Kaunas, Lithuania," Environment and Climate Change Canada. [Online]. Available: https://woudc.org/data/stations/312. [Accessed: 25-Jun-2025].

[100]. WOUDC, "Station Metadata – ID 412: Diekirch, Luxembourg," Environment and Climate Change Canada. [Online]. Available: https://woudc.org/data/stations/412. [Accessed: 25-Jun-2025].

[101]. WOUDC, "Station Metadata – ID 455: Chişinău, Moldova," Environment and Climate Change Canada. [Online]. Available: https://woudc.org/data/stations/455. [Accessed: 25-Jun-2025].

[102]. WOUDC, "Station Metadata – ID 531: Antananarivo, Madagascar," Environment and Climate Change Canada. [Online]. Available: https://woudc.org/data/stations/531. [Accessed: 25-Jun-2025].

[103]. WOUDC, "Station Metadata – ID 207: Mahe, Seychelles," Environment and Climate Change Canada. [Online]. Available: https://woudc.org/data/stations/207. [Accessed: 25-Jun-2025].

[104]. A. Baumgartner, "Grating monochromator wavelength calibration using an echelle grating wavelength meter," *Optics Express*, vol. 27, no. 10, pp. 13596–13610, May 2019, doi: 10.1364/OE.27.013596.

[105]. "All About Diffraction Gratings," Edmund Optics Knowledge Center, 2025. [Online]. Available: https://www.edmundoptics.com/knowledge-center/application-notes/optics/all-about-diffraction-gratings.

[106]. O. Schiek and E. Winter, "Two new mirror monochromators," *Appl. Opt.*, vol. 4, no. 2, pp. 195–199, Feb. 1965.

[107]. M. J. Dodge, "Refractive properties of magnesium fluoride," *Appl. Opt.*, vol. 23, no. 12, pp. 1980–1985, 1984.

[108]. D. Irish, "Monochromators," in *Practical Absorption Spectrometry*, A. Knowles and C. Burgess, Eds. Dordrecht: Springer, 1984, pp. 47–65. doi: 10.1007/978-94-009-5550-9_4.

[109]. Shimadzu Corporation, "Which is better: prism or diffraction grating?" Shimadzu Scientific Instruments FAQ. [Online]. Available: https://www.ssi.shimadzu.com/service-support/faq/uv-vis/instrument-design/15/index.html. [Accessed: Jun. 25, 2025].

[110]. ET Enterprises Ltd., "P9402B Series Photomultiplier Tube, 30 mm diameter, magnesium-fluoride window & CsTe photocathode, spectral response 110–360 nm," Uxbridge, UK: ET Enterprises Ltd., 2025. [Online]. Available: https://et-enterprises.com/products/photomultipliers/product/p9402b series. [Accessed: Jun. 25, 2022].

[111]. Hamamatsu Photonics K.K., *Photomultiplier Tubes: Basics and Applications*, 4th ed., rev. E. Hamamatsu City, Japan: Hamamatsu Photonics K.K., 2017. [Online]. Available: https://www.hamamatsu.com/.

[112]. U. Franke, "Drones in Ukraine: Four lessons for the West," 2025. [Online]. Available: https://ecfr.eu/article/drones-in-ukraine-four-lessons-for-the-west/. [Accessed: Jul. 21, 2025].

[113]. L. Smith, M. Richardson, R. Ayling, and N. Barlow, "Effective expendable countermeasure model against dual-band infrared and ultraviolet man-portable air-defense seeker systems," *Optical Engineering*, vol. 54, no. 8, p. 085104, Aug. 2015, doi: 10.1117/1.oe.54.8.085104.

[114]. K.-S. Doo, J.-S. Oh, S.-G. Jahng, H.-K. Hong, J.-S. Choi, and D.-S. Seo, "Simulation of target detection in ultraviolet and infrared bands," *Optical Engineering*, vol. 40, no. 11, pp. 2646–2654, Nov. 2001, doi: 10.1117/1.1411975.

[115]. C. Willers, J. Delport, and M. Willers, "CSIR optronic scene simulator finds real application in self-protection mechanisms of the South African Air Force," in *Technologies for Optical Countermeasures VII*, Bellingham, WA: SPIE, 2010. doi: 10.1117/12.850788.

[116]. D. G. Pelli and P. Bex, "Measuring contrast sensitivity," *Vision Research*, vol. 90, pp. 10–14, 2013. https://doi.org/10.1016/j.visres.2013.04.015

[117]. A. Rogalski, Z. Bielecki, J. Mikołajczyk, and J. Wojtas, "Ultraviolet Photodetectors: From Photocathodes to Low-Dimensional Solids," *Sensors*, vol. 23, p. 4452, 2023. https://www.mdpi.com/1424-8220/23/9/4452

[118]. J. Lloyd, "Fundamentals of Electro-Optical Imaging Systems Analysis," in *Electro-Optical Systems Design, Analysis, and Testing*, M. C. Dudzik, Ed., *The Infrared & Electro-Optical Systems Handbook*, Vol. 4, SPIE Press, 1993, ch. 1, pp. 18–20. https://doi.org/10.1117/3.2543823.ch1

[119]. Y. Chen, J. Li, and R. Qiang, "Study of spectral radiation characteristics of solid rocket plume based on an improved SHDOM," SPIE, Nov. 2023, p. 9. https://doi.org/10.1117/12.2687391

[120]. J. M. Burt, *Monte Carlo Simulation of Solid Rocket Exhaust Plumes at High Altitudes*, University of Michigan, Ann Arbor, MI, USA, 2006.

[121]. I. Gaissinski, Y. Levy, M. Lev, and V. Sherbaum, "Effect of soot particles on supersonic rocket plume properties," *International Journal of Turbo and Jet Engines*, vol. 29, no. 2, pp. 89–110, Jun. 2012. https://doi.org/10.1515/tjj-2012-0014

[122]. Y. Lou and T. Bai, "A study on UV missile plume emission model," in *ICO20: Remote Sensing and Infrared Devices and Systems*, SPIE, Jan. 2006, p. 60310F. https://doi.org/10.1117/12.667927

[123]. A. Blanc, L. Deimling, and N. Eisenreich, "UV- and IR-signatures of rocket plumes," *Propellants, Explosives, Pyrotechnics*, vol. 27, no. 3, pp. 185–189, Jun. 2002. https://doi.org/10.1002/1521-4087(200206)27:3<185::AID-PREP185>3.0.CO;2-H

[124]. N. A. Anfimov, G. F. Karabadjak, B. A. Khmelinin, Y. A. Plastinin, and A. V. Rodionov, "Analysis of mechanisms and nature of radiation from aluminum oxide in different phase states in solid rocket exhaust plumes," in *AIAA 28th Thermophysics Conference*, AIAA, 1993. https://doi.org/10.2514/6.1993-2818

[125]. Y. Xu, L. Bai, L. Zhang, J. Li, H. Shi, and L. Guo, "Analysis of UV radiation of solid rocket plume containing multiphase alumina clusters," *Int. J. Heat Mass Transf.*, vol. 247, Sep. 2025. https://doi.org/10.1016/j.ijheatmasstransfer.2025.127125

[126]. R. Rehm et al., "Toward AlGaN Focal Plane Arrays for Solar-Blind Ultraviolet Detection," *Physica Status Solidi (A)*, vol. 217, no. 7, Apr. 2020. https://doi.org/10.1002/pssa.201900769

[127]. W. B. Zhao et al., "Solar-blind photodetectors and focal plane arrays based on AlxGa1-xN," *Bandaoti Guangdian/Semiconductor Optoelectronics*, vol. 30, no. 1, pp. 21–24, Feb. 2009.

[128]. L. Wang et al., "Recent Progress in Solar-Blind Photodetectors Based on Ultrawide Bandgap Semiconductors," *ACS Omega*, Jun. 18, 2024. doi: 10.1021/acsomega.4c02897.

[129]. Q. Cai et al., "Progress on AlGaN-based solar-blind ultraviolet photodetectors and focal plane arrays," *Light: Science & Applications*, Dec. 01, 2021. doi: 10.1038/s41377-021-00527-4.

[130]. E. Cicek, R. McClintock, C. Y. Cho, B. Rahnema, and M. Razeghi, "AlxGa1-xN-based back-illuminated solar-blind photodetectors with external quantum efficiency of 89%," *Appl. Phys. Lett.*, vol. 103, no. 19, Nov. 2013. https://doi.org/10.1063/1.4829065

**List of drawings:**

**List of tables:**